STIGMATIC SPECTROSCOPY OF THE SOLAR ATMOSPHERE IN THE VACUUM-ULTRAVIOLET

by

Hans Thomas Courrier

A dissertation submitted in partial fulfillment
of the requirements for the degree

of

Doctor of Philosophy

in

Physics

MONTANA STATE UNIVERSITY
Bozeman, Montana

May 2020

DEDICATION

To my parents, Thomas J. and Marilyn S. Courrier, for their unfailing support and presence.

To Lindsay Ryder, for your unconditional love and support.

ACKNOWLEDGEMENTS

This work would not have been possible without the generous support and guidance of Dr. Charles Kankelborg. Thank you for your valuable insight and wisdom that you were always willing to impart and your encouragement that kept me going. Thanks also go to my graduate committee for their efforts, advice, and guidance: Dr. John Carlsten, Dr. Rufus Cone, Dr. Dana Longcope, Dr. David McKenzie, and Dr. Jiong Qiu. Sounding rocket and satellite missions are a collective effort and would not be possible without the work of many hands. I would like to extend my gratitude to my MSU team members: Dr. J. L. Fox, Dr. T. Rust, R. Smart, J. Parker, K. Mashburn, J. Plovanic, M. Norton, J. Maxwell, S. Atwood, J. Knoll, and J. Hartman, for their contributions. Neither launch of the MOSES instrument would have been possible without the professional and excellent work of the NSROC team and WSMR staff. It was also a great privilege to work with the members of the LMSAL IRIS team, including Dr. B. De Pontieu and Dr. J. P. Wülser. I am fortunate to have found many good friends in the MSU Physics Department staff. Thanks to N. Williams for your above and beyond technical assistance and the many entertaining conversations around a milling machine. I am certain I would have lost my way long ago if not for the guidance and wisdom of M. Jarret. Thank you, Margaret.

Thanks to my parents, T. and M. Courrier, for providing a loving home and good education. L. Ryder has been a supportive partner and friend through all consuming work; may I always be there for her.

TABLE OF CONTENTS

TABLE OF CONTENTS – CONTINUED

TABLE OF CONTENTS – CONTINUED

LIST OF TABLES

Table Page

LIST OF FIGURES

Figure Page

LIST OF FIGURES – CONTINUED

LIST OF FIGURES – CONTINUED

ABSTRACT

The solar atmosphere presents a complicated observing target since tremendous variability exists in solar features over a wide range of spatial, spectral, and temporal scales. Stigmatic spectrographs are indispensable tools that provide simultaneous access to spatial context and spectroscopy, enabling the diagnosis of solar events that cannot be accomplished by imaging or spectroscopy alone. In this dissertation I develop and apply a novel technique for on orbit spectrograph calibration, recover co-temporal Doppler shifts of widely spaced solar features, and describe a new design for a slitless solar spectrograph.

The *Interface Region Imaging Spectrograph, (IRIS)* is currently the highest spatial and spectral resolution, space based, solar spectrograph. Ongoing calibration is important to maintaining the quality of *IRIS* data. Using a Mercury transit against the backdrop of the dynamic solar atmosphere, I characterize the spatial point spread functions of the spectrograph with a unique, iterative, blind, deconvolution algorithm. An associated deconvolution routine improves the ability of *IRIS* to resolve spatially compact solar features. This technique is made freely available to the community for use with past and future *IRIS* observations.

The Multi-Order Extreme Ultraviolet Spectrograph (MOSES) is a slitless spectrograph that collects co-temporal, but overlapping spatial and spectral images of solar spectral lines. Untangling these images presents an ill-posed inversion problem. I develop a fast, automated method that returns Doppler shifts of compact solar objects over the entire MOSES field of view with a minimum of effort and interpretation bias.

The Extreme ultraviolet Snapshot Imaging Spectrograph (ESIS) is a slitless spectrograph that extends the MOSES concept. I describe this new instrument, which is far more complex and distinct as compared to MOSES, and the contributions I made in the form of optical design and optimization. ESIS will improve the quality of spatial and spectral information obtained from compact and extended solar features, and represents the next step in solar slitless spectroscopy.

Taken together, these contributions advance the field by supporting existing instrumentation and by developing new instrumentation and techniques for future observations of the solar atmosphere.

CHAPTER ONE

INTRODUCTION

1.1 Spectroscopy and the Solar Atmosphere

The Sun, as observed from Earth, can be decomposed into several layers. The photosphere is the layer that is observed in the visible continuum. In broad terms, temperature and density increase from the top of the photosphere inward, which correlates to a rapid increase in optical density. For this reason, the photosphere represents the “surface” of the Sun as visible to our eyes. The radiation spectrum from the photosphere is roughly approximated by that of a blackbody at $\sim$5800 K, superimposed by Fraunhofer absorption lines from the photosphere and chromosphere in the foreground.

The solar interior comprises the layers below the photosphere. Moving inward the next layer encountered is the convective zone, followed by the radiative zone. Both of these layers are named for their dominant processes of energy transport. The innermost layer is the core, where nuclear fusion powers the entire star. Starting from the $\sim$4000 K temperature minimum at a position about 500 km above the photosphere, both temperature and density increase by orders of magnitude as radius decreases [*e.g.* Model S, Christensen-Dalsgaard et al., 1996].

The solar atmosphere consists of the top of the photosphere and the layers above. The chromosphere sits directly above the photosphere, while the corona is the outermost layer that can extend well beyond the Earth. In between the chromosphere and corona is the transition region (TR). The simplest models describe the TR as a thin interface layer, even though observations present a more complicated picture. In the solar atmosphere, density continues to decrease as height above the photosphere increases. This correlates with a decrease in optical depth. From the upper chromosphere outward, the solar atmosphere is well approximated as an optically transparent[1] medium, so that there is little absorption or scattering of outgoing radiation. Somewhat curiously, however, the temperature in the solar atmosphere increases with height above the photosphere; a relatively gradual rise from the the temperature minimum above photosphere is observed in the chromosphere, before rapidly increasing through the TR to ∼1 MK at the base of the corona [*e.g.* Mariska, 1986]. This anomalous temperature profile clearly indicates a source of heating is driving the temperatures in solar atmosphere away from thermodynamic equilibrium.

This high temperature corona was first hinted at during an August 7, 1869 solar eclipse. A green emission line at 530 nm originating from the solar corona was observed independently by Charles Augustinus Young and William Harkness during the lunar occultation. The emission line did not correspond to any known element at the time, so a new element "Coronium" was hypothesized. Ultimately, Coronium would never materialize; almost 60 years would pass before Walter Grotrian (1939) and Bengt Edlén (1942) connected the green emission with the more terrestrial but highly ionized Fe XIV. Lines of highly ionized nickel and calcium were also identified, making it apparent that the corona must be very hot, as these high ionization states could only exist at temperatures greater than 10^6K.

Under further scrutiny, the construct of layers tends to fall apart above the photosphere. This is because tremendous variability in both temperature and

---

[1] The term "optically thin" is sometimes imprecisely (or ambiguously) used to described the concept of transparent plasmas in the corona and transition region in the relevant literature.

density exists at any given radius in the solar atmosphere. As an example, Figure 1.1 shows a collection of loops above the solar limb in three filter-bands of the Atmospheric Imaging Assembly [AIA, Lemen et al., 2012] on board the *Solar Dynamics Observatory*. In the AIA images, each filter band roughly corresponds to an ionization temperature. At 211 Å, much of the emission is from Fe XIV at ∼2 MK. In the 171 Å channel, emission is dominated by Fe IX at ∼0.7 MK, while in the 304 Å channel He II is the primary emitter at ∼0.5 MK [O'Dwyer et al., 2010]. Figure 1.1 shows that emission from the loops spans three different temperature regimes, and that these three regimes co-exist in close proximity to each other. The loops also highlight extreme variability in density, as these structures are surrounded by space that is comparatively much less dense. Furthermore, because the plasma in this region is attached, or "frozen-in," [*e.g.* Priest, 1982] to the magnetic field, the observational inference is that the emitting plasma in each of the three panels in Figure 1.1 traces out loops in magnetic field lines. From this situation, combined with the extreme disparities in temperatures and pressures in close proximity, a picture emerges of each loop containing its own individual atmosphere. This distinct anisotropy and inhomogeneity stands in stark contrast to the notion of a solar atmosphere that is only a function of radius.

Emission from the transition region and corona is primarily from far ultraviolet (FUV) and extreme ultraviolet (EUV) emission lines from highly ionized atoms, formed between temperatures of 10^4 and 10^6 K [Vernazza and Reeves, 1978, Del Zanna and Mason, 2018]. Shortward of ∼100 nm, blackbody emission quickly dies out so that there is little continuum and the EUV solar spectrum is largely dominated by individual emission lines. Assuming ionization equilibrium, these emission lines are formed over relatively narrow temperature ranges and, in most cases, can be well isolated with a spectral resolution of ∼0.3 nm [*e.g.* Vernazza and Reeves, 1978, noting

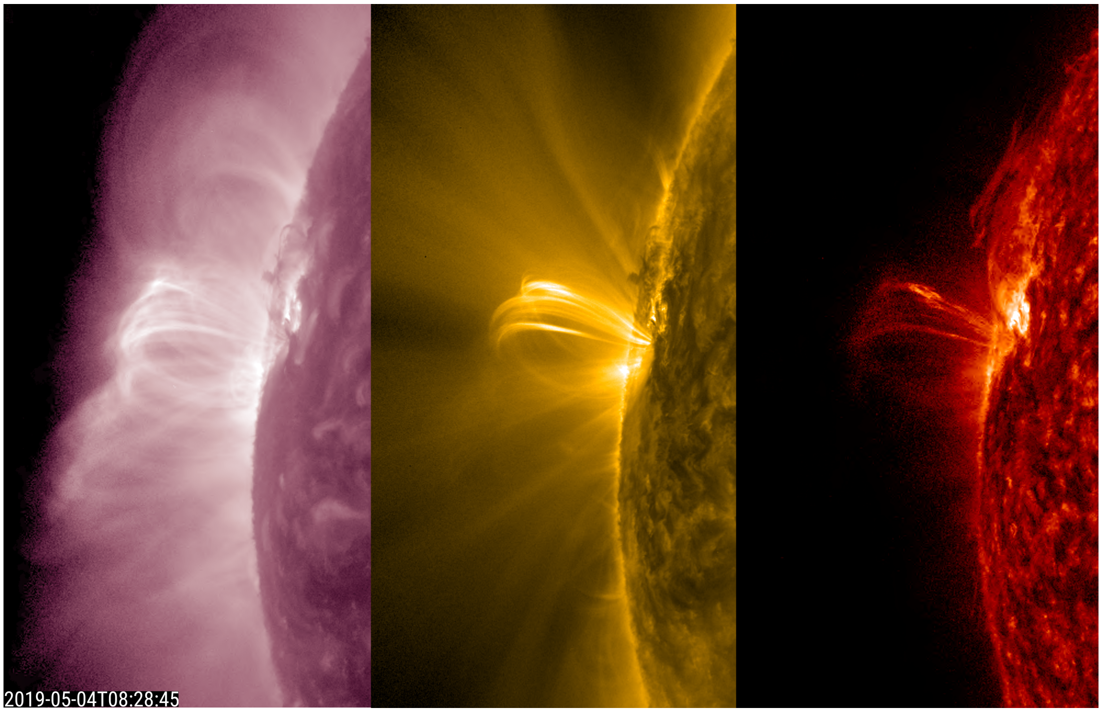

Figure 1.1: Loops over NOAA Active Region 12740. Emission from the loops is seen in close proximity across three different AIA ionization temperature regimes, AIA 211 Å (∼2 MK, left panel) AIA 171 Å (∼0.7 MK, center panel), and AIA 304 Å (∼0.5 MK, right panel), showing that temperature is not strictly a function of height.

that there are of course closely spaced and blended lines].

Since optical depth effects and continuum are largely absent in many FUV and EUV lines, spectroscopic interpretation of individual line profiles is relatively straightforward. The ion velocity distribution (*i.e.* the profile of a particular line) is due primarily to Doppler shifts caused by bulk flows of the plasma and microscopic thermal motions of the ions in the transparent solar atmosphere. Further information can be obtained by comparing emission line pairs. Emission by ions of the same element formed in overlapping or close temperature regimes gives information about temperature, while comparing lines of allowed and forbidden transitions of the same ion yields density information [*e.g.* Feldman et al., 1978, Del Zanna and Mason, 2018]. For these reasons, spectroscopy is an ideal tool for diagnosing physical conditions in the solar atmosphere. Imagers such as the *Transition Region and Coronal Explorer* [*TRACE*, Handy et al., 1999] and AIA provide a complementary technology as Figure 1.1 demonstrates. Multilayer vacuum ultraviolet (VUV) coatings make it possible to image the sun in a relatively narrow band ($\lambda/\Delta\lambda \sim 10-50$, using normal incidence mirrors [*e.g.* Underwood, 1981, Windt et al., 2004]). However, from a spectroscopic point of view, these "narrow band" images contain contributions from multiple emission lines [O'Dwyer et al., 2010]. Nevertheless, multilayer passbands that are dominated by a single-peaked contribution function (*i.e.* lines formed at similar temperatures) can be interpreted, with some care, as a single temperature regime. Thus, this type of imagery not only provides sky-plane motions, but places the scene in a particular temperature context. For example, from the three AIA images in Figure 1.1 it is easy to discern the co-existence and spatial proximity of the loops across three different temperature regimes in the solar atmosphere.

1.2 Stigmatic Solar Spectroscopy

In a *stigmatic* slit spectrograph, at a particular wavelength, each point along the slit is mapped to a point at the focal plane. If the slit is placed at the focus of a solar telescope, imaging and spectroscopy are combined so that spectra can be correlated to specific physical structures on the Sun. The observation of Zeeman splitting in sunspots by Hale [1908] is a classic example. In the right panel of Figure 1.2, the splitting of the Fe 617.3 nm absorption line is clearly seen in Hale's 1919 spectrum [Hale et al., 1919]. Comparing the Zeeman splitting of this stigmatic spectrum with the co-pointed broadband white light imagery in the left panel of Figure 1.2 clearly shows a strong magnetic field is correlated with the sunspot. Hale's observations led to the realization that sunspots mark locations where concentrations of magnetic flux emerge from the photosphere into the solar atmosphere.

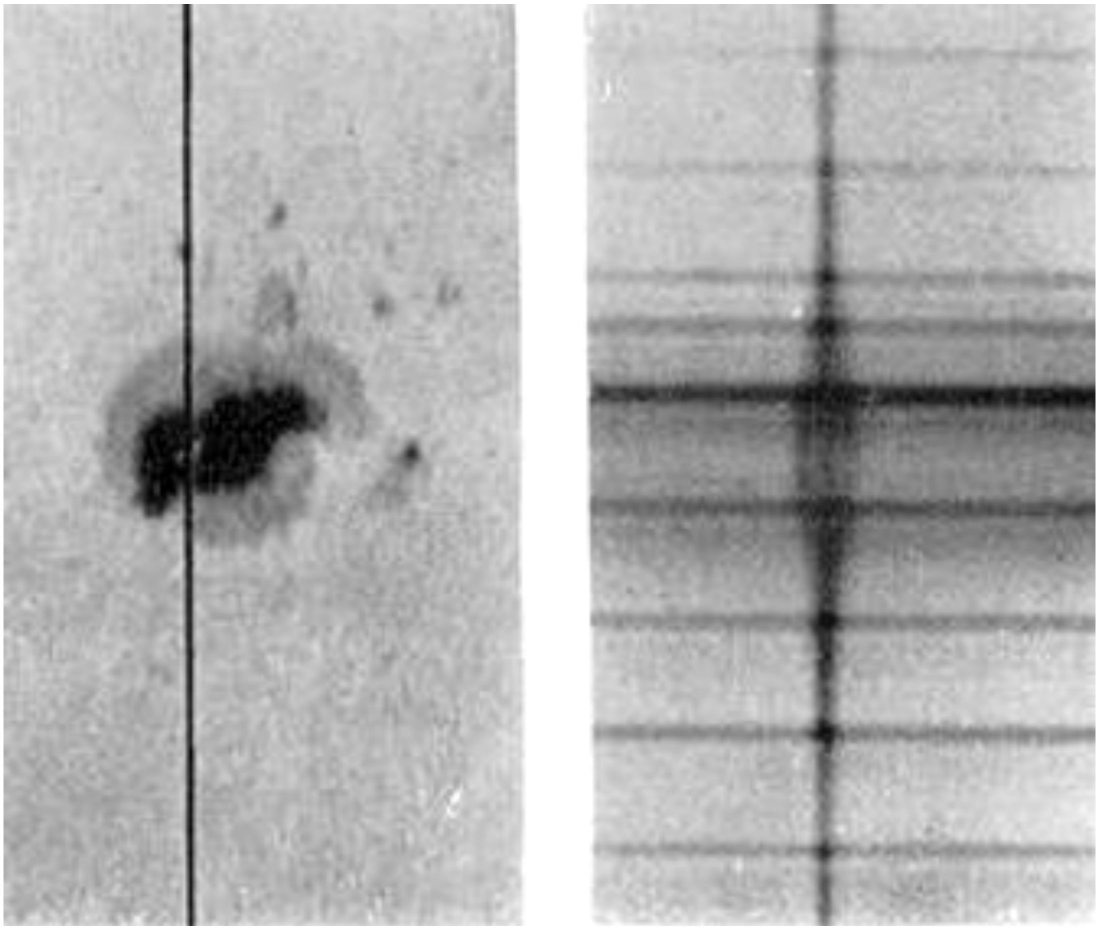

Figure 1.2: Sunspot (left) associated with concentrations of strong magnetic flux emergence by Zeeman splitting of the Fe 617.3 nm line (right) from Hale et al. [1919]. The position of the spectrograph slit is marked by the dark vertical line in the left image.

Observations in VUV wavelengths are key to understanding the structure and dynamics of the solar atmosphere. This is because in these wavelengths the solar atmosphere is bright while the photosphere is dark. In visible wavelengths, strong emission from the photosphere dominates and "washes out" the much weaker contribution from the more rarefied solar atmosphere. Hale's Mount Wilson observations were limited to visible wavelengths as the Earth's atmosphere is effectively opaque to VUV radiation. Since the late 1940s, research rockets have carried spectrographs, imagers, and other instrumentation above the Earth's atmosphere, enabling access to solar VUV radiation [*e.g.* Baum et al., 1946, Tousey, 1986]. In more recent years, satellites [*e.g.* Wilhelm et al., 2004, Del Zanna and Mason, 2018, and the references therein] have enabled much longer and consistent solar VUV observation than suborbital rockets. Rockets, however, continue to provide a low-cost and low-risk platform to access space for novel and unconventional instrumentation [*e.g.* Tousey, 1986, Fox, 2011, Kobayashi et al., 2012, 2014, Brosius et al., 2014, Kubo et al., 2016, Ishikawa et al., 2017].

Despite the decades of observation outlined above, our understanding of how energy is transported from the relatively cool photosphere through the chromosphere and TR to the ∼1 MK corona remains incomplete. It is generally agreed that the source of energy is magnetic in nature; *e.g.* Pevtsov et al. [2003] showed a direct correlation between photospheric magnetic flux and power radiated from the corona in the form of X-rays. However, the exact heating mechanism(s) are yet to be identified [*e.g.* Klimchuk, 2006, Schmelz and Winebarger, 2015, and the references therein]. In the remainder of this section I describe two possible phenomena of energy transport within the TR that have distinct spectroscopic signatures. Magnetic reconnection may serve as a source of energy in the solar atmosphere by directly converting magnetic energy to plasma kinetic energy. Magnetohydro dynamic (MHD) waves provide a potential mechanism to move energy through the layers of the solar atmosphere, depositing some energy in the TR and corona through dissipation, or damping, of the wave amplitude. Through these two (or potentially, some other) mechanisms, the strong magnetic fields first observed by Hale punctuating the photosphere and emerging into the solar atmosphere may prove to be the source of energy to the hot solar corona.

1.2.1 Magnetic Reconnection

Magnetic reconnection describes the process wherein pairs of differently directed magnetic field lines in a plasma "break" and reconnect with each other, forming a lower energy state [*e.g.* Parker, 1957, Petschek, 1964]. Reconnection allows the magnetic field lines to relax by shortening, releasing kinetic energy in the process. The electric field associated with this change in magnetic field can also cause particle acceleration. Both kinetic energy (flows) and energetic particles can give rise to heating so that, through the reconnection process, magnetic energy is converted into thermal energy. The actual reconnection site is believed to be too small to be resolved in the solar atmosphere. However, from the magnetic, kinetic, and thermal signatures, reconnection can be implicated in many solar events, such as flares [Priest and Forbes, 2002], macrospicules [Wang, 1998], and explosive events [EEs, Dere et al., 1991]. Outside of the solar atmosphere, reconnection is observed during magnetic "substorms" that release large amounts of solar wind energy stored in the Earth's magnetic field [Angelopoulos et al., 2008]. Although reconnection appears to be ubiquitous in the solar atmosphere, the process (or processes) by which reconnection proceeds is not well understood.

Explosive events (EEs) are an example of a reconnection-type process in the TR. They are observed as exceptionally strong ($\sim$100 $\mathrm{km\,s^{-1}}$) Doppler shifted (or broadened) features in spectral line profiles [Brueckner and Bartoe, 1983, Dere et al., 1984, 1991]. Figure 1.3 shows an example of such an EE observed by the Naval Research Laboratory (NRL) High Resolution Telescope and Spectrograph [HRTS Dere et al., 1991]; the strong Doppler shifts are apparent in the O IV and Si IV lines near the center of the image. EEs are compact, numerous, and highly energetic, with lifetimes on the order of $60-90$ s [Brueckner and Bartoe, 1983, Dere et al., 1991, Fox et al., 2010]. They are also relatively easily observed in multiple TR lines by numerous

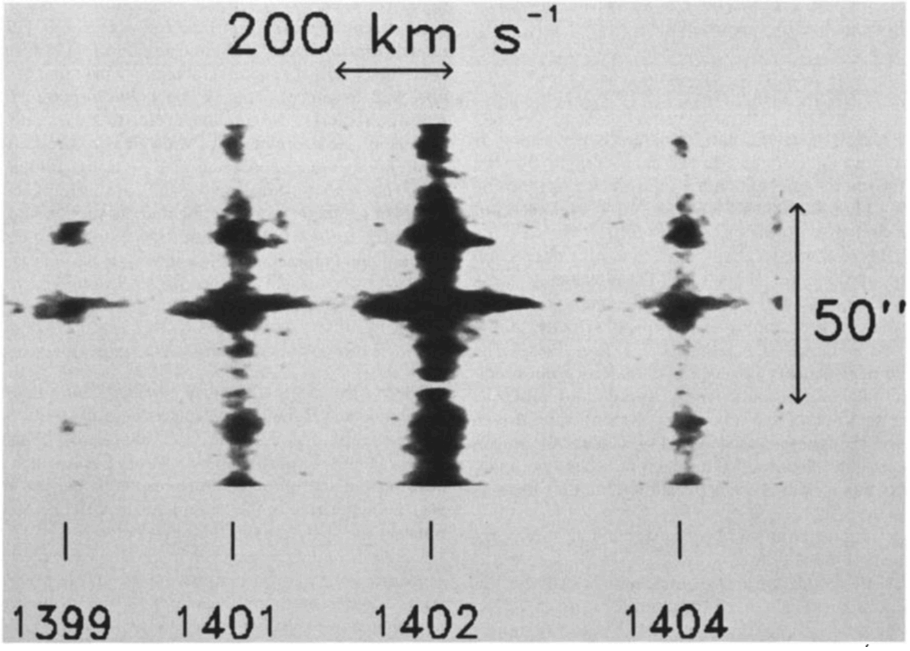

Figure 1.3: Stigmatic spectra from the NRL Naval High Resolution Telescope and Spectrograph (HRTS) showing an EE in lines of O IV (1399, 1401, and 1404 nm) and Si IV (1402 nm) from Dere et al. [1991].

VUV spectrographs (*e.g.* C IV, Si IV, and He II [Dere et al., 1989, Innes et al., 1997, Rust, 2017, Innes et al., 2015]) and are so frequent that one can expect to observe at least one EE with a slit spectrograph every ∼ 5 minutes [Dere, 1994, Innes et al., 1997].

The fast, sometimes bi-directional, [*e.g.* Innes et al., 1997, Fox, 2011, Rust, 2017, and the references therein], outflows from the core of an EE are a key signature of impulsive energy release that implicates magnetic reconnection. This is because in the TR and corona the plasma is essentially frozen into the magnetic field, able to travel along but not across magnetic field lines [*e.g.* Priest, 1982, Rust, 2017]. Post-reconnection, because the plasma is frozen-in, it is dragged along with the field lines, and thus the motion is perpendicular to the magnetic field (*e.g.* the plasma motion diagrammed schematically in Figure 1.4). This reconfiguration reduces the energy in the field. Thus, magnetic energy is converted to plasma kinetic energy. The Alfvén speed, v_a, is the characteristic velocity associated with this conversion of energy,

$$v_a = \frac{B}{\sqrt{4\pi\rho}}\,, \tag{1.1}$$

where the plasma mass density can be approximated as $\rho = n_e m_p$, the product of electron density n_e and the proton mass m_p. Estimates of the Alfvén speed in the TR are on the order of $100\,\mathrm{km\,s^{-1}}$ [*e.g.* Dere et al., 1991]. This is similar in magnitude to the Doppler shifts produced by EEs, but much greater than the 25-30 $\mathrm{km\,s^{-1}}$ non-thermal velocities observed from Si IV, O V and N V ions in TR quiet sun [*e.g.* Akiyama et al., 2005].

The Petschek model of fast reconnection is an example of how reconnection might proceed in a particular EE. Assuming and inflow velocity $\frac{1}{10}$ to $\frac{1}{100}$ of the Alfvén speed ($\sim 100\,\mathrm{km\,s^{-1}}$ in conditions associated with typical EE's) and characteristic length 1000 km, the time for Petschek reconnection to convert magnetic energy to kinetic energy is between $100-1000\,\mathrm{s}$, comparable to the observed $60-90\,\mathrm{s}$ EE lifetime [Dere et al., 1991]. MHD simulations by Innes and Tóth [1999] show high-velocity outflows from the EE core resulting from Petschek reconnection. These simulations do not show any associated emission from the core of the spectral line profile. A simplified diagram and distinctly red and blue shifted spectral signature for the Petschek reconnection scenario is presented in Figure 1.4 panels (a) and (b), respectively.

In another study, Innes et al. [2015] observed bi-directional outflows from an EE in the Si IV line with the *Interface Region Imaging Spectrograph, (IRIS)* [De Pontieu

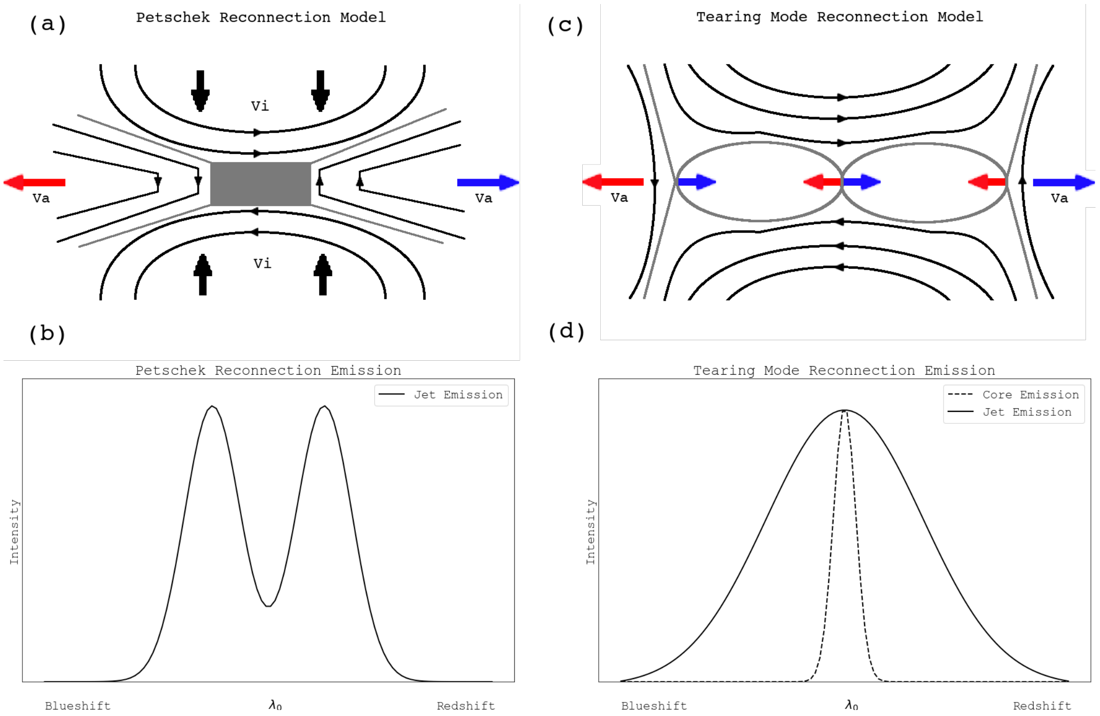

Figure 1.4: Diagrams of spectral signatures resulting from Petschek (panels a and b) and Tearing mode (panels c and d) EE reconnection models from Innes and Tóth [1999] and Innes et al. [2015] respectively. In (a) plasma is accelerated to the Alfvén speed along the line of sight by retracting post-reconnection field lines; the moving plasma appears as distinct red and blue shifts in the spectrum in (b). In (c) the tearing mode of reconnection accelerates plasma at a series of locations to a significant fraction of the Alfvén speed. However, the accelerated plasma is trapped in magnetic islands so that its motion is slowed after a short time. Emission from this hot, dense, and slow moving plasma creates the distinct core component in the spectrum shown in (d).

et al., 2014]. However, in this case significant emission was also detected from the core of the line profile. Similar EEs of this type showing brightening of the line core have been reported elsewhere [*e.g.* Dere et al., 1991, Innes et al., 1997]. The hypothesis of Innes et al. [2015] is that the core brightening observed after a short time in this event is due to tearing-mode reconnection. First, the tearing mode of reconnection accelerates plasma to high velocities at a series of locations along the extended separatrix region. The accelerated plasma is trapped within a shrinking magnetic island, so that its motion is soon damped (Figure 1.4 (c)). Emission from this hot, dense, and slow moving plasma fills in the line core so that the resulting tearing mode spectrum in Figure 1.4 panel (d) lacks the distinct double peaks as seen in the Petschek mode of panel (b).

The above two examples show that the spectroscopic signature of an EE can vary based on the type of reconnection that may be occurring. The example spectra presented in Figure 1.4 are fundamentally different, and should be easily distinguished by a spectrometer with sufficient spectral resolution. Thus, spectroscopy can serve as a diagnosis of the type of magnetic reconnection that results in an EE if the event can be captured by the spectrometer slit.

1.2.2 Alfvén Waves

MHD waves provide a source of energy transport into and through the solar atmosphere. Alfvén waves (transverse mode MHD waves that travel along magnetic field lines,[Alfvén, 1942]) are a particular example. These waves have been detected in numerous regions of the solar atmosphere [*e.g.* Tomczyk et al., 2007, Jess et al., 2009, Hahn et al., 2012, and the references cited therein]. Wave amplitudes on the order of 10's of $\mathrm{km\,s^{-1}}$ are sufficiently energetic to provide a means to heat the corona and power the solar wind [De Pontieu et al., 2007, McIntosh et al., 2011, Hahn and Savin, 2013].

The energy carried by an Alfvén wave can be converted to heat by damping of the wave in different regions of the solar atmosphere. Since the amplitude of the Alfvén wave contributes directly to emission linewidth [*e.g.* Hahn et al., 2012, Hahn and Savin, 2013], dissipation of wave energy is observed directly as a decrease in the non-thermal emission linewidth. In a particular example, Hahn et al. [2012] measured non-thermal linewidth as a function of height for the Fe IX, X, XII, XIII and the Si X ions using the Extreme Ultraviolet Imaging Spectrometer [EIS, Culhane et al., 2007] on board *Hinode* [Kosugi et al., 2007]. In this work, one end of the EIS slit was placed close to the limb and the length of the slit oriented radially outward from sun center so as to encompass a large portion of the corona. In this configuration, a decrease in the relative non-thermal linewidth as a function of height above the photosphere was detected, beginning at approximately $1.1R_\odot$ [Hahn et al., 2012].

The examples given for magnetic reconnection and Alfvén waves show that stigmatic spectroscopy allows the isolation of line profiles in particular solar structures; these profiles directly measure plasma motions in the solar atmosphere. In the case of magnetic reconnection, the line profile can be used to discriminate between rival descriptions of energy release. In the case of Alfvén waves, the line profile traces the flow and deposition of energy in the open parts of the lower corona. For both waves and reconnection events, the imaging component provides crucial details on morphology and the surrounding spatial context. For example, a spectrograph may see a red shift and a broadening at a particular point on the slit. Only an image can distinguish whether this spectrum originates from an isolated explosive event or from a flare ribbon that crosses the slit. The insights described above cannot be obtained through imaging alone or by spectroscopy alone.

1.2.3 The IRIS PSF

The state-of-the-art *Interface Region Imaging Spectrograph, (IRIS)* is a small explorer spacecraft that provides simultaneous spectra and slit-jaw images of the photosphere, chromosphere, transition region, and corona [De Pontieu et al., 2014]. *IRIS* is currently the highest spatial (0.33-0.4$''$) and spectral (2653 mÅ) resolution space-based solar observatory in operation. Instrumental effects, such as optical aberration, diffraction, and stray light, can significantly alter the line profile observed by *IRIS* and other imaging spectrometers. Thus, how the above plasma motions described in the previous section are interpreted through line profiles can depend significantly on how well the instrument is calibrated. In Chapter 3 of this thesis, I derive on orbit point spread functions (PSFs) for the spatial axis of the *IRIS* spectrograph. *IRIS* has undergone extensive calibration on the ground prior to launch [De Pontieu et al., 2014]; the work described in Chapter 3 is part of an ongoing effort to supplement and maintain this calibration for the instrument. To help establish the importance of PSF characterization, here I describe how the instrument PSF can contribute to the uncertainty in the examples of explosive events and Alfvén waves discussed above.

For stigmatic spectrometers, instrumental resolution can be broadly classified into two functions. The PSF describes the mapping of an infinitesimally small point source to the spatial axis of the instrument, while the line spread function (LSF) describes the mapping of spectral line source, *i.e.* monochromatic "line" illumination, to the spectral axis. Optical aberration (and other effects) will cause the image of the line and point sources to appear artificially broadened along their respective axes when imaged at the detector plane. The result is that the image at the detector is "blurred" by the convolution of the PSF and LSF (along their respective axes) with the original scene.

The effect of the PSF and LSF on the spectra observed by the instrument is detailed schematically in Figure 1.5. In panel (a) of Figure 1.5, convolution of the signal with the PSF blurs intensity from spatially adjacent pixels. In the example shown, this causes two spatially adjacent spectral signals with different center wavelengths to appear as a spectrally broad signal with a single central peak that spans multiple spatial pixels. Moreover, centroiding each of the resultant line profiles would result in an underestimate of the velocities of these two features. In Figure 1.5

(b), convolution of the signal with the LSF causes a loss of spectral resolution by blending two spectrally distinct peaks into a single, broad spectral signal.

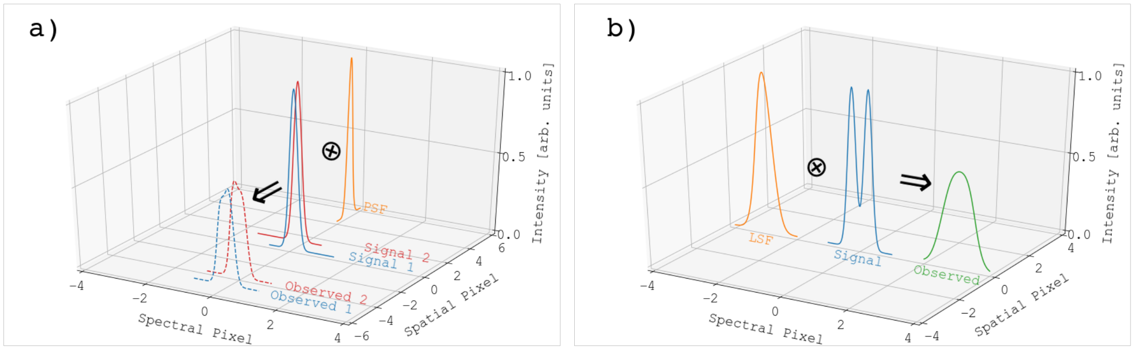

Figure 1.5: Input and observed signals to scale; scale of PSF and LSF increased for visualization; typically the PSF and LSF are normalized to unity. Convolution is represented by the ⊗ operator. Panel (a): The PSF causes signals from spatially adjacent signals to be blurred together. (b): The LSF causes blurring of spectrally adjacent features of the input signal. Both functions impact spectral resolution through different mechanisms.

In the study of magnetic reconnection in EEs, it is clear that the spectral distribution of intensity in the line profile plays an important role in determining the underlying reconnection mode at work. However, both the instrument PSF and LSF can work to obfuscate the underlying reconnection mode(s). For example, panels (a) and (b) of Figure 1.5 show that critical spectral features are lost to blurring by the PSF and LSF. In the context of an EE, this results in a loss of distinction between Petschek and tearing mode types of reconnection (*e.g.* the similarity in line profile observed between both panels of Figure 1.5).

In the Alfvén wave study by Hahn et al. [2012], the contribution to linewidth due to wave damping was about one-tenth of the EIS spectral pixel separation of 0.0022 nm/pixel; a fraction of the ∼0.006 nm full width at half max EIS line spread function (LSF). To observe wave damping as a function of height, Hahn et al. [2012] sampled linewidth at several positions along the EIS slit. This required the characterization of the EIS LSF as a function of position along the slit by Hara et al. [2011], so that wave broadening could be distinguished from the variation in the LSF along the slit and stray light within the instrument [Moran, 2003, Dolla and Solomon, 2008].

These cases illustrate two specific roles that instrument spatial and spectral resolution can play in stigmatic spectroscopy. In Chapter 3, I demonstrate how the PSFs I obtained can alter the line profile of an EE. The spatially gradual effects observed by Hahn et al. [2012] required a well characterized LSF at several points along the EIS slit; in more general cases, where the characteristics of the line profile are of interest, detailed characterization of the instrumental broadening (*e.g.* the LSF) is needed to determine the amount of non-thermal broadening in the line profile [*e.g.* Peter, 1999, Akiyama et al., 2005, Dudík et al., 2017]. These examples show that a good understanding of instrumental effects is crucial to many aspects of solar spectral observations.

1.3 Limitations of Slit-Spectrographs

Section 1.2 describes specific examples of what can be learned about the solar atmosphere from a slit spectrograph. However, these works also help illustrate some handicaps specific to slit spectrographs in VUV solar observations. Some of these limitations are described in this section.

It is difficult, if not impossible, to directly capture the full spatial and temporal variability of many solar events with the 1D FOV offered by a slit spectrograph. The model of a solar flare by Kopp and Pneuman [1976] in Figure 1.6 is an intuitive example. In this model, there will be plasma inflows and outflows associated with the reconnection region, similar to the Petschek and tearing mode models described earlier. In addition, chromospheric evaporation, or upflows due to the gas pressure of heated chromospheric plasma [*e.g.* Shibata and Magara, 2011], will fill the corona with hot plasma that rises along the magnetic loops from their footpoints as indicated in Figure 1.6. After reconnection, plasma trapped by the loops cools and condenses, falling back to the chromosphere. This model of a flare presents plasma at a variety of temperatures and velocities, which can potentially be observed with a slit spectrograph. However, imagining a straight line drawn through any two points in Figure 1.6 to represent the spectrograph FOV, it is difficult (or perhaps impossible) to capture both the reconnection flows and the chromospheric evaporation or condensation from both sides of the flare arcade.

Similar to the above argument, the slit also enforces a particular geometry on the Alfvén wave observations described earlier; Hahn et al. [2012] assumed that the magnetic field is directed radially outward and parallel to the length of the EIS slit. Imposing only a slightly more complicated magnetic field geometry would make following the propagation of the Alfvén waves with a slit spectrograph difficult, if not impossible.

From the flare loop and Alfvén examples it is clear that the situation could be improved by increasing the FOV beyond what a 1D slit provides. Ultimately, what is desired in both these situations is the ability to obtain a 3D datacube; a large FOV 2D "image" with a full spectrum available at each pixel. Such a data cube would allow the full context of a flare or MHD wave event to be investigated without being subject to the geometrical constraints of a spectrograph slit.

Stepping the spectrograph slit, or rastering, across the scene is one method to build a 3D spatial/spectral data cube. A major drawback to the raster approach is that the cadence is often slower than the evolutionary timescale of the solar features under investigation. For example, in a post-flare loop study by Czaykowska et al. [1999], CDS took ∼9 minutes to build a $160'' \times 160''$ raster covering the entire loop

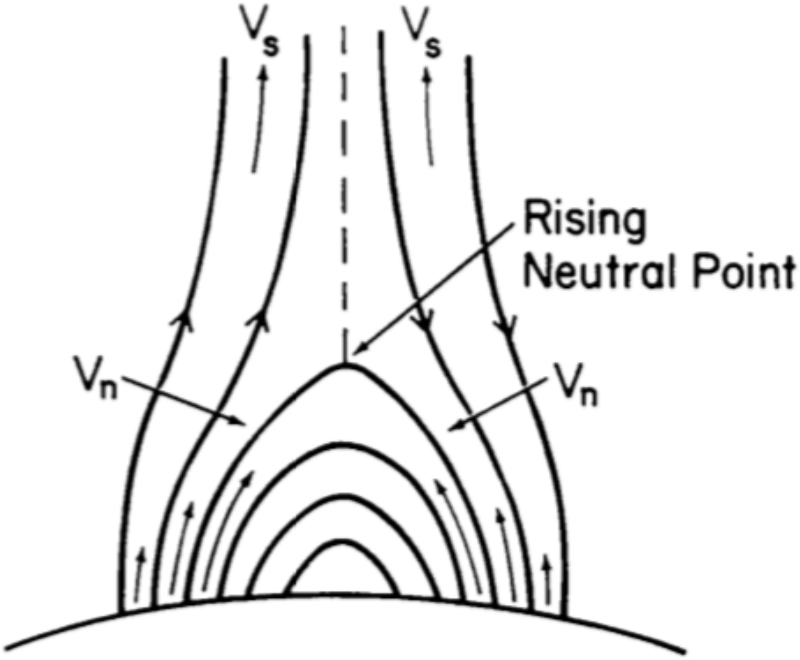

Figure 1.6: Standard model of magnetic reconnection in a flaring region from Kopp and Pneuman [1976]. Note the difficulty in choosing a pointing for a spectrograph slit that captures all regions of interest such as the flare footpoints, outflows, and reconnection regions.

area. A timescale for cooling of plasma suspended in the post-flare loops can be estimated by taking the ratio of the internal energy of plasma in the corona ($3n_ekT$) to the rate of radiative energy loss:

$$\Delta t = 3n_ekT/n_en_hQ(T)\,, \tag{1.2}$$

where n_e and n_h are electron and hydrogen number densities, respectively, k is the Boltzmann constant, T is temperature, and $Q(T)$ is the radiative loss function. In the corona, $n_e \approx n_h$ so that

$$\Delta t = 3kT/n_eQ(T)\,. \tag{1.3}$$

For the CDS observations, the maximum temperature observed corresponds to the Fe XIX emission line at $T = 8.0\,\mathrm{MK}$. At this temperature, assuming $n_e = 10^{10}\,\mathrm{cm}^{-3}$, $Q(T) = 3 \times 10^{-23}\,\mathrm{erg\,cm}^3/\mathrm{s}$ from the CHIANTI database [Young et al., 2019] using the coronal abundances profile. Under these assumptions, the timescale for radiative cooling in the post-flare loops is about $\Delta t = 6$ minutes, just over half the time it took CDS to complete one raster across the loop region. This means that the plasma suspended in a loop could have cooled significantly by the time CDS completed a single raster, with all of the plasma in the loop having completely cooled by the time the slit arrived at the same pointing for the second time. The relevant timescales show that rastering can obfuscate the temporal evolution of a post-flare loop arcade in this example.

The simplest technique available to slit spectroscopy is the sit-and-stare method. The slit is held stationary so that temporal confusion is avoided. In this mode of operation, clever (or more often fortuitous) positioning of the slit is used to capture the time dependence of an event at a single location. An example is the study by Brannon [2016] on the cooling and the subsequent draining of plasma in a flare loop arcade. In this work, the *IRIS* slit was positioned so that it intersected multiple loops across a flare arcade, with the slit spanning nearly from footpoint to footpoint. With this positioning, Brannon [2016] was able to approximate a single loop from multiple samples at different positions along the loops in the arcade.

The drawback to this approach by Brannon [2016] is that there is some ambiguity as to what the compound loop represents due to the spatial sampling of the slit. For example, it is impossible to tell from this slit positioning whether all of the loops in the arcade are governed by the same space–time evolution or if independent temporal and spatial variations in the emitting plasma exist within each individual loop. Some ambiguity could be removed by rastering across a single loop in its entirety, or a larger portion of the loop arcade, however, the same pitfalls will be encountered regarding slit geometry and rastering as discussed earlier.

Another drawback of the sit-and-stare method is that the spatial context is limited by the slit FOV. Take as an example a particular flare ribbon observed by the *IRIS* spectrograph. Both Brosius and Daw [2015] and Brannon et al. [2015] analyzed quasi-periodic intensity and velocity fluctuations in TR emission lines from this event. However, in part due to the lack of context, the cause of these fluctuations are difficult to interpret; Brosius and Daw [2015] hypothesize that quasi-periodic magnetic reconnection or the periodic release of magnetic energy by an external resonator is the source of the intensity fluctuation. An analysis by Brannon et al. [2015] of this same region arrived at a different interpretation. Using the *IRIS* slit jaw imager for additional context, Brannon et al. [2015] detected a “sawtooth” substructure in the intensity of the flare ribbon. This substructure was found to correlate with fluctuations of the Si IV, O IV, and C II emission lines observed by the *IRIS* spectrograph. This leads Brannon et al. [2015] to suggest that the observed intensity variation is caused by a tearing mode or Kelvin-Helmholtz type instability, a very different mechanism than that suggested by Brosius and Daw [2015]. Hence, the limited FOV and lack of spectral context of this event leads to very different interpretations of the underlying mechanism at work.

There are also solar features that are difficult to fully capture with the current technology of slit spectrograph. EEs are a particular example. These features are small enough to be well sampled spatially with only a handful of rasters, but are difficult to fully observe because of their evolutionary timescales. In the study by Innes et al. [1997], SUMER took upwards of 60 s to raster across an entire EE. This timescale is on par with the average EE lifetime [Dere, 1994]. In this case, the temporal confusion introduced by rastering makes it difficult to ascertain whether the bi-directional jets emanating from an EE result from wholly spatial or temporal variation. Sit-and stare observation is an alternative strategy, but this risks capturing a non-representative portion of the EE, similar to the flare study by Brannon [2016]. In the sit-and-stare case, it is difficult to determine the reconnection process behind a particular EE from only a small spatial sample of the whole event, *e.g.* imagine trying to differentiate between Figure 1.4 (a) and (b) from only a small slice through each diagram. For these reasons, EEs present a tricky target to observe with only a slit spectrograph.

The examples presented here all serve to outline specific difficulties encountered in solar observations with slit spectrographs. The limitations are summarized as follows. The slit geometry is ill-suited to observe complex, extended, dynamic solar structures. Rastering to build the necessary context introduces temporal and spatial confusion, and the 1D sit-and-stare observing mode excludes critical nearby spectral context. These limitations, derived from the examples described herein, suggest a specific need for a different type of spectrograph.

1.4 Slitless Solar Spectroscopy

The limitations described in the previous section could be resolved by the ability to quickly build a 3D data cube, or in other words, the ability to perform simultaneous imaging and spectroscopy over a large 2D FOV. In visible wavelengths, a reasonable approximation to this type of product is made available by fast-tuneable Fabry–Perot etalons [*e.g.* Puschmann et al., 2012]. Unfortunately, materials that are transparent to VUV wavelengths simply do not exist to extend this technology shortward of $\sim$150 nm [*e.g.* Wuelser et al., 2000]. With this limitation in mind, I describe a different approach that eliminates the slit from a stigmatic spectrograph.

One of the first VUV slitless spectrographs was flown by the Naval Research

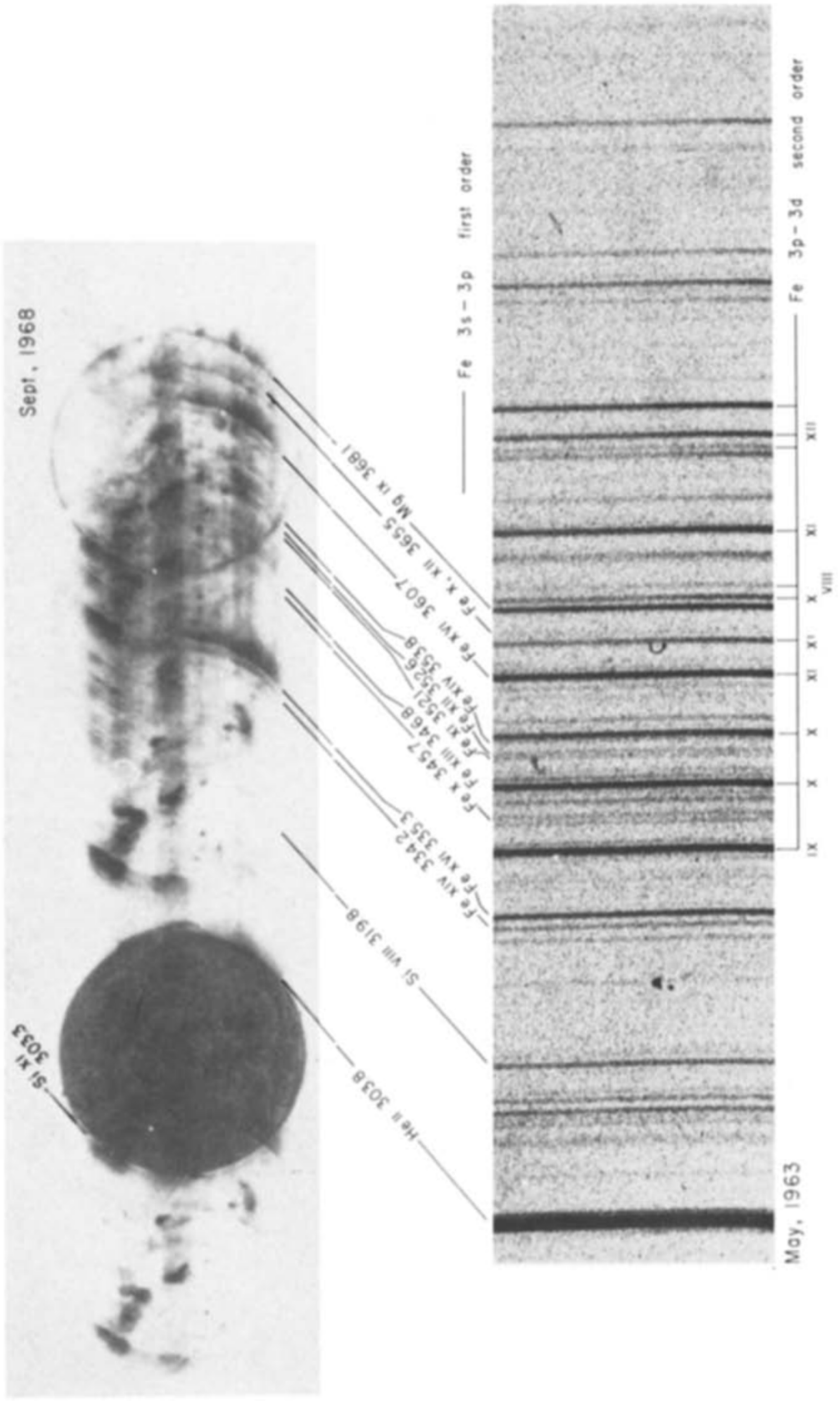

Figure 1.7: Left image, EUV spectroheliogram from the NRL sounding rocket. Note significant overlap exists even for widely spaced emission lines. Right image, grazing-incidence spectrum that identifies the spectroheliogram images. Images from Tousey [1986].

Laboratory (NRL) as a sounding rocket platform [Tousey, 1986] and later developed into the SO82A instrument on the Skylab Apollo telescope mount [Tousey et al., 1977]. An image from the NRL sounding rocket instrument is shown in the top panel of Figure 1.7; here, the FOV is large enough to capture multiple spectral images of the entire solar disc and portions of the corona in a single exposure. Each spectral image corresponds to a different bright EUV emission line (or blended line) identified by the grazing incidence slit spectrum in the lower panel of Figure 1.7 from a separate instrument. While this type of instrument does not deliver a complete spectrum at every pixel, the overall information content of a single image of this type is very large. For example, from the SO82A spectroheliograms it is possible to derive electron densities from several density-sensitive emission line ratios (*e.g.* Ca XVII [Doschek et al., 1977], Fe IX, [Feldman et al., 1978], Mg VII and Si IX [Keenan et al., 1986]).

As the body of work that emerged from SO82A shows, the major obstacle faced by slitless spectrographs is image overlap. In Figure 1.7 it is apparent that significant confusion exists in and near areas where spectral images fall on top of one another; in some cases, solar features are all but obscured by multiple images. Thus, the large FOV afforded by a slitless spectrograph comes in trade for an exponential increase in ambiguity caused by the mixing of spatial and spectral information.

The act of "inversion," defined here as the recovery of a 3D spatial/spectral data cube from a 2D projection, presents an ill-posed problem. One can imagine the difficulty in what is analogous to a tomographic reconstruction problem [Kak and Slaney, 1988]; *i.e.* recovering the shape and internal structure of a semi-opaque 3D object from its shadow projected onto a screen. In the case of SO82A, only one projection of the 3D spatial/spectral solar scene is obtained by the single diffraction order. In the tomographic analogy, knowledge of the 3D object is improved by obtaining shadows from multiple different projection angles. Correspondingly, what is sought in slitless spectroscopy is projections from multiple different diffraction orders. Computed Tomographic Imaging Spectrometers [CTIS, Okamoto and Yamaguchi, 1991, Bulygin et al., 1991, Descour and Dereniak, 1995] leverage this concept by obtaining multiple, simultaneous dispersed images from upwards of 25 grating diffraction orders onto a single detector plane [Descour et al., 1997].

There is a practical limit to the maximum number of projections obtained by a VUV solar slitless spectrograph. The spectral resolution of the CTIS instruments mentioned earlier is only $\lambda/\Delta\lambda \sim 10$, and the wavelength range covered is large (*e.g.* all of the visible spectrum, a factor of ~ 2 in wavelength). To attack the scientific problems outlined above regarding the energization of the solar atmosphere, a different approach is needed. Even a small wavelength range (a few percent) will typically have several spectral lines, perhaps formed at multiple temperatures, and the spectral resolution required to obtain line profiles is of order $\lambda/\Delta\lambda \sim 10,000$. This suggests a different arrangement, with large dispersion and widely separated detectors dedicated to each spectral order or channel. Moreover, a large detector area is needed to obtain a sufficient FOV with enough spatial resolution to resolve solar features; one projection per camera is appropriate. The number of cameras is limited by the spacecraft volume; only a handful of cameras will fit in a typical sounding rocket payload (*e.g.* Chapter 4). Thus, the approach of the Multi-Order Solar EUV Spectrograph [MOSES, Kankelborg and Thomas, 2001, Fox et al., 2010], is to use a single diffraction grating to form images at three cameras from the $m = 0$ and ± 1 diffraction orders.

Inversion of MOSES data amounts to a limited look-angle tomography problem. In lieu of additional projections, and in contrast to CTIS type instruments, the inversion is improved by multilayer EUV mirror coatings that limit the instrument spectral pass band. In this way, the MOSES inversion space is *a priori* confined to the segment of wavelengths surrounding just a few bright emission lines.

In the context of VUV solar spectroscopy, what is gained by the addition of more dispersed orders and the constraint on inversion space is access to higher order line moments. For example, the bandpass of the first flight of MOSES in 2006 was centered around the bright He II emission line. From the MOSES $m = +1$ and $m = 0$ orders, Fox et al. [2010] performed a "parallax" analysis by hand-fitting gaussians to the He II spectral profile for an isolated event in the MOSES FOV. Changes in position (line center) and linewidth of the profile between the two image orders are interpreted as Doppler shifts and broadening of the He II emission line. This enabled Fox et al. [2010] to identify this event as an explosive event with a bright core and distinct, anti-parallel but non-collinear jets. A more extensive investigation of several EEs in the MOSES He II data set was performed by Rust and Kankelborg [2019] using a similar parallax analysis technique. In this work, Rust and Kankelborg [2019] find at least 10 explosive events with bidirectional jets but a lack of core emission. This suggests Petschek mode reconnection rather than a tearing mode, in contrast to Innes et al. [2015]. Due to the large number of EEs identified, the observations by Rust and Kankelborg [2019] also suggest that EEs may have a greater diversity of morphology than previously observed by slit spectrographs and that a range of both tearing mode and Petschek type reconnection modes may be present [*e.g.* Rust, 2017, Rust and Kankelborg, 2019].

1.4.1 Challenges of Slitless Spectroscopy

As with any instrument, there is a unique set of difficulties associated with a slitless spectrograph. MOSES, for example, has three disparate PSFs associated with each image order [Rust, 2017] that simultaneously obfuscate the spatial and spectral content of an individual pixel. As a result, any inversion that compares a pair of MOSES image orders is subject to spectral artifacts caused by the differing image

PSFs. For example, spurious low velocity emission observed in the core of some TR EEs could result from MOSES PSF artifacts [Rust and Kankelborg, 2019]. The characterization of EEs with MOSES is therefore subject to limitations imposed by the instrument spatial and spectral resolution, similar to the discussions given for SUMER and *IRIS* in Section 1.2. Improving or avoiding such limitations is a major theme of this dissertation.

In Chapter 2, I describe an alternative method for deriving only Doppler shifts from a pair of MOSES dispersed images. Conceptually similar to the parallax techniques described earlier, this method is based on local correlation tracking [LCT, November and Simon, 1988] to quantify feature shifts along the dispersion axis in the MOSES images. This work makes use of the PSF characterization by Rust [2017] and is presented as an alternative method to obtain Doppler shifts from MOSES data. An advantage of this method is that it is designed to be more robust when faced with differing image PSFs.

Aside from disparate PSFs, inversion of MOSES data is complicated by other aspects of the optical design. In Chapter 4, I describe the EUV Snapshot Imaging Spectrograph (ESIS) instrument, which is a next generation slitless spectrograph derived from the concept proven by MOSES. In Section 4.2, I give a detailed comparison of the MOSES and ESIS designs, and the advantages of the new ESIS concept gained through experience with MOSES.

To conclude this section, it is worth stating that the two spectrometer types discussed in this chapter (slit- and slitless) are complementary rather than exclusive. MOSES and ESIS target a small segment of the solar EUV spectrum, containing at most a few emission lines. The intent of these instruments is to image and recover only one or two line profiles over a large 2D FOV in this small slice of spectrum. For this reason, a MOSES type instrument is not likely to discover or identify new spectral lines, or, for example, estimate the density of H_2 from relatively weak molecular hydrogen lines [*e.g.* Jaeggli et al., 2018] in sunspots. Slit spectrographs that can unambiguously isolate and resolve large numbers of individual lines, such as HRTS, SUMER and *IRIS*, are much better suited to these tasks. Thus, MOSES and ESIS are designed to uncover the dynamics and evolving morphology of a particular spectral line spread over a large FOV, while SUMER and *IRIS* excel at the more classic task of measuring a spectrum with many lines.

1.5 Summary of Dissertation Chapters

Each chapter that follows is a separate project within a body of work, organized to reflect the progression of the discussion above. Here, I give a brief summary of the content of each chapter.

In Chapter 2, I describe an efficient automated method for extracting Doppler velocities from any pair of (co-temporal) MOSES images. In contrast to the work by Fox et al. [2010] and Rust [2017], I obtain the Doppler shifted component of the line profile for every pixel in a MOSES image rather than a limited region, however, this is at the expense of recovering the higher order line moments. The method is also insensitive to background, so that Doppler shifts can be diagnosed over the entire MOSES FOV. This has the potential applications of identifying large-scale or widely spread small-scale trends in mass and energy flow in MOSES (or ESIS) images.

Chapter 3 details my contributions to calibration/characterization and data processing efforts of the IRIS observatory. In this work, I used a transit of Mercury across the Sun to derive on-orbit point spread functions (PSFs) for the near (NUV) and far ultraviolet (FUV) channels of the *IRIS* slit-jaw spectrograph. This is the first on-orbit characterization of the spectrograph spatial resolution. I show that the PSF in the NUV channel influences interpretation of small scale features (in this case, a small explosive event); in the FUV channels, the instrument PSF does not significantly influence the interpretation of this same feature. Also developed in this work is a PSF deconvolution routine to correct the PSF contribution in the *IRIS* spectra. The PSFs and a simple deconvolution routine are included in the SolarSoft [Freeland and Handy, 1998] library for public distribution to users of *IRIS* data.

In Chapter 4 I describe the EUV Snapshot Imaging Spectrograph (ESIS), in which I had a major design role. ESIS is a sounding rocket based slitless imaging spectrometer that is the logical continuation of MOSES. In this chapter, I compare specifics of the ESIS and MOSES instruments, describe the scientific objectives for the new instrument, and detail how ESIS is designed to meet these objectives. I have tried to collect as much of the significant details of the ESIS as possible into this chapter, so that Chapter 4 can serve as a definitive reference for this new instrument.

Finally, this dissertation concludes with Chapter 5, where I present the key points, relevance and significance, and potential avenues of future study from each of the three preceding chapters.

CHAPTER TWO

USING LOCAL CORRELATION TRACKING TO RECOVER SOLAR SPECTRAL INFORMATION FROM A SLITLESS SPECTROGRAPH

Contribution of Authors and Co–Authors

Manuscript in Chapter 2

Author: Hans T. Courrier

Contributions: Conceived and implemented study design. Constructed code to analyze and display data sets. Wrote first draft of the manuscript.

Co–Author: Charles C. Kankelborg

Contributions: Helped to conceive study. Provided guidance regarding analysis and comments on drafts of the manuscript.

Manuscript Information

Hans T. Courrier, Charles C. Kankelborg

Journal of Astronomical Telescopes and Imaging Systems, SPIE

Status of Manuscript:
____Prepared for submission to a peer–reviewed journal
____Officially submitted to a peer–reviewed journal
____Accepted by a peer–reviewed journal
__x__Published in a peer–reviewed journal

Published by SPIE the international society for optics and photonics
Published January, 2018, JATIS, 4(1), 018001

ABSTRACT

The Multi-Order Solar EUV Spectrograph (MOSES) is a sounding rocket instrument that utilizes a concave spherical diffraction grating to form simultaneous images in the diffraction orders $m = 0$, $+1$, and -1. MOSES is designed to capture high-resolution co-temporal spectral and spatial information of solar features over a large 2D field of view.

Our goal is to estimate the Doppler shift as a function of position for every MOSES exposure. Since the instrument is designed to operate without an entrance slit, this requires disentangling overlapping spectral and spatial information in the $m = \pm 1$ images. Dispersion in these images leads to a field-dependent displacement that is proportional to Doppler shift. We identify these Doppler shift induced displacements for the single bright emission line in the instrument passband by comparing images from each spectral order.

We demonstrate the use of local correlation tracking as a means to quantify these differences between a pair of co-temporal image orders. The resulting vector displacement field is interpreted as a measurement of the Doppler shift. Since three image orders are available, we generate three Doppler maps from each exposure. These may be compared to produce an error estimate.

2.1 Introduction

The transition region is the portion of the solar atmosphere between the million degree corona and the much cooler chromosphere. In order to understand the underlying physical mechanisms that result in this temperature disparity, it is necessary to characterize the solar atmosphere in the spatial, temporal, and spectral domains. Spectrographic observations point to a number of mechanisms by which the corona may be heated. Large scale Alfvénic waves with amplitude $\approx 20\,\mathrm{km\,s^{-1}}$ and periods of $100 - 500s$ have been observed in the transition region and corona by McIntosh et al. [2011] and are energetic enough to power the quiet corona and fast solar winds. Magnetic reconnection may also play a part in heating the corona, [Longcope and Tarr, 2015] and can be observed as spatially compact explosive events (EEs) in the transition region and upper solar atmosphere [Dere, 1994, Dere et al., 1991]. These events contrast Alfvén waves with much shorter lifetimes ($\approx 75s$) and Doppler velocities on the order of $100\,\mathrm{km\,s^{-1}}$ (See Fox et al. [2010], and references therein). Imaging either of these events with a slit style spectrograph can be challenging, and is usually the result of a combination of fortuitous positioning of the spectrograph slit, rastering, and exposure timing.

The Multi-Order Solar EUV Spectrograph (MOSES) [Kankelborg and Thomas, 2001, Fox et al., 2010] is a sounding rocket based snapshot imaging spectrograph. MOSES obtains high cadence ($\approx 10s$) spectral and spatial information simultaneously over a 20’ x 10’ field of view (FOV) by omitting the entrance slit usually associated with rastering type spectrometers [Fox et al., 2010]. The high spatial resolution (0.6” pixels) and large FOV of MOSES makes it possible to capture a multitude of EEs and traveling wave phenomena within a single exposure. MOSES shares this characteristic with other ground based instruments, such as the Computed Tomography Imaging Spectrometer (CTIS) [Descour and Dereniak, 1995], and the ground based observations made by DeForest et al. [2004] using the Advanced Stokes Polarimeter (ASP) on the Dunn Solar Telescope at the National Solar Observatory. Much like these two instruments, the increased field of view and temporal resolution of MOSES comes at a cost. While MOSES can easily obtain co-temporal spectral and spatial information over a large FOV, disentangling the overlapping spectral and spatial information in the MOSES dispersed images presents an ill posed inversion problem.

The MOSES instrument utilizes a concave spherical diffraction grating to form images of $m = 0$, $+1$, and -1 diffraction orders on three 2048 x 1024 rear-illuminated CCDs. A schematic of the grating and imaging detectors is shown in Fig. 2.1. The top, center, and bottom detector planes in Fig. 2.1 image the $m = +1$, 0, and -1 spectral orders respectively. The spatial axis is the same in all three spectral orders, however the direction of the dispersion axis is reversed between the $m = \pm 1$ orders. The images formed in these two orders are not redundant. When imaging an object that has some spectral width, components that are redward of the instrument passband center (the letter “A” in Fig. 2.1) are shifted away from the $m = 0$ order CCD in the $m = \pm 1$ order images. Conversely, the blueward components of the object (“B” in Fig. 2.1) are shifted towards the $m = 0$ order CCD. There is no dispersion in the $m = 0$ order images; intensity in this order is simply a function of position integrated over the instrument passband. Multilayer coatings and thin film filters limit the instrument passband to a few spectral lines, the brightest of which is the Lyman alpha transition of He II at 30.4 nm. More information about instrument specifics can be found in Fox et al. [2010].

Any pair of MOSES spectral orders contains information about Doppler shifts [Kankelborg and Thomas, 2001]. Fox et al. [2003] proposed a pair of inversion techniques to solve the ill-posed problem of obtaining a spectrum for each pixel in a MOSES image. We propose a solution to a better posed problem; estimating just the Doppler shift from the strong He II line. Most of the solar emission within the instrument passband comes from this emission line. Doppler shifts are estimated by cross-correlating corresponding patches of two simultaneous images to determine a local shift vector. The shift vector component parallel to the image dispersion direction then corresponds to the Doppler shift. This method is based on a stereoscopic inversion method described by DeForest et al. [2004] for ground based magnetography. The Fourier Local Correlation Tracking (FLCT) [Fisher and Welsch, 2008] routine is employed as a fast and efficient means of performing the cross-correlation and generating subsequent per pixel vector displacement fields for image pairs. There are two advantages to performing the inversion with local correlation tracking; (1) correlation is not affected by differing background levels in image pairs and (2) the method can track intensity in the dispersed and non-dispersed axis of the images, allowing some compensation for differing aberration between image orders. In Sec. 2.2, we prepare a synthetic data set that simulates MOSES flight data. We use this synthetic data to characterize the spatial and spectral response of the FLCT method in the context of a MOSES like data set, paying particular attention to how differing point spread functions in the three spectral orders influence FLCT-derived Doppler shifts. We then use the results of Sec. 2.2 and FLCT to generate Dopplergrams of MOSES data collected during the Feb. 2006 flight [Fox et al., 2010] in Sec. 2.3.

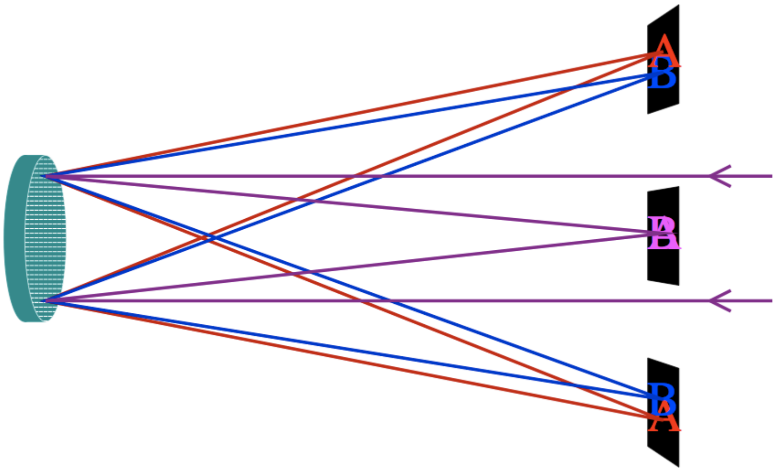

Figure 2.1: Schematic diagram of the MOSES instrument. Incident light on the right forms an undispersed image on the central $m = 0$ CCD. Dispersed images are formed on the outboard $m = \pm 1$ CCDs.

2.2 Methodology

In this section we demonstrate how we use FLCT to perform the stereoscopic inversion between image pairs of the MOSES instrument. MOSES has three diffraction orders that are imaged simultaneously. This results in three independent image pairs for each exposure; $m = 0, +1$, $m = 0, -1$, and $m = +1, -1$. The inversion process can be described by three high level operations: (1) FLCT determines displacement vectors for each pixel in an image pair; (2) the displacement vector array is converted into a line-of-sight (LOS) velocity array using the known instrument dispersion; (3) 'Dopplergrams' are created by overlaying the color-coded LOS velocities onto the $m = 0$ image. In Sec. 2.2.1 we determine the best FLCT parameters to reconstruct the Doppler velocity from MOSES data, and in Sec. 2.2.2 we investigate artifacts that result from instrument aberration and the FLCT-based inversion method.

2.2.1 FLCT Parameters

FLCT is a computationally efficient implementation of the local correlation tracking (LCT) method developed by November and Simon [1988] to quantify proper motion measurements of solar granulation. A variety of LCT techniques have been developed to infer 'optical flow' from brightness patterns in a sequence of solar images (*e.g.* Schuck [2006] and references therin). The optical flow is a 2-d field that, when applied to the scalar field of an image, results in the best reproduction of the next image in the sequence. In this context, the 2-d field can be used to estimate velocities perpendicular to the line of sight (LOS). For MOSES, the optical flow between image orders corresponds to spectral shifts, which we use to estimate Doppler velocites. The fourier implementation [Fisher and Welsch, 2008] of LCT uses a fast and straightforward approach that is easily adapted to finding displacements between MOSES image orders.

Pursuant to its originally intended purpose, FLCT has five input arguments: (1) amount of time between input images; (2) unit of length of a single pixel; (3) optional threshold parameter to skip flow calculation for pixels based on input image intensities; (4) optional low pass filtering parameter applied in the FFT domain; (5) characteristic width, σ, of a Gaussian windowing function applied to the input images. To output displacement vectors in pixels from FLCT, we set the ratio of the first two input arguments equal to unity. The optional threshold and low pass filtering parameters are not used. In this section we discuss how we threshold FLCT output and choose the windowing parameter σ to provide the best stereoscopic inversion of MOSES data.

We choose to threshold FLCT output based on the MOSES $m = 0$ order image intensity for two reasons; (1) it places the FLCT-derived displacement vectors (Doppler shifts) over the $m = 0$ order image, rather than the abstracted spectrally ‘smeared’ images produced by the $m = \pm 1$ orders, (2) As we explain below, FLCT tends to shift the velocity field when comparing $m = 0$ to $m = \pm 1$; thresholding using $m = 0$ intensity minimizes this effect. In general, LCT methods track features by finding the maximum correlation between subsets of two images. Ideally, the best correlation will be found where the subsets of each image overlap. Hence, LCT will find a displacement field in between the initial and final locations of a feature that appears in both images. Since we want to know the physical locations of Doppler shifts, we require the FLCT-derived displacement field between MOSES image orders to originate from the $m = 0$ order intensities. The shift in velocity field is demonstrated in Fig. 2.2, where FLCT has generated displacement vectors between two images of identical Gaussians ($\sigma = 2$ pixels) using a larger windowing function with $\sigma = 3$. An exaggerated displacement field is created by shifting one image four pixels horizontally with respect to the other. The dashed box centered over the left Gaussian marks the nominal correlation window size of 2σ. While correlations are possible outside of this box, the purpose of the windowing function is to discourage correlations for comparatively large displacements. In Fig. 2.2 the displacement vectors are shifted to the right side of this box, to a point in between the two images, rather than over the left Gaussian. Thresholding Dopplergrams generated from the two outboard order images based on the zero order intensity helps compensate for this offset of the Doppler velocities.

The optimal value of σ is largely dependent on the size scales present in our images [Fisher and Welsch, 2008, DeForest et al., 2004]. MOSES images the solar transition region, which is highly dynamic. Small compact explosive events (spatial size on the order of a few MOSES pixels) are associated with Doppler shifts of tens to hundreds of $\mathrm{km\,s^{-1}}$ [Dere et al., 1989, Fox et al., 2010]. In general smaller values of σ result in finer resolution in the displacement field, while larger values are better

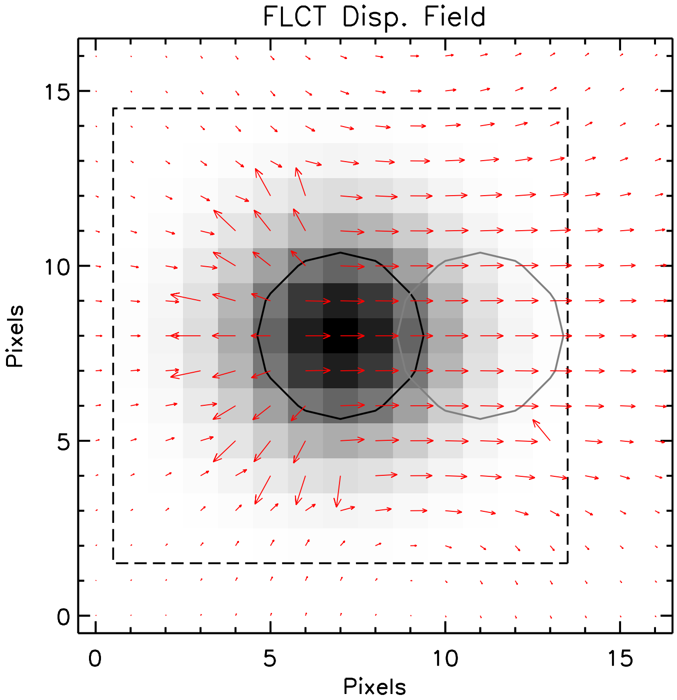

Figure 2.2: FLCT-generated displacement vectors for a Gaussian that has been shifted four pixels to the right. The black contour is drawn at half maximum intensity. The gray contour marks the same and identifies the location of the shifted image. The dashed box marks 2σ for the FLCT windowing function ($\sigma = 3$), centered over the unshifted image; correlations outside of this box are considered unlikely. Displacement vectors are scaled to fit within one pixel.

suited to reproducing larger shifts and reduce artifacts due to the differing size of the PSF for each image order. One major limitation of FLCT (and all local correlation techniques) is that spatial resolution of the extracted Doppler shift is affected by the correlation window size [DeForest et al., 2004, Descour and Dereniak, 1995]. This effect is illustrated by the dashed box in Fig. 2.2, which marks where the Gaussian windowing function drops below four orders of magnitude for $\sigma = 3$. There must be sufficient features contained within this box for FLCT to derive a displacement vector, as the windowing function makes correlations increasingly unlikely for features that are located further away. Fortunately the solar transition region is finely structured, and acknowledging this limitation, we use knowledge of the MOSES instrument aberration for each image order to set a lower limit for σ.

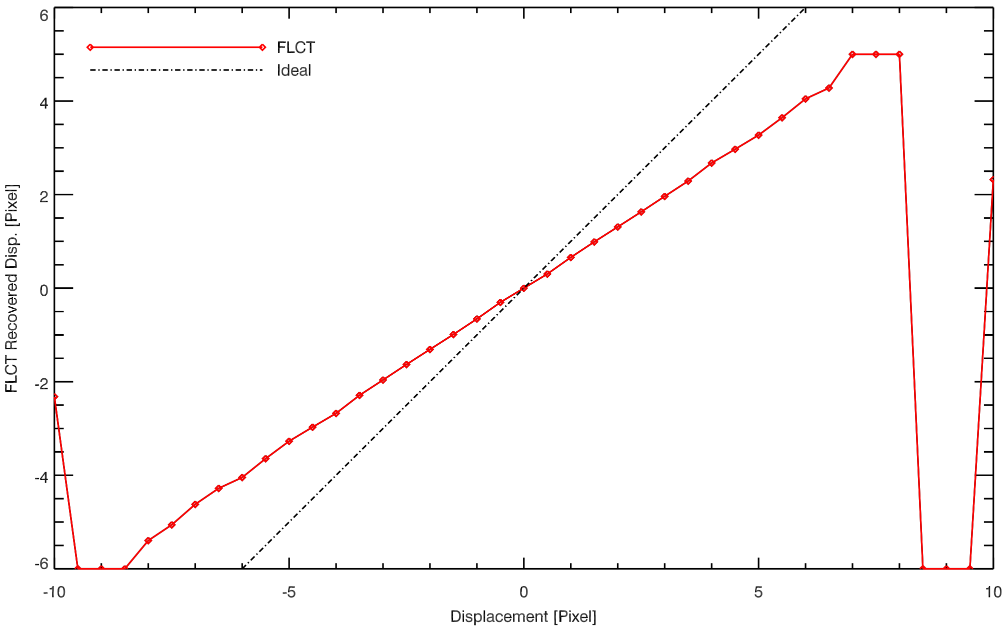

Figure 2.3: FLCT-generated vs. true displacement between the pair of symmetrically displaced, identical Gaussian functions described in Fig. 2.2.

FLCT consistently recovers the displacement of correlated features that fall within the window set by σ. This is shown in Fig. 2.3, where the displacement between the pair of identical Gaussian functions described earlier is varied from complete overlap (*i.e.* zero displacement) in half-pixel increments, then plotted against the value recovered by FLCT. For all cases, $\sigma = 3$. In Figure 2.3, the distribution of displacements recovered by FLCT is approximately linear between ±6 pixels, although the magnitude of displacement is consistently undervalued, an artifact of the method noted elsewhere (*e.g.* Freed et al. [2016], and the references therein). For this reason, the displacement recovered by FLCT should be considered a lower limit on the true displacement. For greater than six pixel displacements, the distribution of the FLCT recovered values quickly becomes unstable, indicating that FLCT is having difficulty finding the correct correlation when the magnitude of the displacement exceeds 2σ. Thus, FLCT-derived Doppler shifts that correspond to values of greater than 2σ pixel displacements should be considered unreliable.

The top row of Fig. 2.4 shows 2D estimates of the MOSES point spread functions (PSFs) for each image order, estimated by Rust [2015]. A contour is drawn at half maximum intensity that indicates the size and shape of each PSF. As seen in Fig. 2.4 the three PSFs extend differently over several pixels along the horizontal (dispersed) and vertical (non-dispersed) axes. The bottom row of Fig. 2.4 shows line spread functions (LSFs) for the dispersed axis of each image order, obtained by summing over the vertical axis of the corresponding 2D PSF. The width of each LSF is estimated by a least-squares Gaussian fit. Modulation Transfer Functions (MTFs) derived from the LSFs of Fig. 2.4 are plotted in Fig. 2.5. MTFs for normalized Gaussian functions of $\sigma = 2$ and 3 are overplotted in dashed lines. Both Fig. 2.4 and Fig. 2.5 highlight the differences in imaging quality of the three MOSES image orders.

The disparity in aberration between image orders is a primary consideration in our selection of two dimensional FLCT as an inversion method. The difference in aberration between image orders causes intensity information, and thereby spectral information, to be mapped differently into each of the MOSES image orders. Vertical displacement between image pairs is wholly a result of instrument aberration, since this axis is not dispersed. On the other hand, horizontal displacement is due to some combination of the spectral content of the signal and instrument aberration. We include the vertical component of displacement, so that signal that has moved in this

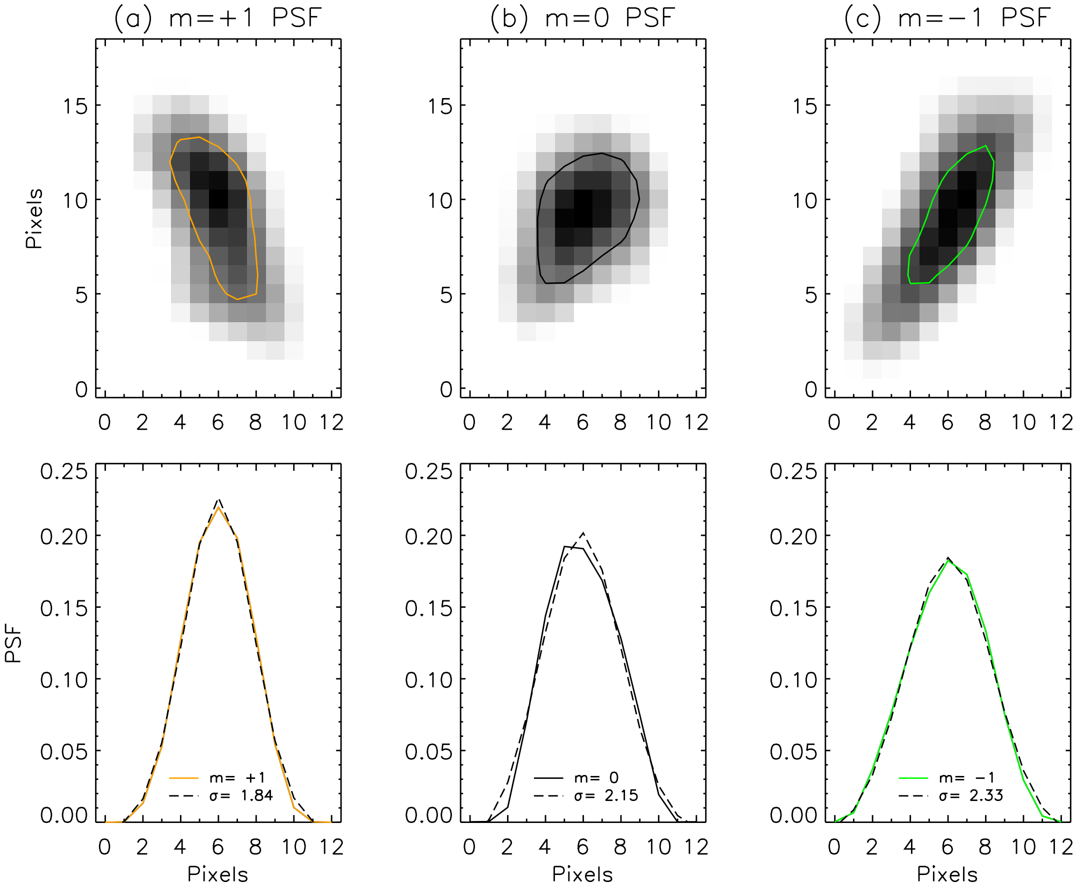

Figure 2.4: Estimates of the MOSES $m = +1$, 0, and -1, image order PSFs in columns (a), (b), and (c), respectively. The contour is drawn at half maximum intensity for each PSF image in the top row. In the bottom row, line spread functions are formed by summing along the vertical axis of the PSF image directly above. A Gaussian with characteristic width σ is fit to each LSF in the bottom panels, and overplotted as dashed curves.

direction due to PSF differences can be identified and tracked. This is illustrated by the FLCT-generated displacement vectors for two simplified cases in Fig. 2.6.

In Fig. 2.6(a)- 2.6(c), we estimate the instrument response to a monochromatic point source with no Doppler shift. In this case the point source is not shifted in the $m = \pm 1$ orders, so that the centroids of the PSF for each image order are co-located.

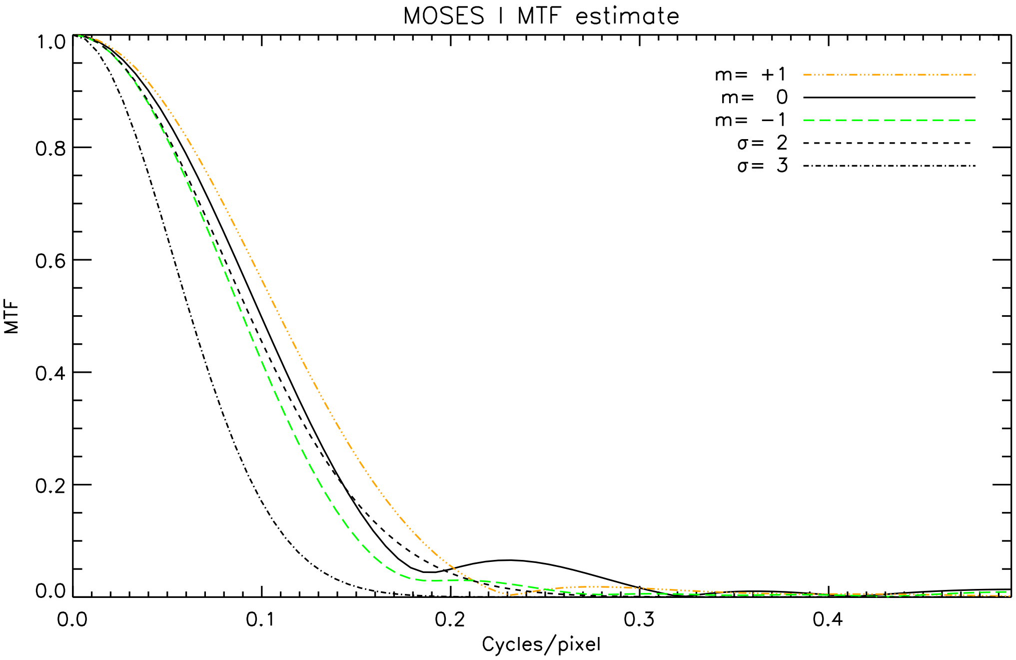

Figure 2.5: MTFs for each of the MOSES image orders, derived from the LSFs of Fig. 2.4. Overplotted in dashed and dash-dot curves are MTFs of FLCT Gaussian windowing functions with $\sigma = 2$ and 3.

In Fig. 2.6 panel (a) and (b) FLCT draws displacement vectors from the $m = 0$ to the $m = +1$ and -1 image orders respectively, while the vectors are drawn from the $m = +1$ to the $m = -1$ image order in panel (c). In these three panels the horizontal displacement vectors are near zero where the PSFs overlap in each image pair. Artificial displacement vectors appear where one PSF extends beyond the other in each image pair; we investigate this in greater detail in Sec. 2.2.2. A window size of $\sigma = 3$ was used to generate the displacement vectors in all panels, based on the MTFs from Fig. 2.5. Since FLCT finds a corresponding point in the $m = \pm 1$ for every point in the $m = 0$ PSF in Fig. 2.6, and similarly for for the $m = +1$ to $m = -1$ in panel (c), we assert that $\sigma = 3$ is sufficiently large to resolve this case.

In Fig. 2.6(d)- 2.6(f), FLCT generates displacement vectors for a monochromatic

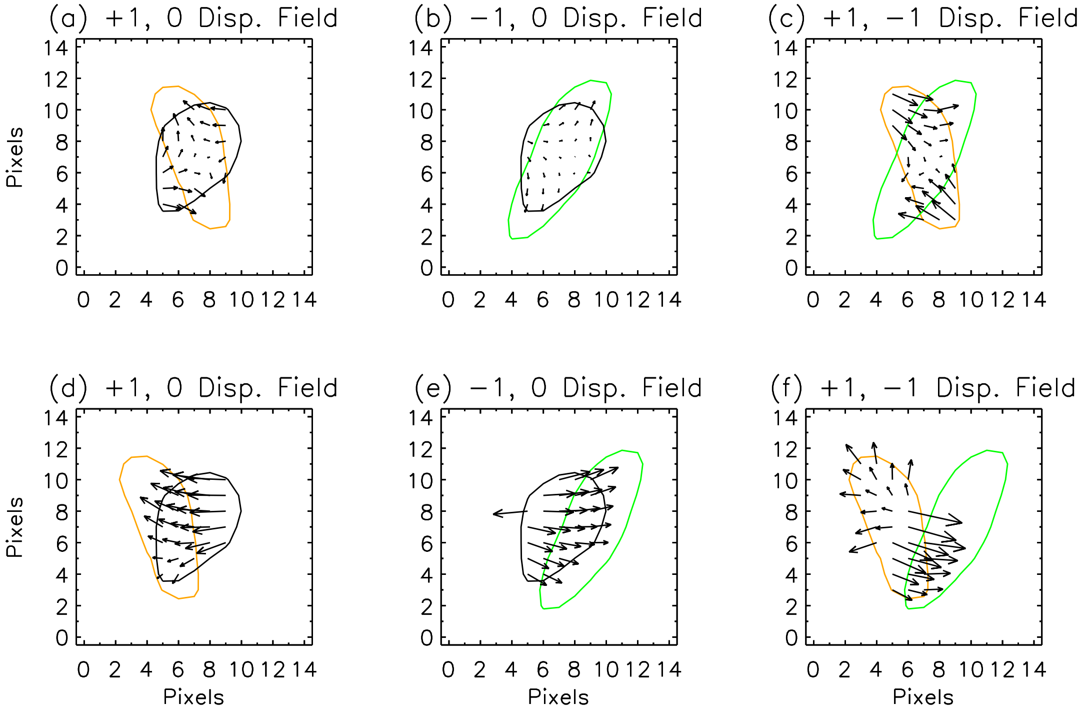

Figure 2.6: FLCT-generated displacement vectors for a point source based on the PSF estimates of Fig. 2.4. Panels (a)-(c), the signal is monospectral. Panels (d) and (e), dispersion is added by means of a two pixel redward shift in the $m = \pm 1$ orders. This appears as a four pixel shift in (f) due to the symmetry of the instrument.

point source with a known Doppler shift. Each of these three panels are similar to the one above, however a $58\,\mathrm{km\,s^{-1}}$ red shift has been simulated by translating the $m = +1$ PSF leftward two pixels in Fig. 2.6 panel (d) and the $m = -1$ PSF rightward by the same amount in panel (e). This appears as a four pixel displacement between PSF centroids in Fig. 2.6 panel (f) due to the symmetry of the instrument. This two pixel displacement is well reproduced over the whole of the $m = 0$ PSF in panels (d) and (e) of Fig. 2.6, albeit with some errors in the non-overlapping portions resulting from the differing PSF shapes noted earlier. The window size of $\sigma = 3$ remains sufficient to resolve this case for the image pairs in these two panels. In Fig. 2.6 panel (f), FLCT has failed to correlate the upper portion of the $m = +1$ to the $m = -1$ PSF. This is due in part to the elongated form and differing orientation of the PSFs as well as the increased displacement for a given Doppler shift for this image pair. Experimentation has shown that $\sigma = 5$ is a sufficiently large window size to map all of the intensity of the $m = +1$ PSF into the $m = -1$ PSF.

From these two cases we conclude that setting the FLCT window parameter $\sigma = 3$ for the $m = 0, +1$ and $m = 0, -1$ image pairs and $\sigma = 5$ for the $m = +1, -1$ provides the optimal resolution for our inversion method.

2.2.2 Inverting Synthetic Data

To investigate how the FLCT-based inversion method recovers Doppler information from closely spaced sources, synthetic images that simulate the basic structure of compact and dynamic events observed by MOSES were generated and analyzed. Two test cases are considered in panels (a) of Fig. 2.7 and Fig. 2.8; an unresolved, and marginally resolved case, respectively. For both cases, the synthetic images consist of adjacent red, blue, and unshifted point sources. Point sources with Doppler shifts are colored blue or red to indicate direction, while the magnitude of the shift is $29\,\mathrm{km\,s^{-1}}$ for either direction in accordance with the legends in Fig. 2.7 and Fig. 2.8. In panel (a) of both Fig. 2.7 and Fig. 2.8 the point source located at (25,11) has zero spectral linewidth, while the point source at (25,40) has a linewidth of $29\,\mathrm{km\,s^{-1}}$. These two test cases help to visualize the combined resolution limits of the imaging system and inversion method.

To mimic the MOSES instrument response for each image order, the synthetic images are first convolved with the appropriate PSF estimate from Fig. 2.4. Poisson noise is then added to each image, resulting in an approximation to compact, dim

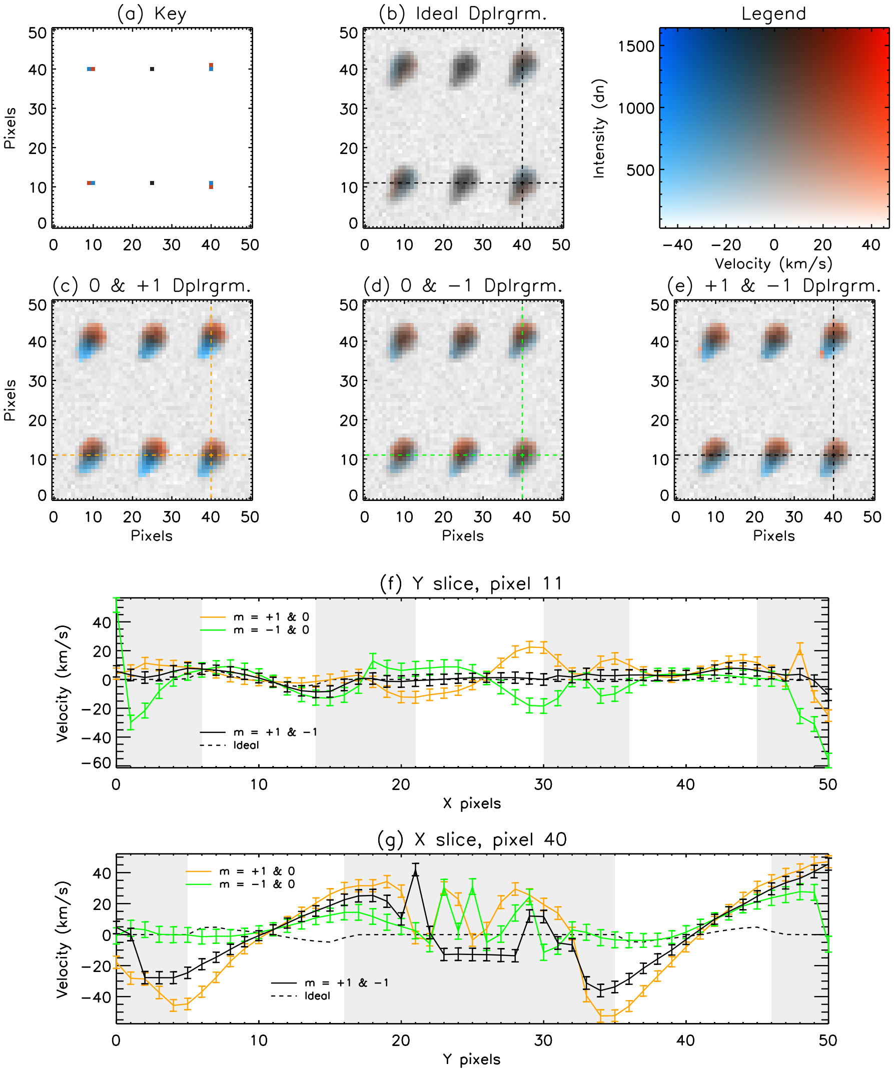

Figure 2.7: Dopplergrams of synthetic images that mimic the MOSES instrument response to spatially unresolved point sources. The color indicates line shift in km s^{-1} while color saturation shows intensity. Panel (a) is the original input image, (b) is the expected instrument response. Panels (c), (d), and (e), are the inversion results for each image pair. Horizontal and vertical cuts of each Dopplergram are (indicated by dashed lines in panels (b)-(e)) plotted with error bars in panels (f) and (g), respectively. Gray regions plots (f) and (g) indicate where Doppler velocities have been thresholded out of the Dopplergrams. Inversion results are dominated by systematic errors from instrument aberration (discussed in the previous section text) in this case where the point sources are not sufficiently resolved.

events observed throughout the field of view of MOSES. The signal to background for the $m = 0$ synthetic images is $\sim$2.9, set in a background with mean of 424 counts. FLCT is then used to generate displacement vectors for each of the $m = 0, +1$, $m = 0, -1$, and $m = +1, -1$ image order pairs.

Dopplergrams from each of the image pairs are shown in panels (c)-(e) of Figs. 2.7 and 2.8. The component of the FLCT-derived displacement vectors parallel to the dispersion axis is converted to LOS velocity by multiplication with the instrument dispersion. The magnitude of the MOSES dispersion is $29\,\mathrm{km\,s^{-1}}$ per pixel for the $m = 0, +1$ and $m = 0, -1$ image pairs and $14.5\,\mathrm{km\,s^{-1}}$ per pixel for the $m = +1, -1$ image pair. The factor of two in difference in dispersion is due to the anti-symmetry of dispersion of the $m = \pm 1$ image orders noted earlier. Dopplergrams are created by overlaying color coded LOS velocities from each image pair on the $m = 0$ order image. In Figs. 2.7 and 2.8 the Dopplergrams are thresholded by binning the $m = 0$ order image counts into halves and ignoring those velocities corresponding to the dimmest half for clarity. Plots (f) and (g) of Figs. 2.7 and 2.8 show horizontal and vertical cuts through Dopplergrams (b)-(e). The gray background in these two plots indicate where Doppler velocity has been thresholded in the corresponding Dopplergrams. Non-thresholded Doppler velocities are shown in these regions to help characterize systematic errors in the inversion. Error bars indicate estimated uncertainty in Doppler velocity due to random intensity errors in the data, derived in Appendix A.

An additional Dopplergram is shown in panel (b) of Figs. 2.7 and 2.8. These Dopplergrams present the expected distribution of Doppler velocity information of the synthetic images after convolution with the $m = 0$ order PSF. The velocity field displayed on the $m = 0$ order image, $v'(x, y)$, is derived from the known velocity field,

$v(x, y)$, of the synthetic images by

$$v'(x, y) = \frac{I(x, y)v(x, y) * \kappa}{I(x, y) * \kappa}\,, \tag{2.1}$$

where $I(x, y)$ is the intensity of the $m = 0$ order image in counts, κ is the $m = 0$ order PSF estimate, and $*$ is the convolution operator. Weighting $v(x, y)$ by intensity prevents the velocity signal from a point source from being 'diffused' when convolved with κ, an unphysical situation since we measure Doppler velocity indirectly via displacement of the dispersed intensity. This weighting maintains the magnitude of the (artificial) velocity signal over an extended source, approximating the real distribution of intensity when convolved with the MOSES PSFs. These 'ideal' Dopplergrams then illustrate how the Doppler information encoded into our synthetic images is distributed in the $m = 0$ order images.

Contrasting Doppler shifts in sources separated by only one pixel will not be resolved using FLCT with $\sigma = 3$ or $\sigma = 5$ window. This is illustrated in Fig. 2.7(c)-2.7(e), where the inversion is dominated by spurious Doppler shifts resulting from instrument aberration for all three image pairs. These artifacts appear as red shifts near the top of the re-imaged point source, and blue shifts near the bottom, in panels (c)-(e) of Fig. 2.7. For each of the three image pairs, the inversion returns similar results for all point sources regardless of their spectral content. Comparing Fig. 2.7 (c),(d), and (e) to the ideal Dopplergram in panel (b), there is little correlation in Doppler velocity except where the orientation of point sources in panel (a) tends to match the orientation of the inversion artifacts. In Fig. 2.7 panel (f) there is some correlation with true Doppler velocity near pixel 10, where systematic errors from the PSFs align well with the Doppler shifted point sources in panel (a), however the inversion returns spurious shifts for the other two features. This is most notable in

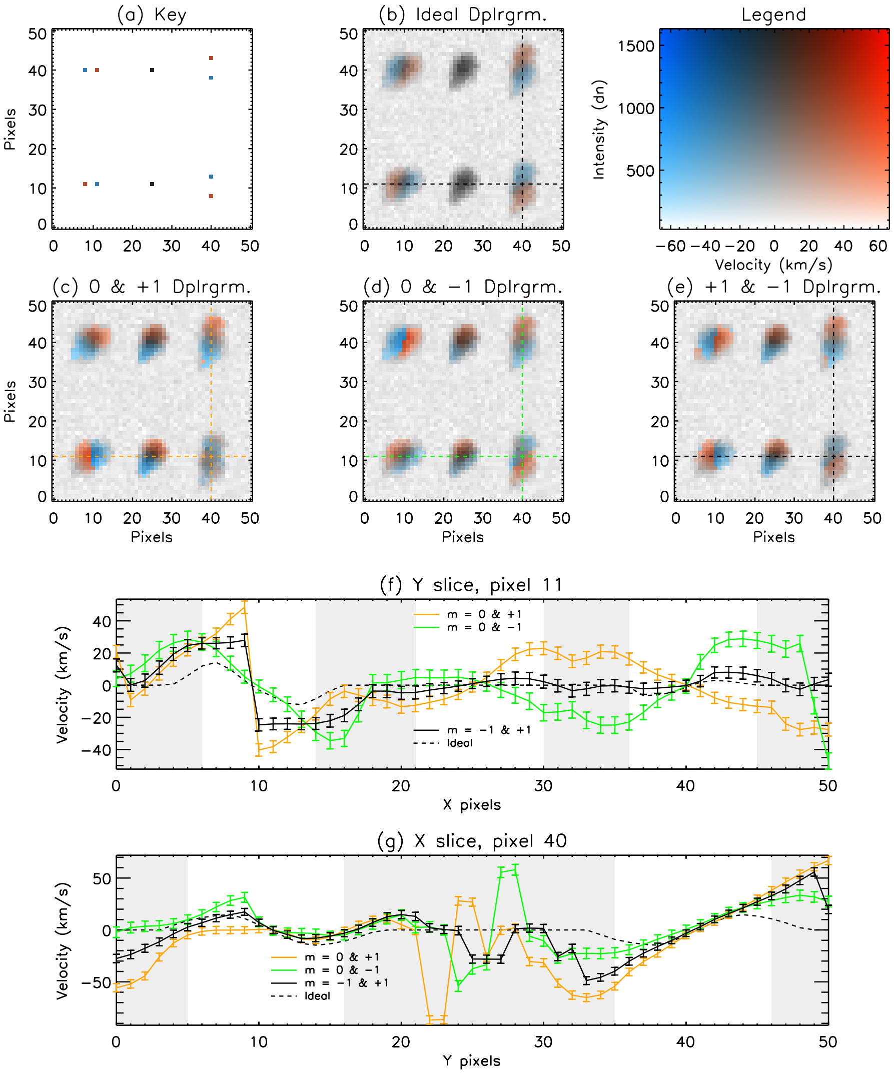

Figure 2.8: Dopplergrams with increased spatial separation between spectral point sources. Panel layout is the same as Fig. 2.7; the original input image is shown in panel (a). Artifacts contribute to the under- and over-estimation of Doppler velocity in panels (c), (d), and (e), compared to (b), see text for details.

Fig. 2.7 panel (f), where the extracted Doppler shift is nearly identical for the features located at pixels 10 and 40, despite the inverted Doppler velocities shown in panel (a). For this case where the spectral point sources are not well separated, the true Doppler shifts are overwhelmed by systematic error in the inversion.

The inversion method returns more favorable results when the separation between spectral point sources is increased. This is illustrated in Fig. 2.8 (a) where the horizontal separation between red and blue shifted point sources is increased to three pixels horizontally and five pixels vertically. This is still below the spatial resolution indicated by the MTFs in Fig. 2.5, however the additional spectral information allows us to resolve the point sources in Fig. 2.8 (a) in most cases. Comparing each of Fig. 2.8 (c), (d), and (e) to (a), the basic structure of panel (a) is well reproduced by the inversion of each of the three image pairs. Comparing these same three panels to Fig. 2.8 (b) shows that the inversion method reproduces the expected distribution of Doppler velocities, but overestimates the magnitudes. This overestimation of Doppler magnitude is attributed to the artifacts that result from differing instrument aberration pointed out in Fig. 2.7.

In Fig. 2.8 panel (f) the Doppler field offset discussed in Sec. 2.2.1 is evident near pixel 10. For the $m = 0, +1$ cut, the peak Doppler velocities occur near pixels 9 and 10, while lower peak velocities are reported by the $m = 0, -1$ cut at pixels 5 and 15. The Doppler field offset tends to smear the recovered Doppler signals together in the $m = 0, -1$ cut near pixel 10, resulting in a softening of the transition from red to blue shift. The inverse is true for the $m = 0, +1$ cut, as the recovered velocity field is smeared away from the transition area. The $m = -1, +1$ cut has a smoother response and the recovered signal tends to towards the average of the other two cuts near pixel 10.

The $m = 0, +1$ image pair does not resolve the Doppler velocities for the feature centered at pixel (40,11) in Fig. 2.8(a) and pixel 10 in panel (g). This is because the orientation of the point sources in Fig. 2.8 leads to an unfavorable configuration in the $m = +1$ image. In this case convolution with the $m = -1$ PSF causes the point sources to nearly overlap in the y-axis in this order, causing this feature to look nearly identical in the $m = 0$ and $m = -1$ orders. For this particular orientation of point sources, the y-axis resolution of the PSFs are the limiting factor. We note that the Doppler shifts of the opposite feature (pixel (40,40) in Dopplergrams and panel (f), pixel 40) is well resolved, as the alignment of PSFs is more favorable for this feature.

Despite these shortcomings, Figure 2.8 shows that FLCT is able to at least qualitatively reproduce Doppler shifts near the resolution limit for two images with differing PSFs. Moreover, sources separated by three pixels are resolved even when a $\sigma = 5$ FLCT window is used (*e.g.* Fig. 2.8). In most cases the inversion method reproduces the general structure of the point sources (i.e. finding the correct sign of Doppler shift), however systematic errors tend to under- or over-estimate the magnitude of the Doppler shifts.

2.3 Inverting MOSES Data

In this section, we apply FLCT Doppler estimation to representative images and features from solar observations obtained with MOSES. The MOSES instrument was launched February 8, 2006 from White Sands Missile Range, New Mexico. Over the course of approximately five minutes, 27 exposures were taken above 160 km. Data from this flight have been dark subtracted, the $m = \pm 1$ order images co-aligned to the $m = 0$ order, and optical distortion removed from all images. Intensities are in units of data numbers (DN) per second. Exposures are normalized so that each image has the same mean DN s^{-1} as the exposure with least atmospheric absorption, the fourteenth exposure [Fox, 2011]. We generate Dopplergrams over the entire instrument FOV for each set of exposures in this image set guided by the results of Sec. 2.2. A value of $\sigma = 3$ is used for the the $m = 0, +1$ and $m = 0, -1$ image pairs while $\sigma = 5$ for the $m = +1, -1$ image pair.

A Dopplergram generated from the $m = -1$ and 0 orders of the twenty-fourth exposure is shown in Fig. 2.9. In this exposure, the orange boxed feature in Fig. 2.9 is fully developed and has also been analyzed in Fox et al. [2010], Fox [2011]. The color map is scaled to $\pm 150\,\mathrm{km\,s^{-1}}$ as the majority of Doppler velocities fall within this range. Groups of white pixels in the FOV and the band of white pixels across the left side and top of the image are a result of bad, missing, or saturated pixels in one or more image orders. The image in Fig. 2.9 exemplifies the co-temporal spectral and spatial data the MOSES instrument collects over a large field of view within a single exposure. Several small, isolated features that show characteristics similar to transition region explosive events [Fox et al., 2010, Dere et al., 1989] appear in these exposures. Two of these features are shown in the orange and green boxed areas of Fig. 2.9, and in greater detail in Fig. 2.10 and Fig. 2.11, respectively.

The feature depicted in Fig. 2.10 is the same explosive event analyzed by Fox et al. [2010]. Our analysis produces similar structure, with the core of the feature largely red shifted, becoming blue shifted in the lower wing and red shifted near the tip of the upper wing. Unlike the analysis by Fox et al. [2010], we resolve the upper wing as mostly blue shifted, only becoming red shifted towards the tip. We also find the core of the feature to be red shifted. The differing offset of this red shift in Fig. 2.10 panels (a) and (b) is due to the Doppler field shift, described in Sec. 2.2.1. Based on our analysis in previous sections, the true position of this red shift is more closely reproduced in panel (c). Blue shifts are also affected by the Doppler field offset, leading to a softening of the transition from red to blue in the $m = 0, -1$ and $m = 0, +1$ cuts of Fig. 2.10 panel (d) near pixel 32 and 19, respectively. Despite these systematic errors, this event appears well resolved by the inversion method as all three Dopplergrams report similar velocities and structure in Fig. 2.10 panel (d).

The feature depicted in Fig. 2.11 has some hidden complexity. This appears to be an entirely blue shifted event in the $m = -1, +1$ Dopplergram, however a red shift

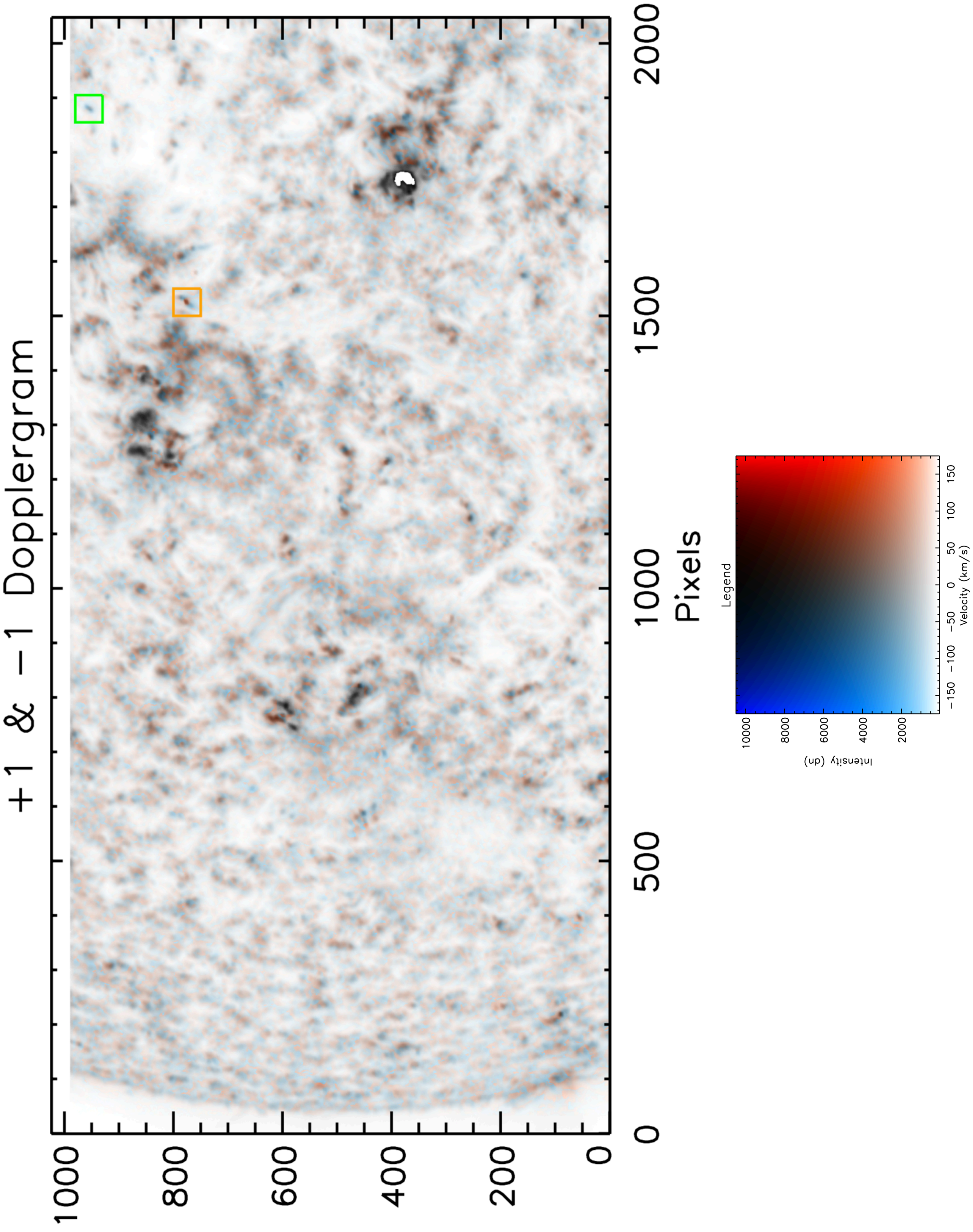

Figure 2.9: Top panel, FLCT-generated Dopplergram of a MOSES exposure from the $m = +1$ and -1 order images. White pixels are bad or missing data. Orange and green boxed areas shown in greater detail in Fig. 2.10 and Fig. 2.11 respectively. Bottom panel, Doppler velocity and intensity legend for the Dopplergram above.

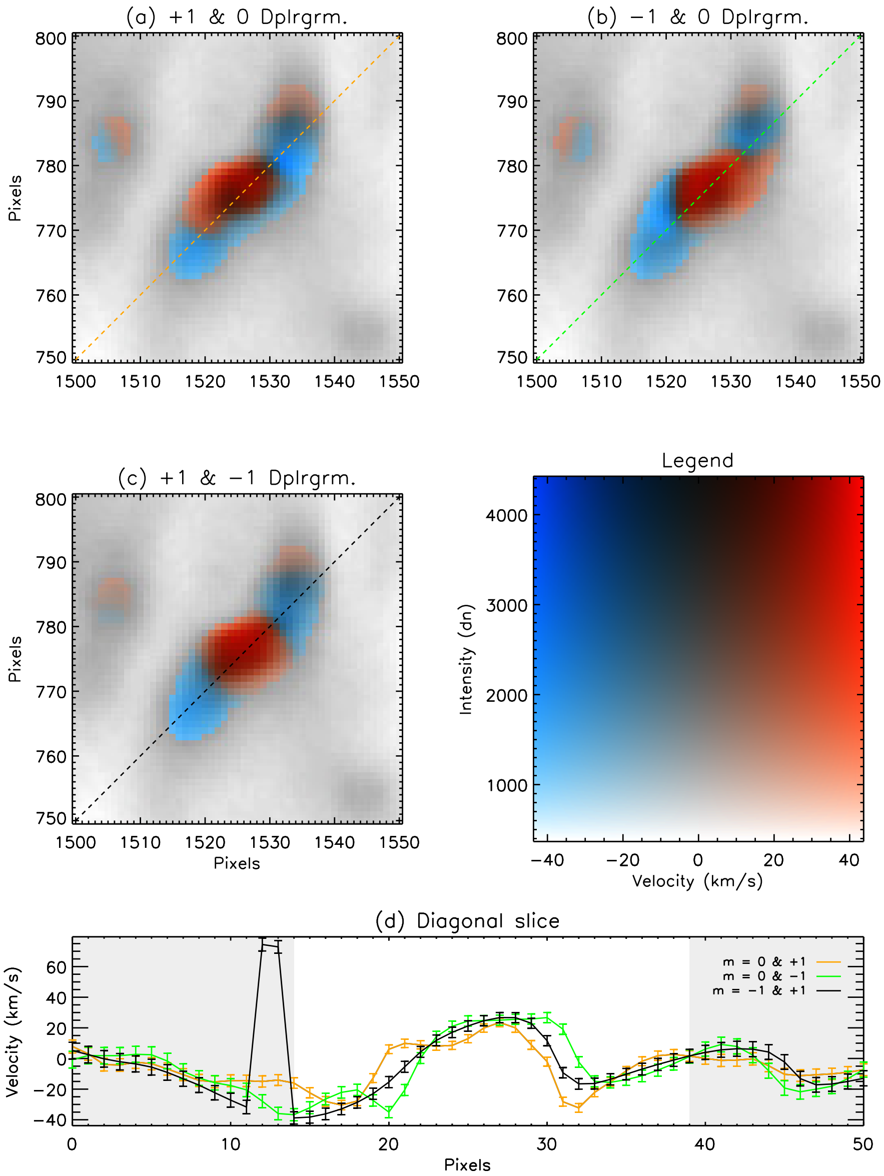

Figure 2.10: Dopplergrams of a compact bi-directional explosive event observed by MOSES (a) +1 & 0, (b) −1 & 0, and (c) ±1 image orders. Diagonal cuts through the Dopplergrams (panels (a)-(c), dashed lines) are plotted in panel (d). The differing location in each panel of the red shifted core of this event is an artifact of the inversion method, discussed in Sec. 2.2.

near the center of the feature is registered in both panels (a) and (b) of Fig. 2.11. This indicates this feature is only partially resolved by our inversion method and may be a compact version of the event in Fig. 2.10, with a red shifted core and blue shifted wings extending to the north and south. The Doppler field offset spreads the red and blue shifts away from the core of the event in Fig. 2.11 panels (a) and (b) (similar to panels (a) and (b) of the Fig. 2.10), and PSF artifacts may contribute to overestimation of the peak red and blue shifts. The red shift near center is not resolved in Fig. 2.11 panel (c) from a combination of unfavorable PSF alignment and the larger correlation window size in this Dopplergram. The $m = 0, +1$ and $m = 0, -1$ velocity cuts in Fig. 2.11 panel (d) show that the red shifts extend nearly to the core of the feature in each case, also indicating that a red shift may be buried in the core of this feature.

2.4 Discussion and Conclusions

The MOSES instrument is designed to provide simultaneous imaging and spectroscopic information in a single snapshot over a wide field of view. To accomplish this, MOSES collects simultaneous EUV images in three spectral orders of a concave diffraction grating. Here we have demonstrated, on both synthetic and real data, the derivation of Dopplergrams from image pairs using local correlation tracking. Applications of FLCT to actual MOSES data in Sec. 2.3 show some promising results. Strong events such as those shown in Fig. 2.10 and Fig. 2.11 look broadly similar whether the Dopplergram is generated from the $m = 0, +1$, $m = 0, -1$, or $m = +1, -1$ order image pairs. Comparing the features of Fig. 2.11 to the synthetic images of Fig. 2.8, it is clear that resolving the Doppler shifts of adjacent features located within one PSF radius ($\sim$3 pixels) is near the limitations of our FLCT-based method. However, for a $\sigma = 3$ and even $\sigma = 5$ window, the spatial resolution of our

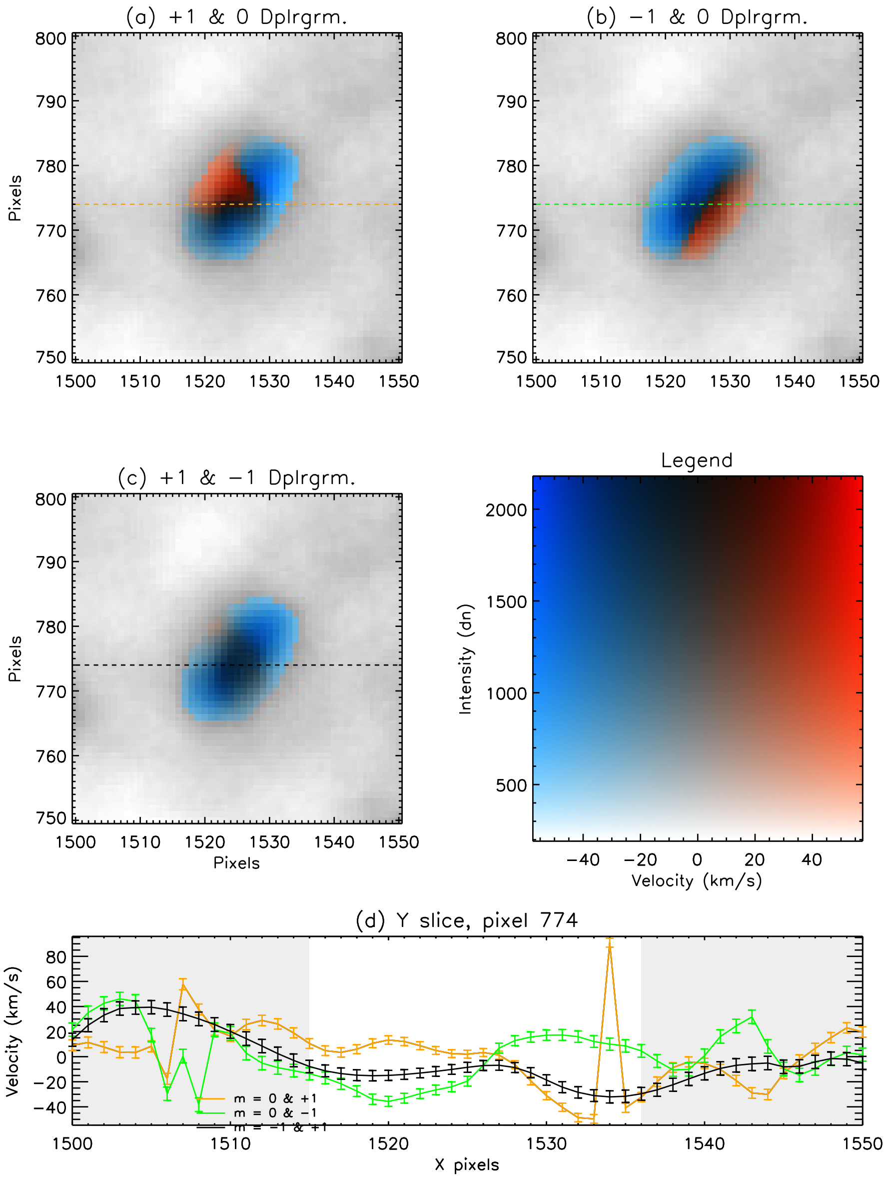

Figure 2.11: Compact explosive event observed by MOSES; panel layout is the same as Fig. 2.10. Offset red shifts in panels (a) and (b) may indicate this event has a redshifted core. This red shift is not resolved in panel (c). See text for details. Horizontal cuts through the Dopplergrams (panels (a)-(c), dashed lines) are plotted in panel (d).

Doppler maps is only modestly degraded in comparison with the original intensity maps (*e.g.* panel (d) of Fig. 2.8 in which Doppler shifts are resolved for sources three and five pixels apart). DeForest et al. [2004] employed a difference of image intensity integrals along the dispersion axis to capture the finest details. Before we can reach that level of detail with MOSES data, we will need to apply explicit PSF correction [Atwood and Kankelborg, 2018]. In Sec. 2.2, we show the origin of systematic errors that mainly affect poorly resolved structures. Some of these systematic errors are due to the differing PSFs of each image order. While the inversion method can compensate for some degree of disparity between PSFs of the image orders, and the three available Dopplergrams help identify these systematic errors, the method would be improved treating PSF errors in the data prior to analysis. A procedure that equalizes PSFs between image orders (*e.g.* the procedure by Atwood and Kankelborg [2018]) could reduce or eliminate these systematic errors, and may be preferable to deconvolution of the PSF estimates.

It is also apparent from Sec. 2.2 that FLCT systematically shifts the locations of the Doppler shifts. This unfortunately hampers quantitative, pixel-by-pixel comparison of the Dopplergrams derived from the $m = 0, +1$, and $m = 0, -1$ image orders. It would be helpful to develop a similar algorithm that places the Doppler shifts (displacement vectors) at the source locations in the $m = 0$ order image, rather than between the $m = \pm 1$ and $m = 0$ order images. Once this shortcoming is addressed, we expect to be able to better assess and improve our Doppler shift estimates by comparing and perhaps combining results gained from different image order pairs.

Moving forward, our strategy will be (1) Remove or reduce PSF contributions in the MOSES data; (2) develop a local correlation tracking algorithm that minimizes or eliminates the offset of the displacement field; (3) Apply this algorithm to both synthetic and real MOSES data, as we have done in this study.

2.5 Acknowledgements

This work was supported by the NASA Heliophysics Sounding Rocket Program, grant number NNX14AK71G.

CHAPTER THREE

AN ON ORBIT DETERMINATION OF POINT SPREAD FUNCTIONS FOR THE INTERFACE REGION IMAGING SPECTROGRAPH

Contribution of Authors and Co–Authors

Manuscript in Chapter 3

Author: Hans T. Courrier

Contributions: Conceived and implemented study design. Helped to obtain data sets. Constructed code to analyze data sets. Wrote first draft of the manuscript.

Co–Author: Charles C. Kankelborg

Contributions: Helped to conceive study. Provided guidance on analysis and comments on drafts of the manuscript.

Co–Author: Bart De Pontieu

Contributions: Constructed code to obtain data sets. Provided feedback of analysis and comments on drafts of the manuscript.

Co–Author: Jean-Pierre Wülser

Contributions: Constructed code to obtain data sets. Provided feedback of analysis and comments on drafts of the manuscript.

Manuscript Information

Hans T. Courrier, Charles C. Kankelborg, Bart De Pontieu, Jean-Pierre Wülser

Solar Physics

Status of Manuscript:
____Prepared for submission to a peer–reviewed journal
____Officially submitted to a peer–reviewed journal
____Accepted by a peer–reviewed journal
_x_ Published in a peer–reviewed journal

Published September, 2018, Solar Physics, 293(125)

ABSTRACT

Using the 2016 Mercury transit of the Sun, we characterize on orbit spatial point spread functions (PSFs) for the Near- (NUV) and Far- (FUV) Ultra-Violet spectrograph channels of NASA's *Interface Region Imaging Spectrograph (IRIS)*. A semi-blind Richardson–Lucy deconvolution method is used to estimate PSFs for each channel. Corresponding estimates of Modulation Transfer Functions (MTFs) indicate resolution of 2.47 cycles/arcsec in the NUV channel near 2796 Å and 2.55 cycles/arcsec near 2814 Å. In the short (≈1336 Å) and long (≈1394 Å) wavelength FUV channels, our MTFs show pixel-limited resolution (3.0 cycles/arcsec). The PSF estimates perform well under deconvolution, removing or significantly reducing instrument artifacts in the Mercury transit spectra. The usefulness of the PSFs is demonstrated in a case study of an isolated explosive event. PSF estimates and deconvolution routines are provided through a SolarSoft module.

3.1 Introduction

Images from a telescope are often well approximated as a convolution of the real scene with the instrument point spread function [PSF, *e.g.* Hecht, 1987]. The PSF describes the response of such an imaging system to a point source of light, altering the perfect mapping of light from the observed object to the image plane of the instrument. The PSF and its Fourier amplitude, the MTF, are widely used for evaluating the performance of a telescope or optical system [*e.g.*, Hecht, 1987, Goodman, 2005, DeForest et al., 2009].

The Sun is an extended, high-contrast, and (often) finely structured source in extreme-ultraviolet (EUV) wavelengths [Walker et al., 1988, Golub et al., 1990, Antolin and Rouppe van der Voort, 2012]. Observations of such scenes may be subtly smoothed (or blurred) by an instrument PSF, reducing contrast between adjacent bright and dark features. This can affect many different types of measurements, in particular those involving feature photometry [DeForest et al., 2009]. For example, Shearer et al. [2012] found that the PSF scattering wings of the *Extreme-UltraViolet Imager* (EUVI) instrument aboard STEREO-B could significantly alter the diagnostics of temperature and density in coronal holes on the solar disc. Instrument artifacts in solar scenes may be significantly reduced through deconvolution when the PSF is known [*e.g.*, DeForest et al., 2009, Poduval et al., 2013] or by blind methods where the scene and the PSF are estimated concurrently [Karovska et al., 1994, Golub et al., 1999]. Therefore, a realistic estimate of the instrument PSF is desirable for quantitative interpretation of solar observations.

The *Interface Region Imaging Spectrograph* [IRIS, De Pontieu et al., 2014] is a dual channel solar spectrograph (SG) and slit-jaw imager (SJI) operating in Sun-synchronous orbit since 27 June 2013. As IRIS is a space based observatory, it is not subject to atmospheric distortion, or 'seeing' effects. Consequently, all contributions to the IRIS PSFs are due to systematic effects within the observatory *e.g.*, diffraction from the instrument aperture, surface irregularities of the optics (roughness, scratches, dust, figuring error), charge diffusion in the CCDs, and instrument pointing drift and jitter. We infer PSFs along the spatial dimension of the IRIS SG from on orbit observations. Instrumental blurring can then be significantly reduced or removed by deconvolving the inferred PSFs from IRIS SG data.

Solar occultations due to planetary transits or solar eclipses provide a sharply defined shadow that can often be used to characterize the PSF of a Sun-pointed instrument. Weber et al. [2007] and Wedemeyer-Böhm [2008] fit PSFs to Mercury transit data observed by the *X-ray telescope (XRT)*, *Broadband Filter Imager (BFI)* and the *Solar Optical Telescope (SOT)* onboard the *Hinode* spacecraft. DeForest et al. [2009] constrained semi-empirical PSFs and measured the effect of stray light in the *Transition Region And Coronal Explorer (TRACE)* extreme-ultraviolet (EUV) telescope using Venus transit observations. More recently, Poduval et al. [2013] characterized the diffuse component of the PSFs for the *Atmospheric Imaging Assembly (AIA)* EUV telescopes on board the *Solar Dynamics Observatory (SDO)* spacecraft using a lunar occultation of the Sun.

We use the May 2016 Mercury transit to characterize on orbit PSFs for the IRIS SG. While Mercury's limb (when occulting the Sun) provides a sharply defined edge from which a spatial component of the SG PSF may be derived, the region in Mercury's shadow is devoid of any significant spectral information. Therefore, we confine our attention to blurring in the spatial direction only (parallel to the SG slit) and assume that the PSF is effectively invariant across the passband in each SG channel. The structure of the paper is as follows: In Section 3.2 we describe IRIS, the data, and processing required for our analysis. Section 3.3 describes model PSFs for the far ultraviolet (FUV) and near ultraviolet (NUV) SG channels, and the semi-blind deconvolution process we use to derive NUV PSF estimates. In Section 3.4 we present these estimates and discuss their applications with representative deconvolved data. We conclude by summarizing the characteristics of our PSF estimates and present deconvolved spectra in Section 3.5.

The PSFs determined here are distributed via SolarSoft [SSW, Freeland and Handy, 1998] with a deconvolution routine, `iris_sg_deconvolve.pro`, suitable for direct application to IRIS SG Level 2 data.

3.2 Instrument and Data Selection

The IRIS instrument uses a Czerny–Turner style spectrograph and a slit-jaw imager (SJI) to obtain solar images and spectral information over a range of ultraviolet (UV) wavelengths. The SG and SJI instruments are fed by a single 19 cm Cassegrain telescope [Podgorski et al., 2012]. A slit prism at the focus of the telescope separates incoming light into three light paths: SG FUV (short, 1332 – 1358 Å, and long, 1389 – 1407 Å, channels), SG NUV (2783 – 2835 Å channel), and SJI channel. Spectra and images are obtained by four 2061 × 1056 pixel CCDs. The field of view (FOV) of the SG slit is $0.33'' \times 175''$. SG rasters are created by scanning the active secondary mirror of the Cassegrain telescope, for a maximum raster FOV of $130'' \times 175''$. Each 13 µm pixel of the SG CCDs subtends $0.167''$ spatially and 12.8 mÅ (FUV) or 25.5 mÅ (NUV) spectrally.

Level 2 IRIS data are available for download from the Lockheed Martin Solar and Astrophysics Laboratory (LMSAL: `https://iris.lmsal.com/data.html`) and are considered the standard science product. The Level 2 data are 32-bit floating point numbers. Processing IRIS data to Level 2 includes removing overscan rows, reorienting images to common axes, removing dark currents and pedestal, flat fielding, applying geometric and wavelength calibrations, mapping images to a common plate scale, subtracting FUV background, and recasting images into rasters (SG) and time series (SJI) [De Pontieu et al., 2014]. The level 2 SG data may further be subdivided into spectral regions, or "windows," corresponding to a spectral line list that reads out only a portion of the CCDs at the time of observation. The spectral regions are denoted by the emission or photospheric reference line wavelength they encompass [*e.g.* 1336, 1394, 1403, 2796 and 2814 Å; De Pontieu et al., 2014]. IRIS observed the Mercury transit using a full readout for 15 s exposures and a small linelist otherwise (see *e.g.* Table 3.1).

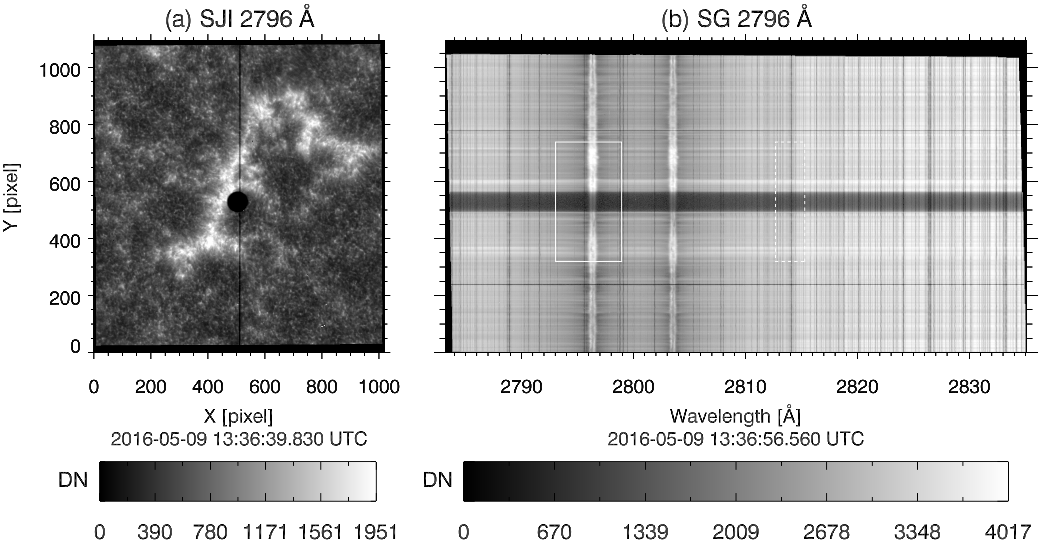

Figure 3.1: Panel (**a**), IRIS 2796 Å slit-jaw image of Mercury transit. Mercury is the dark shadow near center, the *dark vertical line* through the center of the image is the spectrograph slit. Panel (**b**), corresponding full NUV spectrograph readout. Mercury's shadow is the dark horizontal band across spatial pixels ≈490 to 570. *Thin horizontal dark lines* near spatial pixels 240 and 775 are fiducial marks on the slit. Solid white box outlines data analyzed for the 2796 Å window; *dashed box* is the same for 2814 Å window. The vertical extent of both boxes is sized to exclude the fiducials.

On 09 May 2016, as seen from Earth, Mercury transited across the solar disc from ≈10:50-19:00 UTC, moving from east to west. IRIS imaged the entire transit in ≈50 minute increments, the length of time required for Mercury to travel across the SJI FOV. Approximately 10 minutes of observing time was missed between each increment, while the spacecraft changed pointing to keep Mercury in the SJI field of view. The SG slit was oriented parallel to the solar north–south axis for the duration of the transit, so that Mercury crossed the slit at least once during each pointing. Figure 3.1 panel (a) shows a typical 2796 Å SJI image during the transit. The SG slit is visible as a dark vertical line, passing through the shadow of Mercury near center of Figure 3.1 (a).

Table 3.1: IRIS Mercury transit observations.

Data Set	Obs. Period	Exposure		Max. Occultation		Notes
	UTC	*# of exps.*	*len. (s)*	*Index*	*UTC*	
1	10:50:08–11:34:59	514	4	287	11:15:14	Sit & stare, SL
2	11:44:39–12:23:44	448	4	226	12:04:24	Sit & stare, Rot. track, SL
3	12:33:44–13:06:00	600	2	380	12:54:12	Sit & stare, Rot. track, SL
4	13:16:31–13:54:53	140	15	74	13:36:57	Sit & stare, Rot. track, FR
5	14:04:46–14:48:34	502	4	293	14:30:23	Sit & stare, Rot. track, SL
6	14:59:55–15:26:08	96	15	62	15:17:02	Raster, FR
7	15:36:23–16:20:57	512	4	264	15:59:24	Sit & stare, Rot. track, SL
8	16:31:03–17:10:31	144	15	72	16:50:55	Sit & stare, Rot. track, FR
9a	17:25:48–18:00:41	400	4	0	17:25:48	Raster, SL, †
9b				1	17:25:53	
9c				2	17:25:58	
9d				4	17:26:09	
9e				6	17:26:19	
9f				8	17:26:30	
10	18:10:41–19:00:57	576	4	337	18:40:09	Sit & stare, W1

SL: Small line list: 1336 (C II) and 1403 (Si IV), NUV: 2796 (Mg II k), and 2814 Å.
FR: Full readout. To maintain consistency between data sets, we analyze only the portions of the NUV spectra that overlap with the windows listed in SL from the full readouts.
† Raster motion closely matched that of Mercury at the start of data set 9, therefore maximum occultation was imaged multiple times in this data set.

From the 10 sets of observations IRIS made during the transit, only a handful of spectra were suitable for estimating the SG PSF. Spectra were selected in which the signal-to-background ratio (SBR) was large enough so that both limbs on either side of Mercury were sharp and well defined. The observing period, exposure length, location of maximum occultation, and observing notes are listed in Table 3.1 for each of the 10 SG data sets. To minimize the contribution of Mercury's motion to the PSF, we selected only the spectra from each data set where the occultation by Mercury's shadow was maximized over the slit. Except for data set 9, Mercury crossed the SG slit once in each data set. In data set 9, the raster motion tracked Mercury for several frames at the beginning of the observation, resulting in six occurrences of maximum occultation.

The selection criteria were met by data sets 2 through 9 in the NUV channel. Data sets 1 and 10 were ignored because the shadow of Mercury was partially off the solar disc when imaged by the SG. For the off-disc portion of Mercury, SBR is insufficient to present a well-defined limb in the NUV spectra. Figure 3.1 panel (b) shows the full readout NUV CCD spectrum from data set 4; residual intensity from the instrument PSF is clearly seen where Mercury's shadow crosses the Mg II doublet. From the full NUV readouts (data sets 4, 6, and 8), we select only the spectral regions that correspond to the 2814 Å and 2796 Å windows (see Section 3.2.1) to maintain consistency across all data sets. Of the NUV windows, 14 suitable spectra were obtained for both the 2814 Å and the 2796 Å windows.

For the FUV windows (1403, 1394, and 1336 Å), only the three 15 s exposures (data sets 4, 6, and 8) from the 1394 Å and 1336 Å windows had sufficient SBR to present well-defined limbs of the shadow of Mercury. Fewer data sets in FUV spectra meet the selection criteria because quiet Sun and active region intensity in the FUV [*i.e.*, C II, Si IV, and O IV, Vernazza and Reeves, 1978, Cook et al., 1995] is weaker than that of the NUV [Mg II and NUV continuum, Morrill and Korendyke, 2008, Staath and Lemaire, 1995]. For this reason, and because SG throughput decreases with wavelength [De Pontieu et al., 2014], SBR is sufficient only in the data sets with the longest (15 s) integration times. We also note that in two of the three FUV data sets, the north limb of Mercury is over a region of bright plage (see, *e.g.*, Figure 3.3). This results in significantly greater contrast at the north limb compared to the south limb.

We modify the NUV and FUV spectra selected above for input to our semi-blind deconvolution routine. Preparation of the data differs slightly between the NUV and FUV cases, largely due to the lower SBR of the FUV data. In the following subsections we first describe reduction of the NUV spectra, then we describe the differences in this process for the FUV spectra.

3.2.1 NUV Data Reduction

IRIS SG images contain fiducial markings to aid in the geometric alignment of the spectra. These markings are gaps in the slit, and appear as two dark horizontal bands in the spectra (see, *e.g.*, Figure 3.1 panel (b) near spatial Y pixels 240 and 775). Since the slit prism is placed after the telescope optics, the images of the fiducial markings formed on the SG CCDs are not affected by aberrations inherent to the telescope. The PSF in the region of the fiducial markings is therefore narrower. To prevent biasing the PSF estimate, we cropped the fiducial markings from each transit spectrum. A buffer region of several pixels adjacent to each fiducial is removed, the size of which varies so that the shadow of Mercury is centered in the image frame.

We reduce the data to 1D by spectrally summing the transit images. There are two advantages to performing this sum; (1) our task is reduced to finding a PSF in one dimension instead of two, and (2) the signal-to-noise ratio (SNR) is improved for the summed data set. In the NUV the presence of continuum in the spectrum contributes to the overall signal level, so we include the entire window in the sum.

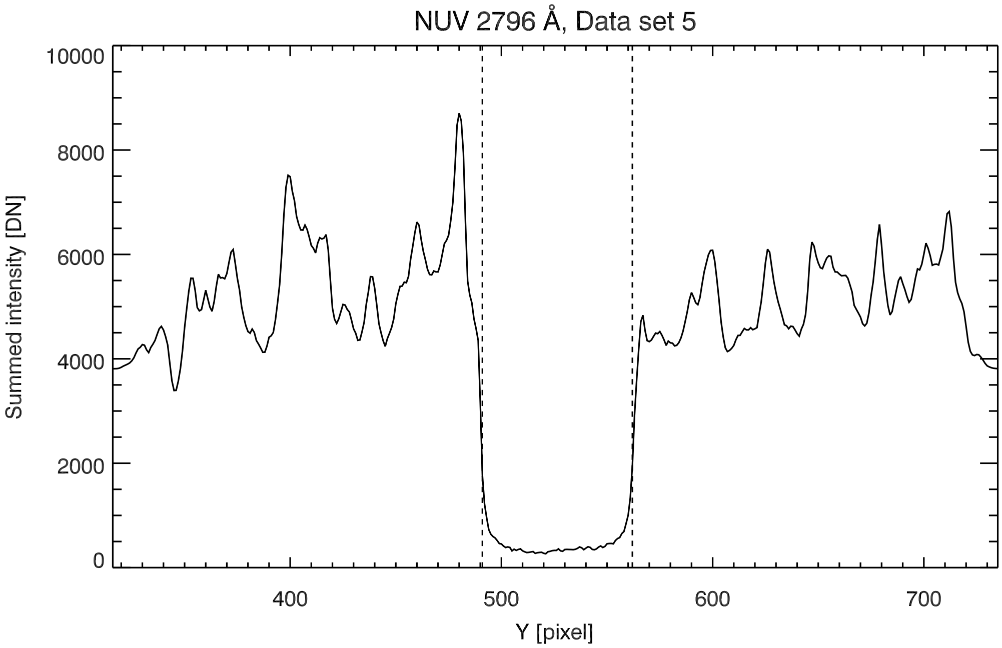

Figure 3.2: Reduced data from set 5. *Vertical dashed lines* mark Mercury limbs. Data are summed over the 232 spectral pixels in this 2796 Å window, the horizontal extent of the solid white box in Figure 3.1 panel (b). Fiducial markings are removed by cropping data.

Data analyzed in the NUV windows is outlined by dashed (2814 Å) and solid (2796 Å) boxes in Figure 3.1 spanning 103 and 232 spectral pixels, respectively. There are two underlying assumptions in our choice to sum over wavelength. The range of reflection angles across the spectral window is small, so we assume that any variation in the PSF with respect to wavelength over the range of a spectral window is small enough to be ignored. This assumption is supported by the nearly identical PSFs in each of the two FUV and NUV windows, estimated independently by our Fourier model in Section 3.3 and our results in Section 3.4. The second assumption is that dispersion is oriented precisely along the pixel rows (*i.e.* the x-axis, or dispersion axis, of the spectra). This applies only to IRIS Level 1.5 data and higher, in which the small instrumental misalignment of the spectrum to the SG CCDs has been corrected for

[De Pontieu et al., 2014]. We have also verified by hand that the fiducial markings are aligned precisely row-wise within each spectral window.

As part of the Level 1.5 processing, the IRIS spectra are warped by a second order polynomial so that the spatial and spectral dimensions are rectilinear with respect to the CCD pixel grid [Jaeggli, 2016]. The geometric correction varies in time and space. A side effect of the image warping (*i.e.* geometric correction) is that sub-pixel shifts result in varying attenuation of high spatial frequencies. Since the correction is small, the offset from the original to the corrected grid of pixels varies slowly across the CCD. For the worst case of a half-pixel shift, the Nyquist frequency is completely lost. In the spatial dimension, the result is a periodic blurring. The phase of this periodic blurring varies image-to-image due to temporal alignment variations in the instrument. By summing along the spectral axis, we have averaged the best and worse cases of this blurring in each image.

3.2.1.1 Estimation of Mercury's limb The reduced version of the solid white box in Figure 3.1 panel (b) is plotted in Figure 3.2; the vertical dashed lines mark the locations of Mercury's limbs. The limbs are located by finding the spatial locations of maximum and minimum derivatives of the reduced spectra intensity in a region that encompasses the entire shadow of Mercury. The derivative is computed using centered differencing,

$$\left.\frac{dI}{dy}\right|_{y=y_i} = \frac{I(y_{i+1}) - I(y_{i-1})}{y_{i+1} - y_{i-1}}\,, \tag{3.1}$$

where $I(y)$ is the summed intensity at pixel y in the reduced data. Errors in limb location of at least ± 1 pixel are expected from discretization; noise in the data may increase this uncertainty. Only approximate locations of the limbs are needed to constrain the semi-blind deconvolution described in Section 3.3.2. Except data sets 5 and 7, we find the locations of the limbs to be consistent between the two NUV windows using this method. For these two data sets, the north limb is displaced one pixel northward in the 2796 Å window when compared to the 2814 Å window. From the limb locations we find that Mercury's shadow spans 72–73 pixels, or an angular diameter of 12–12.2″. For comparison, the angular diameter of Mercury, when viewed from Earth, was estimated to subtend 12.1″ during the time of the transit[U.S. G.P.O., 2015].

3.2.2 FUV Data Reduction

The FUV data reduction proceeds in a similar fashion as the NUV, but with notable modifications described below.

The continuum signal is absent in the FUV. The pixels between the bright emission lines contain only background and readout noise. We therefore sum over only the bright FUV spectral pixels outlined by the dashed boxes in Figure 3.3 panels (b) and (c).

Contrast is insufficient to locate the limb using the derivative method. We select the limb locations of the 2814 Å window as the reference for the FUV data sets. Using the co-alignment performed between spectral windows during Level 2 processing, the limb locations are transferred to the FUV windows.

We find the mean intensity in Mercury's shadow is negative in several of the data sets. This could be a result of small errors in the dark subtraction, which are amplified by spectral summing. To correct this, we estimate the offset error by computing the mean per-pixel intensity in no-signal regions of Mercury's shadow in the FUV data sets. These regions are outlined by solid black boxes in (b) and (c) of Figure 3.3. We find offset error values that range from −0.03 to 0.06 DN (1394 Å) and −0.04 to −0.18 DN (1336 Å). We correct these intensity errors by adding a DC offset to the FUV data sets. The value of the DC offset is such that the mean per-pixel intensity

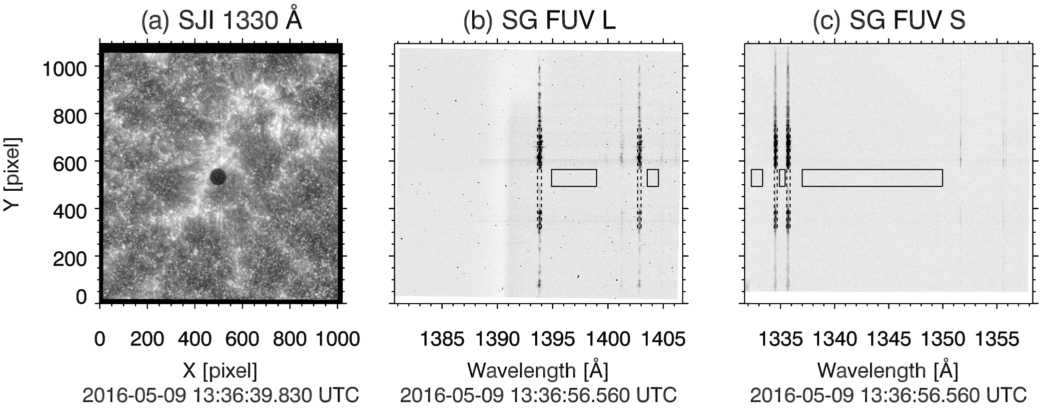

Figure 3.3: (**a**) 1330 Å SJI context image of Mercury transit. (**b**) and (**c**), full readout of data set 4 in the two FUV channels 1394 Å and 1336 Å windows, respectively. Only the spectral lines enclosed by the *black dotted boxes* are analyzed to maximize SBR. Dark subtraction error is estimated by no-signal pixels in Mercury's shadow, enclosed by the *black solid boxes*. Intensity is logarithmically scaled in all panels; SG images are displayed in inverse gray scale.

in the regions outlined in Figure 3.3 (b) and (c) is zeroed.

3.3 PSF Estimation

We estimate the IRIS SFG PSFs using a modified blind iterative deconvolution (BID) technique, in contrast to the parameterized and semi-empirical methods referenced in Section 3.1. BID typically refers to a technique first developed by Ayers and Dainty [1988]; however, it can refer to any image restoration technique in which both the un-degraded image and its degrading function (typically the PSF) are unknown. BID techniques are most often used when *a priori* knowledge is limited to only non-negativity of the images. For example, the Ayers and Dainty [1988] method was subsequently used to derive PSFs and deconvolve images from *Skylab* and *Yohkoh* data [Karovska et al., 1994], and to estimate the on orbit PSF for the TRACE instrument [Golub et al., 1999].

Determining PSFs using BID techniques presents an ill-posed problem. Parameterizing the PSF may be considered a more robust approach [DeForest et al., 2009]; however, the BID method can be improved by incorporating *a priori* information [Fish et al., 1995] resulting in the 'semi-blind' description of the modified BID technique. We find that the IRIS Mercury transit data lends itself well to this particular type of analysis. In much of our data, solar features immediately behind Mercury's limb are not uniformly illuminated (see, *e.g.*, either side of Mercury's shadow in Figure 3.2). As a result, the data are not well approximated by a step function precluding a similar analysis such as performed by Weber et al. [2007] and Wedemeyer-Böhm [2008]. DeForest et al. [2009] and Poduval et al. [2013] used scattered light in the interior shadows of occultations by Venus and the Moon to semi-empirically constrain stray light PSFs for the TRACE and the AIA assembly aboard SDO. This form of analysis is largely concerned with scattering wings so that detailed information on the core structure of the PSFs is excluded. Since we have no *a priori* knowledge of the IRIS PSF, we find BID is better suited to our purposes since we can estimate the entire PSF from the same data set. Knowledge of the core structure of the PSF allows us to investigate the resolution of the SG (Section 3.4) and ultimately may influence the fine structure that we observe in the IRIS data.

A further advantage of a BID approach is that our PSF model is not constrained by a small number of parameters. IRIS operates close to the diffraction limit so that the core of the SG PSF may show significant structure, such as side lobes or asymmetry (see, *e.g.*, Figures 3.4 and 3.7). The parameterized models referenced earlier cannot reproduce either of these structures, so by using BID we are free to find features that we may not have guessed in advance. This allows us to derive a PSF that is consistent with the data at hand.

For the above reasons, we feel that a BID method of estimating the IRIS PSFs is advantageous over a parameterized model. We base our BID on the Richardson–Lucy algorithm (see Equation 3.3), as this method has proven robust in the presence of noise [Fish et al., 1995]. In the remainder of this section we describe initialization (and how we include *a priori* information), the iterative routine, and stopping criterion for our semi-blind deconvolution method.

3.3.1 Initial Guesses

Before we begin the process of deconvolution to determine the PSF, we must prepare initial guesses both for the ideal deconvolved data and for the PSF. In both cases, we will make use of prior information. For that reason, we describe the deconvolution as *semi*-blind.

3.3.1.1 Mercury's Shadow

Since Mercury is opaque, Mercury's shadow during the solar transit will contain no UV radiation. Ideally, the limb of Mercury should have a 'hard' edge in the SG spectra, where the signal drops abruptly to zero in the shadow region. In the observed spectra, the SG PSF softens this edge and causes residual intensity to appear in the shadow of Mercury (see, *e.g.*, Figures 3.1, 3.2, and 3.5), indicating some level of scattered light is present in all spectral windows.

As an initial guess for the NUV deconvolved scene, we modify the reduced data set by setting all pixels to zero between limb locations. The two pixels at the limbs are not set to zero, to allow for subpixel location of the limb. Since the semi-blind deconvolution is a multiplicative process of the initial guess (see, *e.g.*, Equation 3.2 and 3.3), any pixel that is initially set to zero will remain unchanged after each iteration. This initial guess therefore enforces the prior knowledge that the scene should contain no light in the shadow of Mercury.

In the FUV, low SNR results in some negative intensity values. Convergence of the Richardson–Lucy algorithm is neither desirable nor possible in this case [Lucy, 1974]. To counter this, we add a positive DC offset to the FUV reduced data. The pixels in Mercury's shadow are then forced to the value of the DC offset after each iteration, rather than zero as in the NUV case discussed above. The magnitude of the offset is arbitrary; it only needs to be large enough so that negative noise pixels are not 'clipped' at zero. We choose a value of 10^3 DN, which is ample margin to prevent clipping. The offset is subtracted after deconvolution to yield an unbiased estimate of the deconvolved scene.

3.3.1.2 Model PSFs Using the theory of Fraunhofer diffraction [*e.g.* Goodman, 2005, pg. 74, or similar references], we calculate the diffraction pattern of the Cassegrain telescope aperture at the emission line wavelength for each of the four spectral windows. We reduce this 2D pattern to a 1D spatial PSF by summing along the axis parallel to the dispersion direction of the instrument. Spatial PSFs for the NUV and FUV windows are plotted in Figure 3.4. The diffraction caused by Mercury's limb has also been considered; appendix B demonstrates that this diffraction pattern does not affect the PSFs estimated herein. The log plots of Figure 3.4 clearly show side lobes in the wings of the model PSFs. The side lobes are a result of the fringes of the diffraction pattern from the telescope entrance aperture, including central obscuration and spiders. For the remainder of this report, we define the core of the PSF as the radius extending to five pixels on either side of the individual PSF peak value. The output of the semi-blind deconvolution depends on the initial PSF choice, and in Section 3.4 we consider an alternate initialization.

Deconvolving the model PSFs from the reduced data gives an indication of the SG performance compared to the diffraction-limited case. In Figure 3.5, model PSFs are deconvolved from the reduced data and overplotted (solid curves) on the reduced data (dashed curves). The iterative Richardson–Lucy algorithm is used to perform

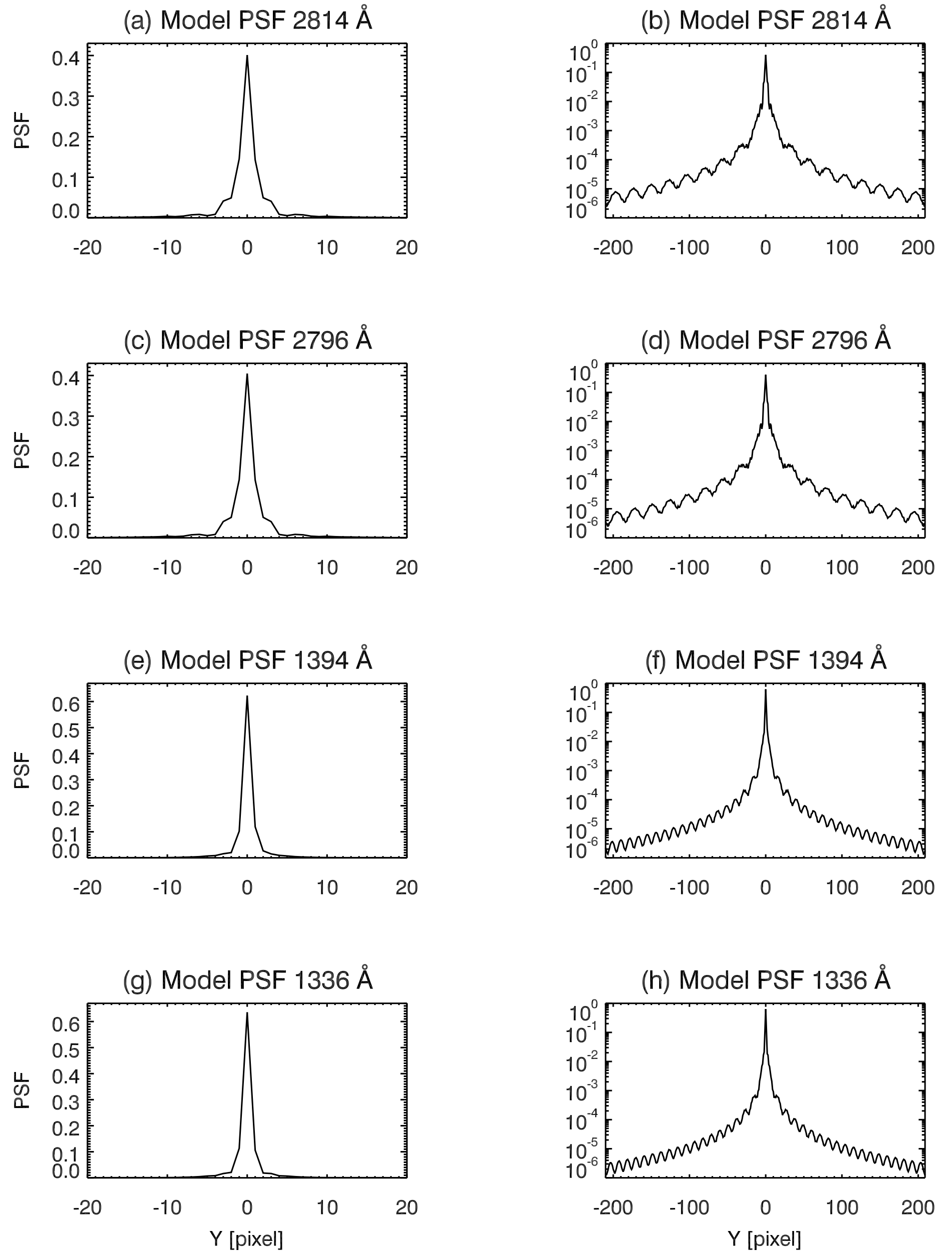

Figure 3.4: Diffraction limit model PSFs for the IRIS Cassegrain telescope. Top panels show the core (**a**) and wings (**b**, log scale plot) of the NUV 2814 Å PSF. Remaining panels depict the same for the (**c, d**) NUV 2796 Å , (**e, f**) FUV 1394 Å , and (**g, h**) 1336 Å windows.

the deconvolution. This method of deconvolution corrects large deviations from the true scene in relatively few iterations; further iterations result in small corrections

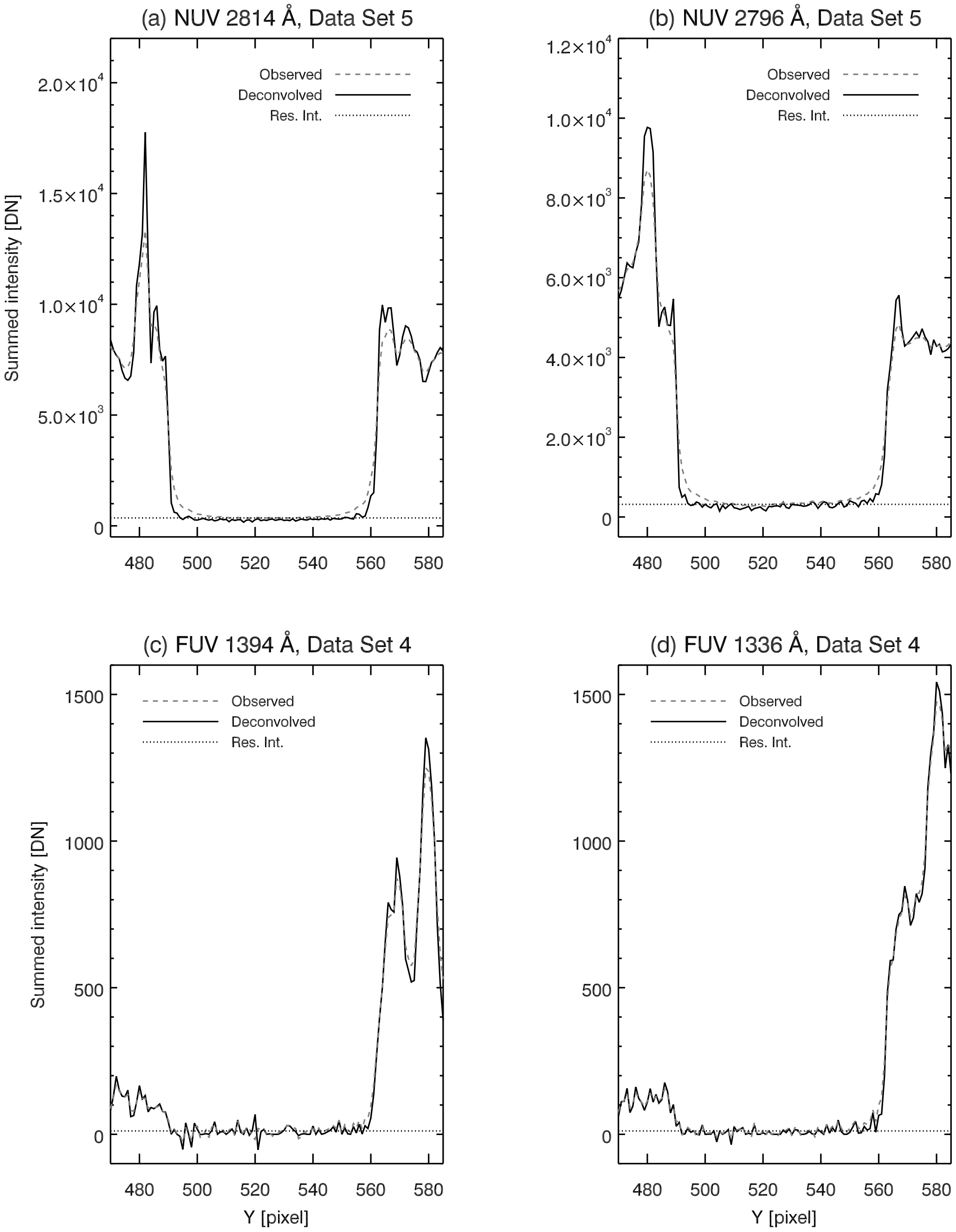

Figure 3.5: Model PSFs deconvolved from reduced data (*solid curves*), with original overplotted (*dashed curves*). Panel (**a**) shows NUV 2814 Å window, (**b**) NUV 2796 Å (**c**) FUV 1394 Å, and (**d**) FUV 1336 Å. Mean residual intensity in Mercury's shadow after deconvolution is plotted as the *dotted curve* in each panel.

that slowly tend to match the statistical fluctuations in the observed scene [*i.e.*, noise, *e.g.* Lucy, 1974]. For this reason, a cost function is typically used to truncate iterations. Often this takes the form of a χ^2 goodness of fit between the observed scene and a forward model consisting of the deconvolved scene re-convolved with the PSF. For our purposes, we use a modified form of the Kullback–Leibler (KL) divergence [Bertero et al., 2009] as the cost function, so that negative pixels may be handled in the same way as Section 3.3.1.1. To prevent fitting to noise, we truncate iterations when the derivative of the KL divergence is ≈ zero. Experimentally, we find 50 iterations in NUV and 9–10 iterations in FUV windows are sufficient to meet this criterion.

In the NUV channel, the effect of deconvolution is evident in panels (a) and (b) of Figure 3.5. Residual intensity is clearly greater than zero in these panels, indicating not enough energy is present in the wings of the NUV model PSFs. The core of the NUV model PSFs also needs correction, as prominent 'shoulders' are still evident at Mercury's limb after deconvolution. In panels (c) and (d) of Figure 3.5, deconvolution of the diffraction-limited PSF results in little change for the two FUV spectra. Some sharpening of the north limb is evident (*e.g.* near pixel 560 in panels (c) and (d) in Figure 3.5); however, residual intensity (dotted line, refer to Section 3.3.2) remains slightly greater than zero in the shadow of Mercury. Mercury's limb is sharpened, and scattered light is reduced in both SG channels by deconvolving the model PSFs; however, Figure 3.5 clearly shows that the model PSFs are inadequate at describing the SG performance in the NUV channel. The effectiveness of the FUV model PSFs are more difficult to discern due to lower SBR in this channel.

3.3.2 Semi-blind Deconvolution

PSFs were estimated using an iterative blind deconvolution routine to simultaneously estimate the PSF and the deconvolved image. We consider our implementation to be a semi-blind method, since *a priori* knowledge of both the diffraction-limited form of the instrument PSF and the complete opacity of Mercury are incorporated into the first iteration of the routine by the initial guesses described previously. The deconvolution routine consists of alternating applications of Richardson–Lucy deconvolutions [Richardson, 1972, Lucy, 1974], expressed as

$$g^{i+1}(y) = \left[\left(\frac{c'(y)}{g^i(y) * f^i(y)}\right) * f^i(-y)\right] \cdot g^i(y)\,, \tag{3.2}$$

$$f^{i+1}(y) = \left[\left(\frac{c'(y)}{f^i(y) * g^{i+1}(y)}\right) * g^{i+1}(-y)\right] \cdot f^i(y)\,, \tag{3.3}$$

where $g(y)$ is the PSF, $f(y)$ is the deconvolved image, $c'(y)$ is the original (detrended) degraded image, y is spatial position in IRIS pixels, i is iteration number, and $*$ is the convolution operator [Fish et al., 1995]. One iteration consists of one evaluation of Equation 3.2 to find the next PSF estimate, $g^{i+1}(y)$, followed by one evaluation of Equation 3.3 to find the next deconvolved image, $f^{i+1}(y)$ [Holmes, 1992]. Integration of Equation 3.3 shows that the total flux is conserved. Conservation of flux is enforced in Equation 3.2 by re-normalizing $g^i(y)$ after each iteration. Iterations are started with the guesses from Section 3.3.1.1 and Section 3.3.1.2 for $f^0(y)$ and $g^0(y)$, respectively.

The convolution operations in Equations 3.2 and 3.3 are performed in Fourier space for computational efficiency. To reduce contamination from edge effects, we detrend the reduced data. For the left edge of $c(y)$, we write this as

$$c'(y) = \begin{cases} \mu \cos^2\left[\frac{\pi y}{2a}\right] + c(y)\sin^2\left[\frac{\pi y}{2a}\right] \,, & 0 \le y \le a \\ c(y)\,, & y > a \end{cases} \,, \tag{3.4}$$

where μ is the mean of the two endpoints of $c(y)$ and a is the number of pixels the smoothing extends from the edge of the data. A similar treatment is applied to the right edge (see, *e.g.*, Figure 3.2). We set $a = 30$, the geometric mean of the PSF half width (five pixels) and the length of data from the left edge to Mercury's limb (≈ 175 pixels). To prevent a symmetric bias in the data, we pad $c'(y)$ to twice its original length with the value of μ and zero pad $g^i(y)$ to match.

3.3.3 Stopping Criterion

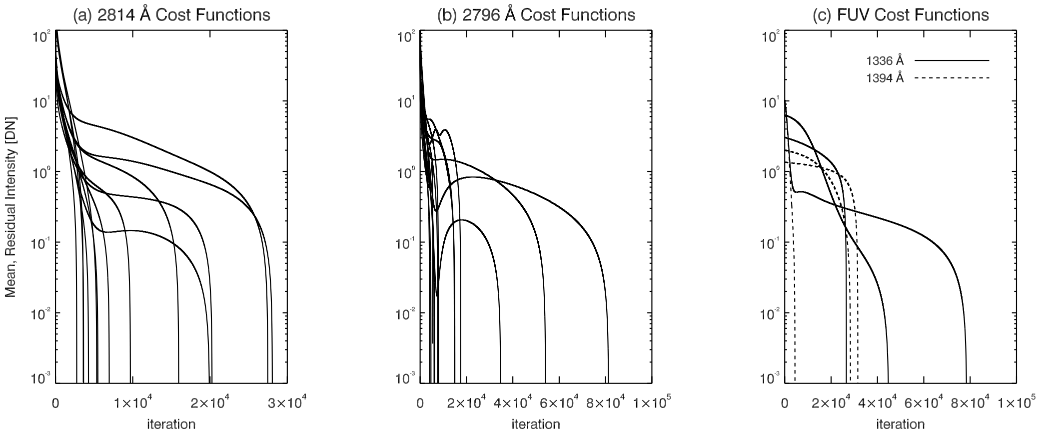

Figure 3.6: Log plot of cost functions for the (**a**) NUV 2814 Å, (**b**) NUV 2796 Å, and (**c**) FUV 1336 (*solid*) and 1394 Å (*dashed*) windows. The cost function is a measure of residual intensity in Mercury's shadow. Iterations are truncated when the cost function reaches zero.

Since the Richardson–Lucy process is an iterative approximation to deconvolution [Lucy, 1974], iterations are truncated when a stopping criterion is met. The stopping criterion is typically derived from a cost function that quantifies the difference between the observed data and a forward model formed from the deconvolved function and the PSF. This function may take different forms depending on the application [*e.g.*, Richichi, 1989, Fish et al., 1995, Bertero et al., 2009, and the references therein]. For our cost function we choose the mean value of residual intensity in the shadow of Mercury, since *a priori* it is known that this value is zero in the ideal case. We write this function as

$$\mathcal{C}^i = \frac{1}{[N-n+1]} \sum_{k=n}^{N} \mathcal{F}^{-1} \left[\frac{\mathcal{F}[c(y_k)]}{\mathcal{F}[g^i(y_k)]} \right] , \tag{3.5}$$

where $\mathcal{F}$ ($\mathcal{F}^{-1}$) is the (inverse) Fourier transform, $c(y_k)$ is the original degraded data, and k runs only over those pixels between the south (n) and north (N) limbs of Mercury's shadow. The deconvolution is performed as division in Fourier space, so that non-negativity is not inherently enforced. This results in an unbiased estimate of the mean shadow intensity. Iteration of the semi-blind deconvolution is truncated when $\mathcal{C}^i < 0$ so that the previous PSF, $g^{i-1}(y_k)$, is the best estimate that does not over-deconvolve the data. In Figure 3.6 we plot cost functions for all data sets. In every case the cost function reaches a zero-crossing, so that the moment of convergence is well defined.

3.4 Results and Discussion

Figure 3.7 displays normalized PSFs for the selected data sets (light gray curves in plots) of the NUV and FUV spectral windows. In each panel of Figure 3.7, the black curve is the mean of PSFs in that spectral window. We take the mean as the best PSF estimate for the two NUV windows, since it preserves normalization while reducing the noise in the wings of the PSFs. We note that the two NUV PSF estimates show similar core (panels (a) and (c), Figure 3.7) and wing structures

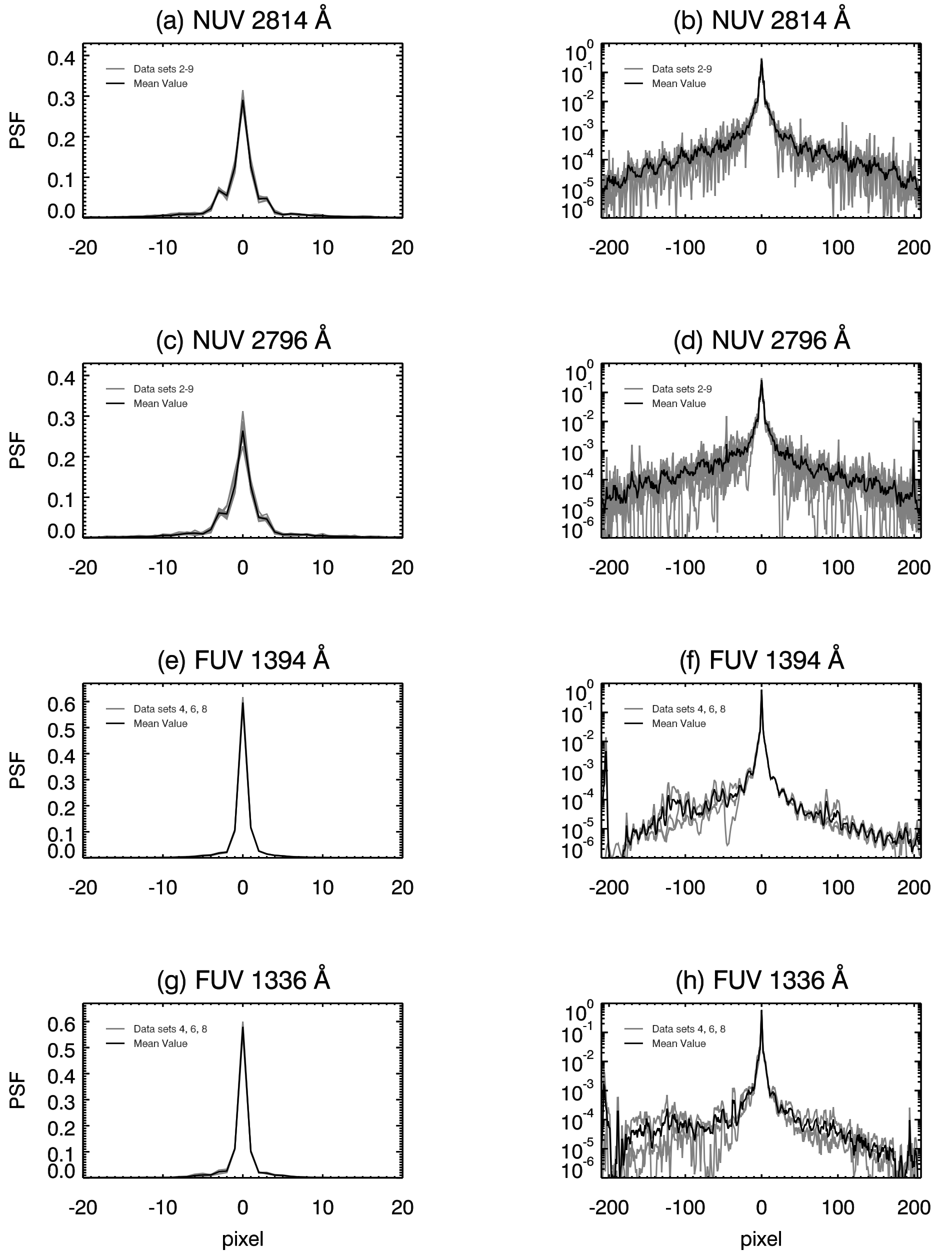

Figure 3.7: PSF estimates from the semi-blind Richardson–Lucy routine for the (**a, b**) 2814 Å, (**c, d**) 2796 Å, (**e, f**) 1394 Å, and (**g, h**) 1336 Å observation windows. *Gray curves* represent the estimate(s) from data sets 2–9 for the NUV and 4, 6, and 8 for the FUV windows. The mean value PSF is overplotted as a *black curve* in each panel. Variation in the left wing of (**f**) and (**h**) results from low contrast in quiet Sun area south of Mercury, see text for details.

(panels (b) and (d), Figure 3.7) despite being derived from different spectral windows. The similarities between the NUV PSF estimates conforms to our expectation that the PSF should not change significantly over a short wavelength range. We assume that any differences between the two NUV PSFs are due to random error.

For the FUV 1394 Å and 1336 Å windows (panels (e) and (g) of Figure 3.7, respectively), the mean PSFs also display similar core structure. In data sets 4 and 6, the southern limb of Mercury is positioned over a region of quiet Sun. Lower solar emission in this region reduces the contrast of this limb in these two data sets. In Figures 3.7 (f) and (h), this manifests as significant variation in the left wing of the FUV PSFs. To remove the uncertainty, we assume the FUV PSF wings are symmetric. We replace the left wing of the mean PSF in both FUV spectral windows (pixels < -5, panels (f) and (h) Figure 3.7) with a mirrored version of its right wing (pixels > 5), then renormalize the result to unity (*e.g.*, (f) and (h) in Figure 3.14).

Comparing (a–d) of Figure 3.7 to the same panels in Figure 3.4, we find that our NUV PSF estimates have more distinct, asymmetric side lobes than the diffraction-limited case. The wings of the NUV PSF estimates are also flatter, which indicates more light is scattered in the NUV channel than the diffraction-limited case. Comparing panels (e–h) of Figure 3.7 and Figure 3.4 we do not find side lobes in the FUV PSF cores; however, wing structure is very similar in both cases.

Table 3.2: PSF energy distribution.

Window	Diff. Model		PSF Estimate		
(Å)	Core	Wings	Core	Wings	PLSR
2814	0.898	0.102	0.815±0.003	0.185	0.725±0.003
2796	0.899	0.101	0.789±0.010	0.211	$0.652^{+0.008}_{-0.010}$
1394	0.954	0.046	$0.951^{+0.003}_{-0.078}$	0.049	$0.975^{+0.025}_{-0.098}$
1336	0.957	0.043	$0.939^{+0.015}_{-0.041}$	0.061	$0.928^{+0.066}_{-0.052}$

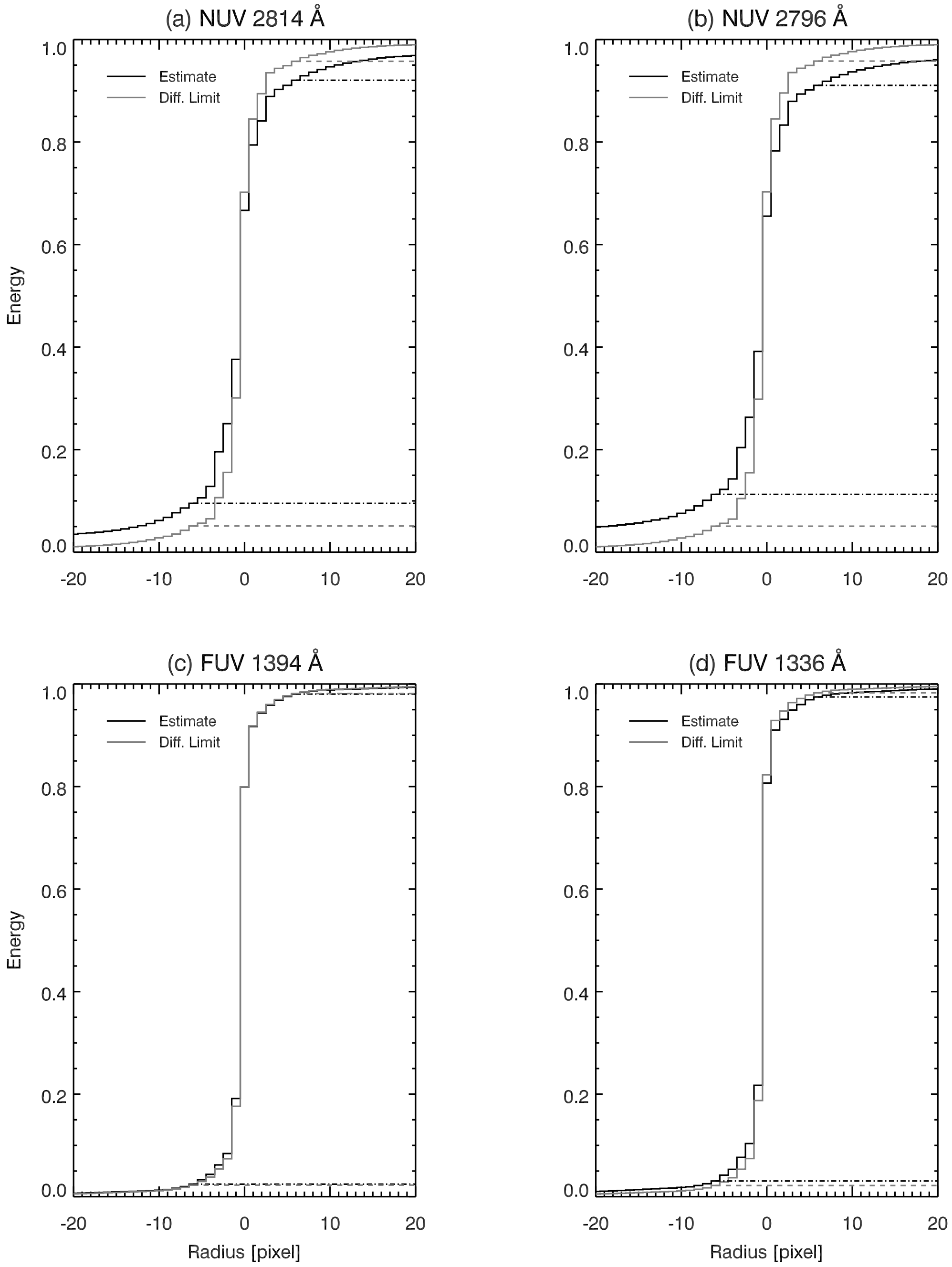

Figure 3.8: Cumulative total energy for the NUV (**a**) 2814 Å, (**b**) 2796 Å, FUV (**c**) 1394 Å, and (**d**) 1336 Å windows. Total energy is calculated between *horizontal line pairs, solid* for diffraction limit PSFs and *dashed* for PSF estimates. NUV plots (**a** and **b**) show similar asymmetric energy distributions.

Table 3.2 lists the wing and core energies for the diffraction limit and PSF estimates. The error ranges reported in Table 3.2 reflect uncertainties in dark subtraction. If the dark signal is overestimated, then after subtraction the signal will be low, and the method will underestimate the core width of the PSF. Low signal also reduces the residual intensity in Mercury's shadow, causing the cost function to truncate iterations early. In general, as the iterations proceed, flux migrates from the PSF core to the tails. Consequently, an overestimate in dark signal results in an underestimate in scattered light. The inverse is true if the dark signal is underestimated. In the NUV channel, dark subtraction uncertainty is $\pm 0.1\,\mathrm{DN}$ per pixel [Wülser et al., 2018]. For the FUV channels, lower SBR means that the offset error must be asymmetrically bounded so that residual intensity in Mercury's shadow is not reduced below zero (clearly an unphysical situation). For an underestimate of dark subtraction, we use the greater of the maximum magnitude of offset error noted in Section 3.2.2 or the per-pixel residual intensity in Mercury's shadow in each FUV channel. There is no bound for overestimating dark subtraction, so we may use the maximum magnitude of offset error from Section 3.2.2.

We estimate total dark subtraction uncertainty as a simple DC offset to the SG spectra. PSFs are recomputed for the extrema of dark subtraction offset to arrive at the uncertainties listed in Table 3.2. The asymmetry in FUV offset error carries through to the listed FUV uncertainty. The last column of Table 3.2 is computed by direct analogy to Strehl ratio. We call this *pixel-limited Strehl ratio* (PLSR), since integration of the peak intensity over the central pixel reduces the peak value of each PSF. Uncertainty in PLSR is estimated in a similar fashion to the core energy. We note that for an underestimate of dark subtraction error, PLSR is reduced and *vice versa* for an overestimate.

As another measure of how energy is distributed between the scattering wings and core, we calculate the cumulative total energy of the NUV PSF estimates. Dash (diffraction-limited) and dash-dot (PSF estimate) horizontal lines demarcate the energy contained in the core of the PSF for each panel in Figure 3.8. Figure 3.8 also shows that the asymmetry of the NUV PSF estimates is similar, and largely constrained to the core of these PSFs.

Table 3.2 and Figure 3.8 show that the PSF estimates have more energy in the wings than the diffraction-limited PSFs in both the NUV and FUV channels. This indicates the instrument scatters more light than the diffraction-limited case. All else being equal, scattered light should be more prevalent at shorter wavelengths. However, our results show that scattering is less prevalent in the FUV than NUV, and scattering is a contributing factor to the reduction in PLSR in the NUV channel. We caution that the FUV transit data are of lesser quantity and quality than the NUV data. In particular, the FUV signal in the shadow of Mercury, which is critical to the estimation of scattered light, is comparatively weak and dominated by noise. Nevertheless, the result holds over the full range of our estimated uncertainties.

To check the plausibility of the PSF estimates, we deconvolve them from the reduced data. By using Fourier deconvolution, we obtain an unbiased estimate of the residual intensity in Mercury's shadow. Since we are using the best estimate (average) PSF on all the individual data sets, this is not merely a recapitulation of the cost function that was used as a stopping criterion in Section 3.3.3. Table 3.3 lists residual intensity in the shadow of Mercury after Fourier deconvolution. For the NUV and both FUV channels, we find that residual intensity after deconvolution is reduced to a fraction of a DN (mean, per pixel) in all but one case. The outlier in NUV data set 4 may result from small dark subtraction errors similar to those noted in Section 3.2.2. Figure 3.9 plots the results of Fourier deconvolution in solid curves for select reduced data sets. For comparison, the observed data is overplotted in dashed

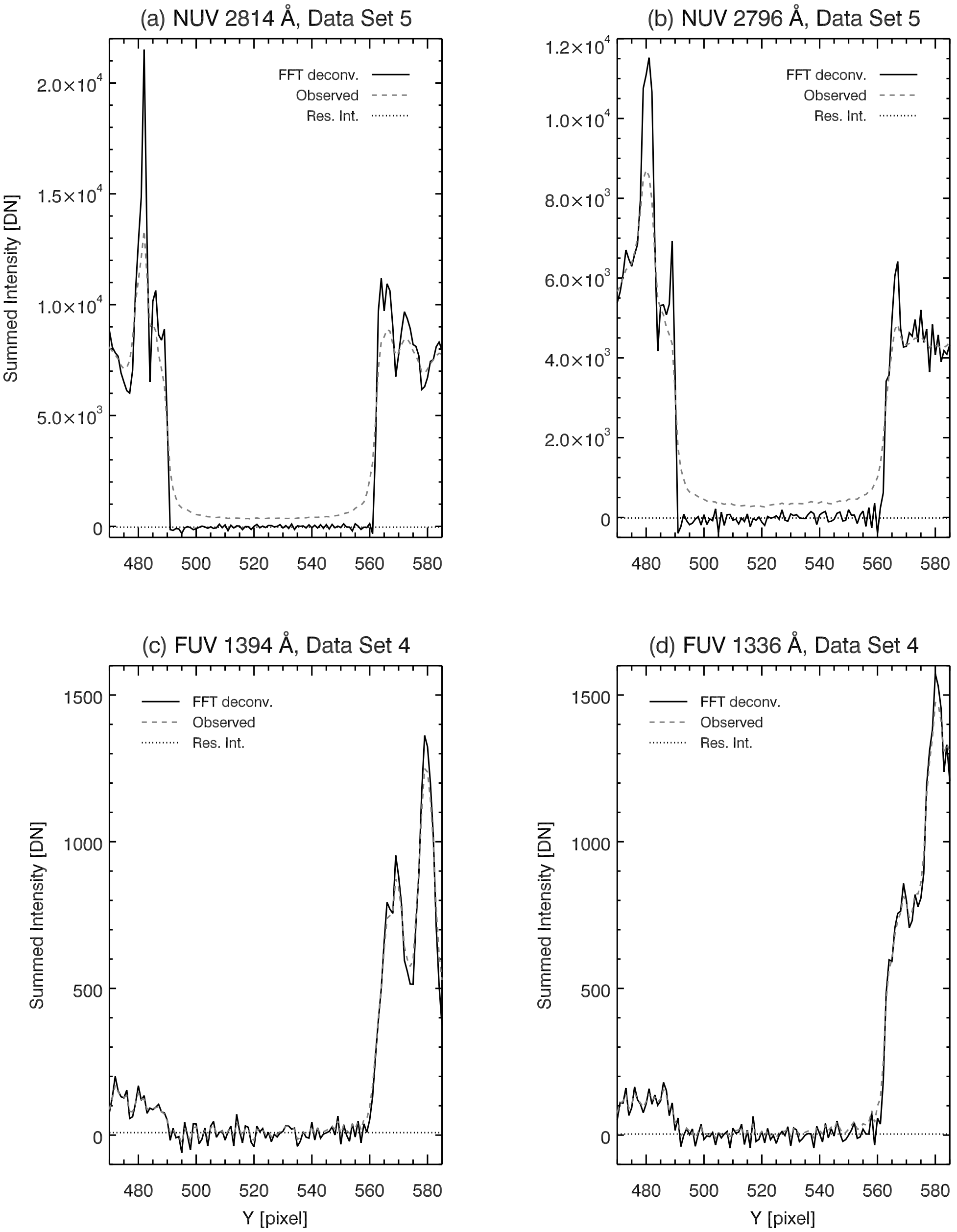

Figure 3.9: Deconvolution of reduced data using PSF estimates. Direct FFT deconvolution is used so that an unbiased estimate is obtained for the mean intensity in Mercury's shadow (*dotted lines*). NUV 2814 Å (**a**) and 2796 Å (**b**) PSF estimates perform well, greatly sharpening the limb of Mercury (compare (a) and (b) in Figure 3.5) and reducing residual intensity to near zero. FUV 1394 Å (**c**) and 1336 Å (**d**) PSF estimates remove more residual intensity when compared to (c) and (d) of Figure 3.5.

Table 3.3: Residual intensity in the shadow of Mercury after PSF deconvolution.

Data Set	1336 Å		1394 Å		2796 Å*		2814 Å*	
	[DN]⋆	*[%]*†	*[DN]*⋆	*[%]*†	*[DN]*⋆	*[%]*†	*[DN]*⋆	*[%]*†
2					0.13	7.9	0.21	5.3
3					0.07	9.0	0.04	1.8
4	0.32	20.1	0.64	49.2	-1.84	-22.1	-1.49	-7.6
5					-0.06	-2.7	-0.37	-6.2
6	0.13	30.2	0.12	48.3	0.73	9.9	-0.65	-3.0
7					0.05	3.1	-0.13	-2.4
8	0.44	58.1	0.22	57.0	0.19	3.0	0.35	2.0
9a					-0.06	-3.6	-0.07	-1.6
9b					-0.05	-2.8	0.03	0.7
9c					-0.01	-0.6	0.04	0.9
9d					0.08	4.5	0.18	4.2
9e					0.05	2.8	0.19	4.3
9f					-0.11	-5.9	0.18	3.9

∗ Negative indicates residual intensity is less than zero after deconvolution.
⋆ DN is the mean per-pixel value in the shadow of Mercury.
† Residual intensity given as percentage of original value before deconvolution.

curves in each panel. The PSF estimates perform well in all data sets compared to the diffraction limit models in Figure 3.5; panels (a)–(d) in Figure 3.9 show that the limbs of Mercury are sharp and steep in the NUV and FUV channels, while residual intensity is reduced to near zero after deconvolution.

The instrument resolution is estimated by the modulation transfer functions (MTFs) in Figure 3.10 panel (a) for NUV and (b) for FUV. In both panels of Figure 3.10 the diffraction-limited MTF is overplotted as a solid black curve. Aliasing (shown by the dashed curves in the figure) causes the MTF to be overestimated by double-counting at the Nyquist frequency. A compensation has been applied to reduce the effect of aliasing on each MTF (solid curves represent aliasing compensated results in Figure 3.10). The aliasing compensation is computed as follows. First a 'non-aliased' diffraction-limited PSF is modeled on a higher resolution grid, so that

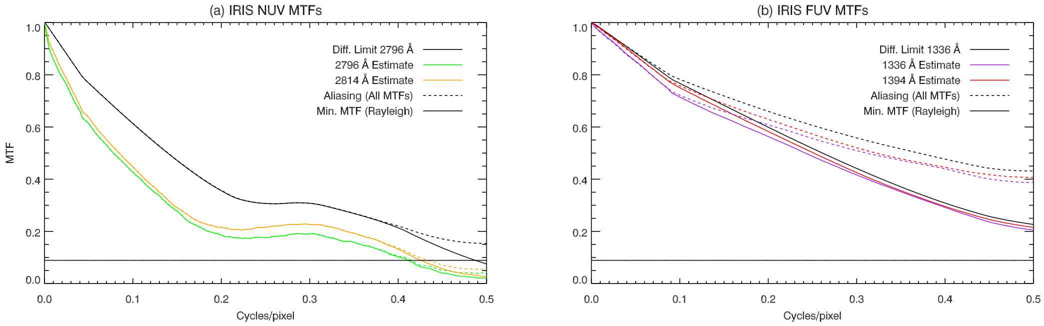

Figure 3.10: MTFs for the SG (**a**) NUV and (**b**) the FUV channels. Diffraction-limited performance (*solid black curve*) and resolution criterion (*dashed black curve*) are overplotted in both panels. A compensation has been applied to all MTFs to reduce the effects of aliasing (see text for details). Aliased curves are plotted in *dashed lines* for all MTFs.

aliasing is negligible at the IRIS SG Nyquist frequency (refer to Section 3.3.1.2). We find that using 1024 pixels is sufficient to suppress aliasing, rather than the 420 pixel length of the reduced data sets. An aliased PSF is then created by applying a boxcar filter the width of an IRIS pixel to the non-aliased PSF. MTFs are then computed from both the aliased and non-aliased PSFs. We define the *compensation curve* as the ratio of the non-aliased to the aliased diffraction-limited MTFs. The compensation curve is re-sampled to match the length of the reduced data set, then multiplied by the MTF estimates for each spectral window. The resulting compensated MTFs are reduced to half the value of the aliased versions at the Nyquist frequency.

We may estimate the spatial resolution of the IRIS SG by analogy to the Rayleigh criterion [Lord Rayleigh F.R.S., 1879]. We choose a resolution criterion of 9%, as this is the value of the MTF of the classic Airy pattern at the resolution attributed to it by Rayleigh. NUV MTFs are plotted in Figure 3.10 (a), showing a significant degradation in MTF, dropping to almost a third of the diffraction limit at the Nyquist frequency. Despite the reduction in resolution, the 2796 Å MTF satisfies the resolution criteria out to 0.41 cycles/pixel (2.47 cycles/arcsec) and the 2814 Å MTF does slightly better at 0.42 cycles/pixel (2.55 cycles/arcsec). Panel (b) of Figure 3.10 shows that the MTFs for both FUV channels are reduced by $\approx 10\%$ compared to the diffraction limit, but still double the resolution criterion at the Nyquist frequency. This shows that the FUV channels are essentially pixel-limited in resolution.

Our PSF estimates include subtle contributions from the blur induced geometric correction, as described in Section 3.3.1. As the geometric blurring varies in time and space, a PSF estimate and deconvolution that accounts in detail for the geometric correction would be prohibitively complicated. This complication could be sidestepped by deriving the PSF for Level 1 data, but that would be of limited value, since geometrical correction is desirable for nearly all scientific use. We have therefore worked from Level 2 IRIS spectra, which are the standard for scientific work. Since our method averages over the geometric blurring, we consider the resulting PSFs as the best average estimates that can be applied to any geometrically corrected IRIS spectra. However, we note that for the same reason, we underestimate the *intrinsic* imaging capabilities of the instrument.

In Figure 3.11, we present the results of deconvolution using our PSF estimates for the NUV 2814 Å (a, b) and 2796 Å (c, d). Figure 3.12 follows the same format for the FUV 1394 Å (a, b) and 1336 Å (c, d) spectral windows. The Mercury spectra from data sets 3 (FUV) and 4 (NUV) are used to illustrate the effect of PSF artifacts in Figures 3.11, 3.12, and 3.13. As the PSFs are one dimensional, deconvolution is performed only along the spatial axis. The deconvolved spectra are calculated by the Richardson–Lucy algorithm, using the same method and criteria described in Section 3.3.1.2. In both NUV spectra, contrast is enhanced throughout the images by deconvolution, evident in the narrower and more peaked spectrum of the deconvolved data in (a) and (b) of Figure 3.13. The limbs of Mercury are also sharpened to a steep cutoff (panels (a) and (b) in Figure 3.13). Scattered light, the ‘haze’ in the

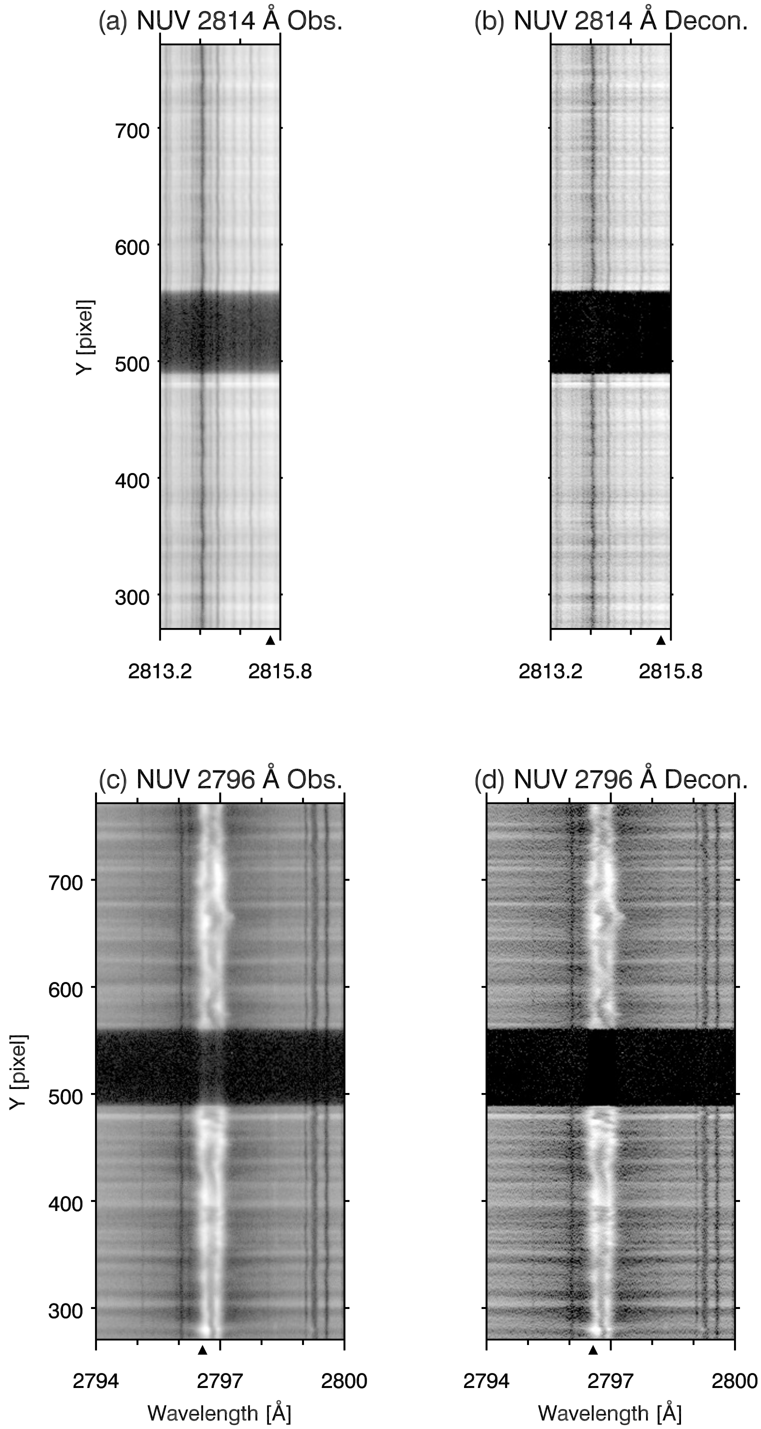

Figure 3.11: Comparison of original (**a**) and deconvolved (**b**) images for the IRIS FUV 2814 Å window. Remaining panels follow the same format: (**c, d**) 2796 Å. Spectra are square root scaled.

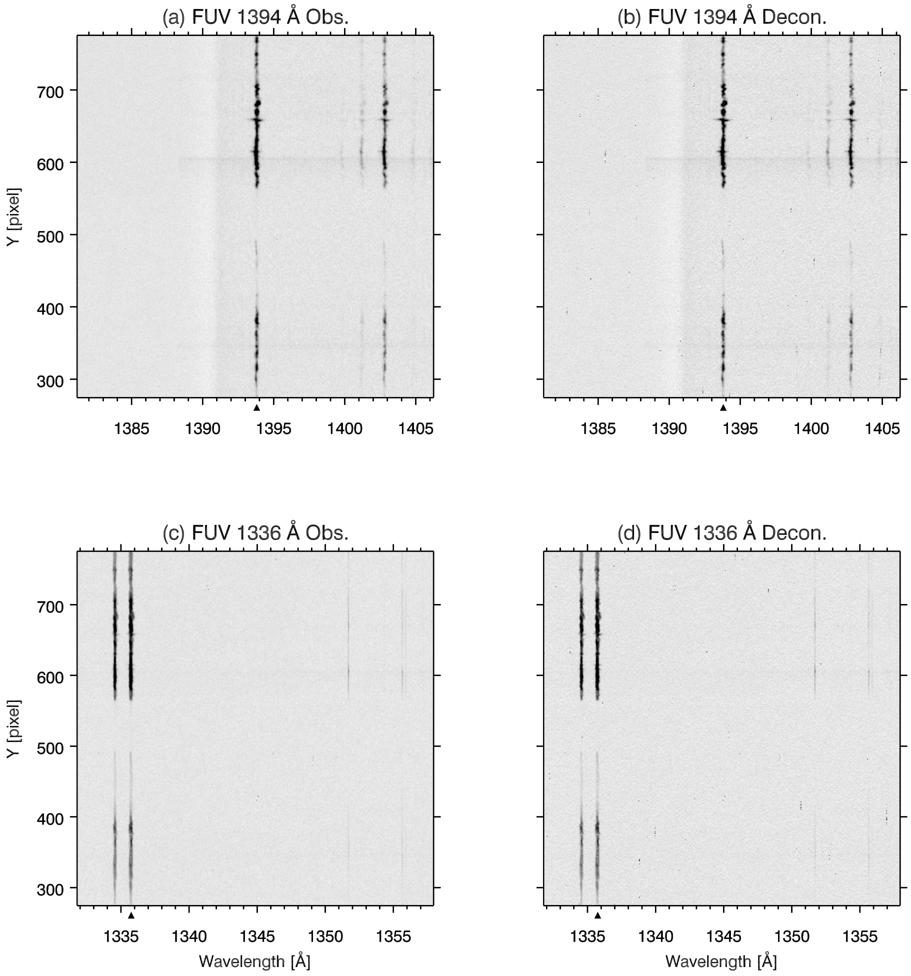

Figure 3.12: Comparison of original (**a**) and deconvolved (**b**) images for the IRIS FUV 1394 Å window. Remaining panels follow the same format: (**c, d**) 1336 Å. Intensity is displayed in inverse gray scale and logarithmically scaled.

NUV spectra (a) and (c) of Figure 3.11, is eliminated in Mercury's shadow in the corresponding deconvolved spectra (b) and (d).

The FUV channels show only modest improvement, since our FUV PSF estimates are essentially pixel limited. Scattered light is not apparent in either (a) or (c) of Figure 3.12 so that deconvolution in (b) and (d) has little to improve upon in this regard. Some sharpening of Mercury's limbs is evident in panels (c) and (d) of

Figure 3.13.

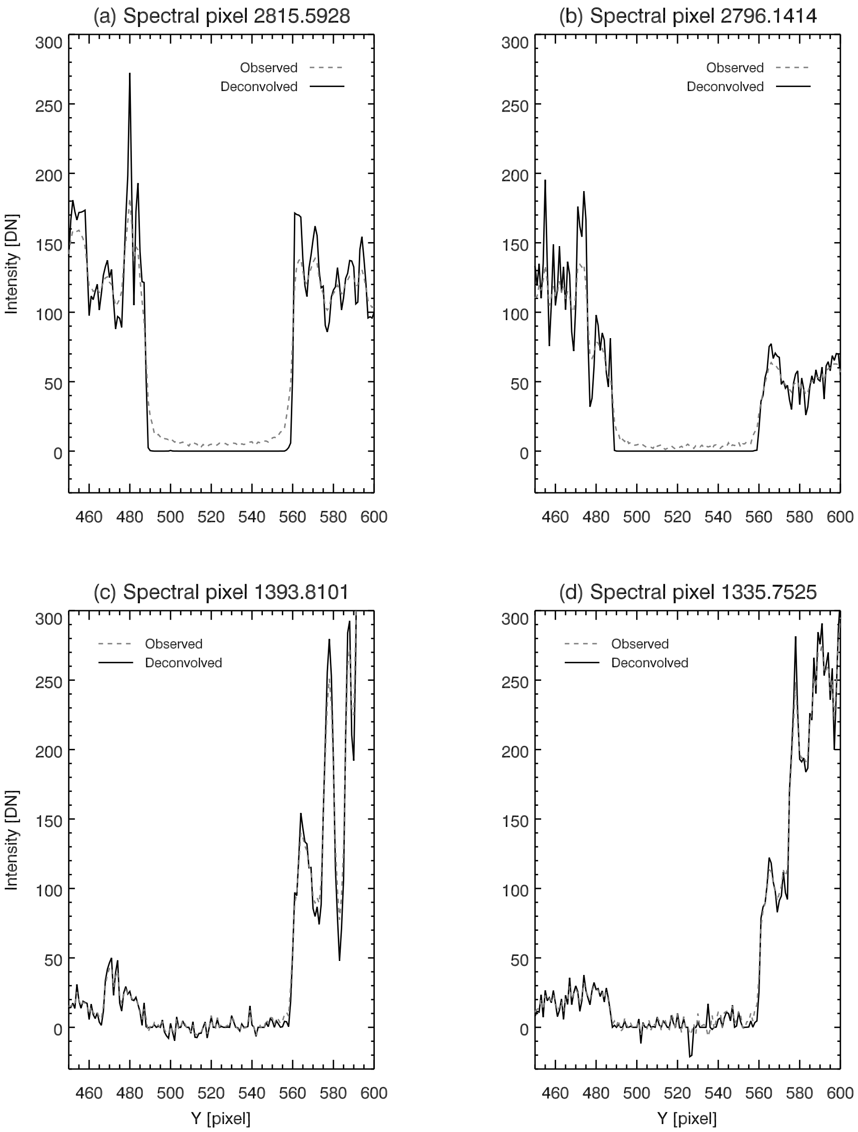

Figure 3.13: (**a**) Depicts intensity variations along a single spectral cut indicated by the black triangle on the wavelength axis in Figure 3.11 (a) and (b). Panels (**b**), (**c**), and (**d**) show the same for Figure 3.11 (c, d), and Figure 3.12 (e, f), and (g, h), respectively.

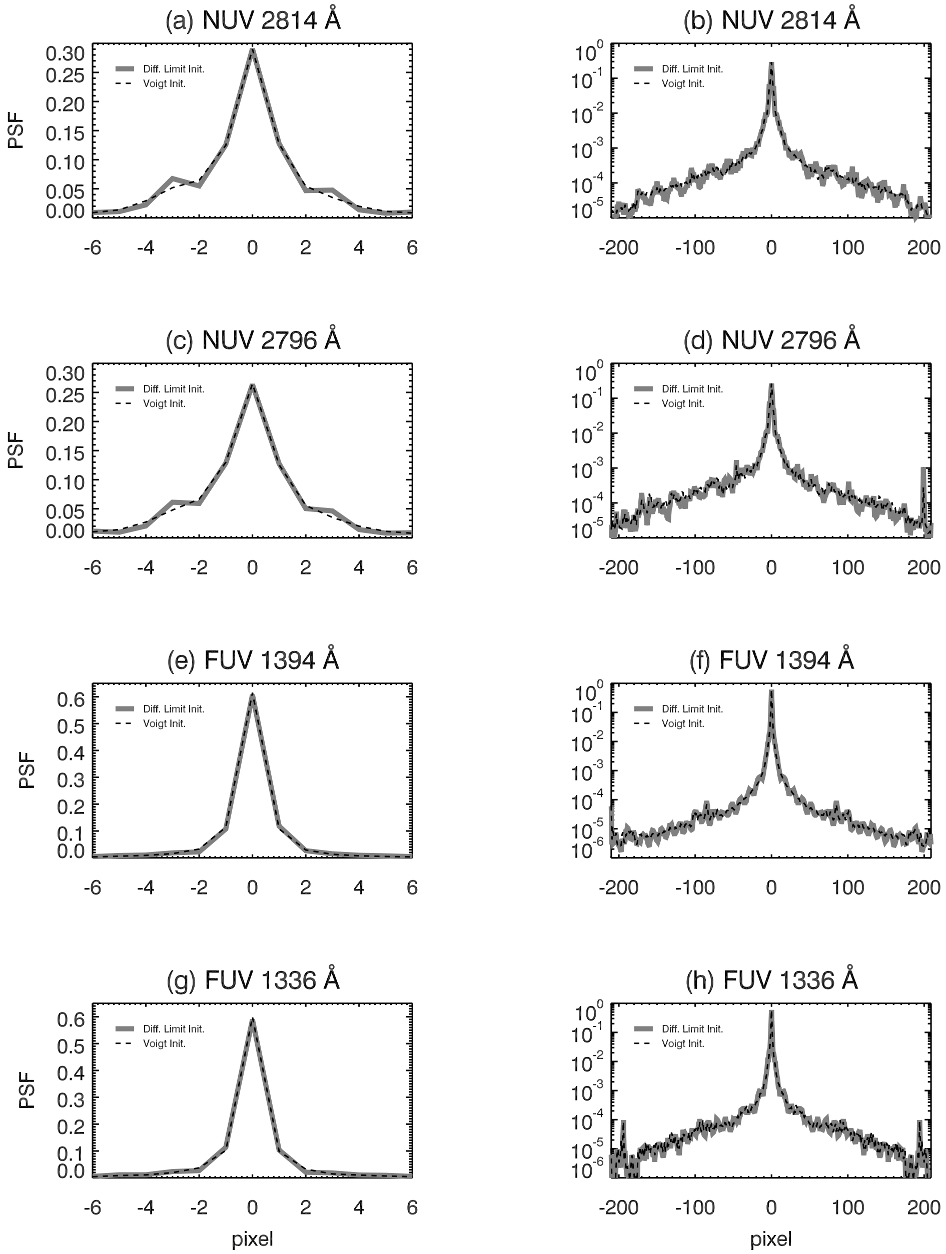

Figure 3.14: Comparison of results from an alternate Voigt PSF initialization (*gray curve*) to diffraction-limited (*black curve*) for the four spectral windows. Both initializations result in prominent side lobes in the core of the (**a**) 2814 and (**c**) 2796 Å PSFs. For all PSFs derived from the Voigt initialization, the wings of the PSF are smoother; however, a distinct discontinuity appears at ≈ ±65 pixels in panels (**b**), (**d**), and (**f**) and ≈ ±120 pixels in panel (**h**).

3.4.1 Effect of the Initial Guess on the PSF

Our initial guess was a diffraction-limited PSF (Figure 3.4). To find how much this initial guess influences our results, we substituted a Voigt profile, fit to the diffraction-limited PSF, as the initializing PSF. A complete exploration of the initializing parameter space is beyond the scope of this document; we choose Voigt profiles as an alternate initialization since it is fundamentally different from the Fourier model PSFs. The initial Voigt profiles are smoother and lack the side lobes and undulating structure of the Fourier models.

PSF estimates from both initializations are compared in Figure 3.14; similar core structures and distinct, asymmetric side lobes result from either initialization (*i.e.* Figure 3.14 (a) and (c)) for the NUV PSFs. We note that the side lobes and asymmetry appear in the NUV Voigt PSFs estimates, despite the absence of these traits in the initializing PSF. For all channels, the PSFs developed from the Voigt initialization have wings that are less noisy, and lack the undulations due to diffraction. This shows that our blind deconvolution method does not resolve fine structure far from the core of the PSF. Yet, the wings still fall off at similar rate compared to the diffraction-limited initialization. Subtle steps are visible in the wings in each NUV channel for the Voigt initialization (±65 pixels panels (b) and (d) of Figure 3.14). Since these features appear in both NUV PSFs for this initialization, their presence may be genuine. They may also appear in the diffraction-initialized PSFs; however, their existence is somewhat obscured by undulations in the wing.

As a further diagnostic of initial conditions, we perform the deconvolutions in Section 3.4.2 using both the Fourier model and the Voigt initialized PSF. Side by side results from either initialization can then be compared. Hereafter we refer to the spectra obtained from the Voigt initialized PSF estimates as the alternate deconvolved spectra.

3.4.2 PSF Effect on Data

To demonstrate the effect of the SG PSFs on IRIS observations, we consider a simple example of an explosive event (EE). Explosive events are ubiquitous, compact events characterized by large, non-thermal Doppler broadenings [$\approx$ 100 km s^{-1} to the red or blue; Dere et al., 1989, Dere, 1994] and may exhibit a bi-directional jet structure [Innes et al., 1997]. Typically EEs were observed in the FUV [*e.g.*, Si IV 1393 Å, and C IV 1548 and 1550 Å, Dere et al., 1989, Innes et al., 1997], but are also detected at EUV and NUV wavelengths [*e.g.*, He II 304 Å and Mg II 2796 Å, Fox et al., 2010, Huang et al., 2014]. Observations of bright, compact, and often isolated EEs are particularly sensitive to any PSF-induced blurring, and can serve as a diagnostic of the IRIS SG PSFs. For our example, we select a typical EE observed by IRIS close to disc center, shown in the boxed region of Figure 3.15 (a). This event is well isolated from nearby bright features and is captured in only one frame in both the NUV and the FUV channels. Its Doppler signature is clearly visible in Mg II (pixel 89 of panel (b), Figure 3.15) and particularly obvious in Si IV emission (panel (c), Figure 3.15). We use the 2796 Å and 1396 Å PSF estimates to deconvolve the spectra in Figure 3.15 (b) and (c), respectively. Deconvolution is performed using the same method described in Section 3.3.1.2, again truncating after 50 iterations for the 2796 Å and 10 iterations for the 1403 Å window.

The observed and deconvolved EE Mg II k wing spectra are plotted in Figure 3.16. Labeling of the Mg II profile follows convention, with features blueward of the line core (k_3) denoted by v and redward by r. Leenaarts et al. [2013b] describe diagnostics of the upper chromosphere using the Mg II h & k features, based on the formation properties discussed in detail in Leenaarts et al. [2013a]. In Table 3.4 we re-list the Mg II k spectral observables from Pereira et al. [2013], with the addition of the values observed from the NUV EE spectra for reference. The IDL routine `iris_get_mg_features.pro` [Pereira et al., 2013] was used to derive the spectral observables for the EE in Table 3.4. If we were observing quiet Sun, the derived numerical values in Table 3.4 could be directly interpreted. However, we note that EEs are very dynamic and likely differ significantly from the plasma conditions in the quiescent Bifrost [Gudiksen et al., 2011] simulations on which the results from Leenaarts et al. [2013a] and Leenaarts et al. [2013b] are based. We only use Table 3.4 to illustrate the quantitative impact of the deconvolution, and we do not mean to imply that the derived numerical values are necessarily correlated with the physical variables identified in Leenaarts et al. [2013b] and Pereira et al. [2013]. Interpreted in this manner, Table 3.4 shows that deconvolution has significant impact on the diagnostic parameters of the Mg II line profile.

Analysis of the Si IV EE spectra plotted in Figure 3.17 is more straightforward. The spectra are first background subtracted using the mean spectral value of the region bordered by the white horizontal lines in Figure 3.15 (c) (the background is computed after deconvolution for the deconvolved spectra). The equivalent width is calculated between the vertical dashed lines in Figure 3.17, the approximate locations of where the shoulder of the spectral line goes to zero. This provides a direct measure of the spectral extent of the EE in each case. Since the FUV PSFs are very nearly diffraction-limited, the effects of deconvolution are very subtle. In the example shown in Figure 3.17, equivalent width is only slightly reduced in the deconvolved spectra. We attribute the decrease in width to a combination of slightly increased fidelity in the deconvolved spectra and the introduction of noise from the deconvolution process.

Figures 3.16 and 3.17 and Table 3.4 all show that the Voigt and Fourier PSF initializations return identical results under deconvolution. We therefore conclude that the differences in the two PSF estimates in Figure 3.14 are below the level of accuracy that the underlying data can provide. We choose to provide the diffraction-limited PSF estimates in the associated SSW routine since these estimates are based on the physical properties of the instrument.

Table 3.4: Correlation between Mg II Features and Atmospheric Properties.

Spectral Observable	Atmospheric Property	Obs.	Deconv.	Alt. Dcv.
Δv_{k3}^{*}	Upper chromospheric velocity	7.0	6.2	6.2
Δv_{k2}^{*}	Mid chromospheric velocity	19.0	24.4	24.4
$\Delta v_{k3} - \Delta v_{h3}^{*}$	Upper chromospheric velocity gradient	-1.1	-4.9	-4.9
k peak separation*	Mid chromospheric velocity gradient	39.4	50.0	50.0
k_2 peak intensity†	Chromospheric temperature	586.7	601.8	601.8
$(I_{k2v} - I_{k2r})/(I_{k2v} + I_{k2r})^{\dagger}$	Sign of velocity above $z(\tau = 1)$ of k_2	0.3	0.4	0.4

$*$ [$\mathrm{km\,s^{-1}}$]
$\dagger$ [DN]

3.5 Concluding Remarks

The PSF of the IRIS spectrograph results in non-zero intensity in the occulted area during a Mercury transit. From the Mercury transit spectra, we estimated instrument spatial PSFs for four spectral windows (2814 Å, 2796 Å, 1394 Å, and 1336 Å) of the NUV and FUV SG channels using a semi-blind Richardson–Lucy method.

In the NUV channel, we find similar PSFs in both the 2814 Å and the 2796 Å windows over multiple data sets. The NUV PSFs have broader cores and asymmetric side lobes, as well as broadened wings when compared to the diffraction-limited case (see, *e.g.*, Figures 3.4, 3.7, and 3.8). The pixel-limited Strehl ratio (PLSR) is 0.73 and 0.65 for the 2814 Å and 2796 Å windows, respectively. The PLSR is affected by increased energy in the side lobes and scattering wings of our PSF estimates. MTFs show that the NUV SG has a resolution (defined by MTF > 0.9) of 0.42 cycles/pixel (2.55 cycles/arcsec) and 0.41 cycles/pixel (2.47 cycles/arcsec) in the 2814 Å and 2796 Å windows, respectively.

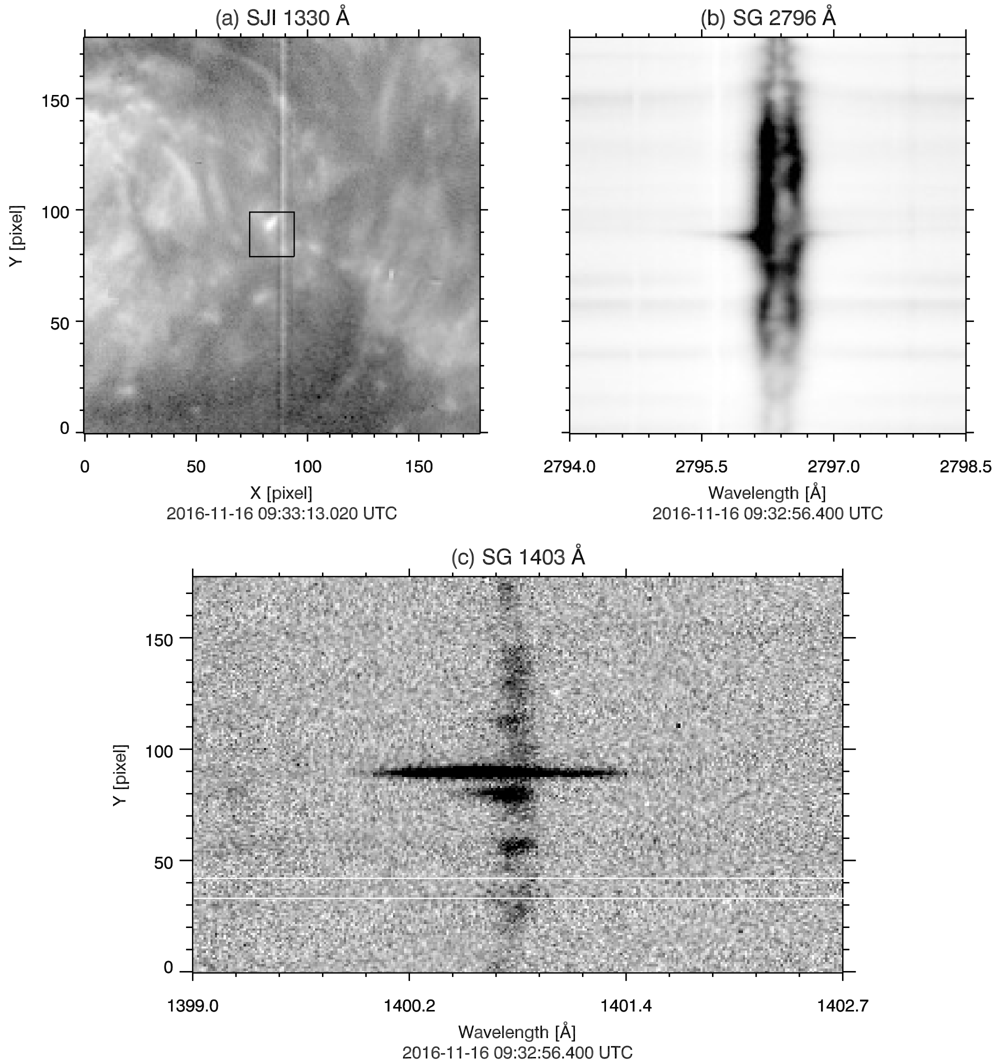

Figure 3.15: (**a**) IRIS SJI 1330 Å image of the explosive event used as a diagnostic of the SG PSFs. Boxed region outlines the approximate location of the EE (note that the SJI image was taken 17 s after the SG images). The EE results in a broadening of the spectra near Y pixel 89 in Mg II (**b**) and Si IV (**c**) emission. *White horizontal lines* in (**c**) denote the region used for the FUV background subtraction.

For the FUV 1394 Å and 1336 Å windows, we estimate PSFs with 0.98 and 0.93 PLSR, respectively. The FUV MTFs are within 10% of their ideal values in both windows. The SG achieves Nyquist-limited resolution in both FUV channels.

We find that the IRIS SG PSFs contain more energy in the wings than the

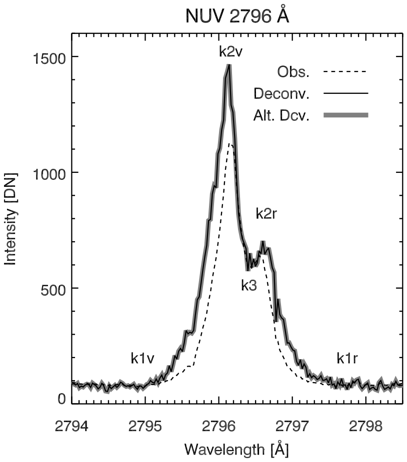

Figure 3.16: Mg II k wing EE spectra.

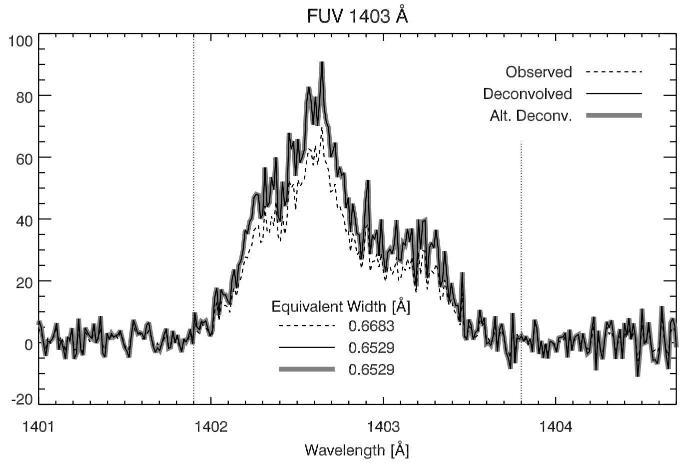

Figure 3.17: Si IV EE spectra. Equivalent width is calculated between *dashed vertical lines.*

diffraction-limited PSFs in both the NUV and the FUV channels. We attribute this excess to scattering. Contrary to our expectations, scattering is apparently more prevalent in the NUV PSFs than in FUV.

Our results are derived from IRIS Level 2 SG data, which is blurred slightly by geometrical correction. We cannot reliably separate this contribution to our PSF estimates from intrinsic instrument effects. Therefore, we underestimate the true instrument performance.

Deconvolution of the PSF estimates improves the spectra in both FUV and NUV channels. Applied to the Mercury spectral data, we find that deconvolution reduces the residual intensity in Mercury's shadow to a fraction of a DN in all channels, indicating that scattered light is reduced to near zero. NUV PSF artifacts, such as the blurring of Mercury's limb, are also greatly reduced while contrast is enhanced, with no adverse effects noted. When applied to the spectra of an isolated EE, we find that deconvolution reveals significant differences in intensity and sometimes velocities derived from the Mg II (NUV) line profiles. Deconvolution of the FUV EE spectra produces more subtle results, reducing the equivalent width of the line profile by 0.02 Å. In addition, the deconvolution can improve assessment of the physical size of detected features in both FUV and NUV channels.

The PSFs estimated here are distributed through SolarSoft (SSW) IDL, along with a program, `iris_sg_deconvolve.pro`, for direct application to IRIS level 2 data. PSFs for the 2814, 2796, 1394, and 1336 Å spectral windows are contained in the module, corresponding to the NUV and both FUV channels. The module performs a Richardson–Lucy deconvolution using the corresponding PSF estimate for each spectral window. The provided software will allow the community to perform more extensive testing of deconvolution of different types of solar scenes.

3.6 Acknowledgements

Funding for this work was supplied through subcontract 8100002702 from Lockheed Martin, in support of phases C/D/E of the NASA *Interface Region Imaging Spectrograph (IRIS) mission.* B.D.P. and J.P.W. were supported by NASA contract NNG09FA40C (*IRIS*).

Disclosure of Potential Conflicts of Interest The authors declare that they have no conflicts of interest.

CHAPTER FOUR

THE EUV SNAPSHOT IMAGING SPECTROGRAPH (ESIS)

Contribution of Authors and Co–Authors

Manuscript in Chapter 4

Author: Hans T. Courrier

Contributions: Responsible for optical design and optimization. Contributed to design and construction of instrumentation. Drafted manuscript and managed contributions from co-authors.

Co–Author: Charles C. Kankelborg

Contributions: Principal investigator; conceived and designed instrumentation. Contributed research and content to introduction. Provided feedback of analysis and comments on drafts of the manuscript.

Co–Author: Amy Winebarger

Contributions: Co-investigator; contributed research and content to introduction. Contributed to development of Camera assembly.

Co–Author: Ken Kobayashi

Contributions: Co-investigator; Contributed to development of Camera assembly.

Co–Author: Brent Beabout

Contributions: Designed camera assembly electronics and interface hardware.

Co–Author: Dyana Beabout

Contributions: Designed camera and ground support equipment software.

Co–Author: Ben Carroll

Contributions: Designed field stop mount and camera baffles.

Co–Author: Jonathan Cirtain

Contributions: Co-investigator; Led collaborative effort between MSU and Marshall Space Flight Center (MSFC.)

Co–Author: James A. Duffy

Contributions: Designed camera assembly mount and hardware.

Co–Author: Carlos Gomez

Contributions: Provided thermal analysis of camera assembly.

Co–Author: Eric Gullikson

Contributions: Developed and applied EUV multi-layer coatings to optics.

Co–Author: Micah Johnson

Contributions: Designed and constructed alignment transfer apparatus.

Co–Author: Jake Parker

Contributions: Assembled and aligned instrument optics.

Co–Author: Laurel Rachmeler

Contributions: Provided analysis and characterization of cameras.

Co–Author: Roy T. Smart

Contributions: Developed and implemented software for instrument computer control systems.

Co–Author: Larry Springer

Contributions: Managed MSU resources and interface between MSU and MSFC.

Co–Author: David L. Windt

Contributions: Designed and developed EUV multi-layer for ESIS optics.

Manuscript Information

Hans T. Courrier, Charles C. Kankelborg, Amy R. Winebarger, Ken Kobayashi, Brent Beabout, Dyana Beabout, Ben Carroll, Jonathan W. Cirtain, James A. Duffy, Carlos Gomez, Eric M. Gullikson, Micah Johnson, Jacob D. Parker, Laurel A. Rachmeler, Roy T. Smart, Larry Springer, David L. Windt

Status of Manuscript:
_x_ In preparation for submission to a peer–reviewed journal pending co-author contribution
____ Officially submitted to a peer–reviewed journal
____ Accepted by a peer–reviewed journal
____ Published in a peer–reviewed journal

ABSTRACT

The Extreme ultraviolet Snapshot Imaging Spectrograph (ESIS) is a next generation rocket borne instrument that will investigate magnetic reconnection and energy transport in the solar atmosphere using the transition region O V 62.9 nm and coronal Mg X 62.5 nm emission lines. The instrument is a pseudo Gregorian telescope; from prime focus, an array of spherical diffraction gratings re-image with differing dispersion angles. The slitless multi-projection design will obtain co-temporal spatial ($0.76''$/pixel) and spectral (37 mÅ/pixel) images at high cadence (<4 s). A single exposure will enable us to reconstruct line profile information at high spatial and spectral resolution over a large ($11.3'$) field of view. The instrument is currently in the build up phase prior to spacecraft integration, testing, and launch.

4.1 Introduction

The solar atmosphere, as viewed from space in its characteristic short wavelengths (FUV, EUV, and soft X-ray), is a three dimensional scene evolving in time: $I[x, y, \lambda, t]$. Here the solar sky plane spatial coordinates, x and y, and the wavelength axis, λ, comprise the three dimensions of the scene, while t represents the temporal axis. An ideal instrument would capture a spatial/spectral data cube ($I[x, y, \lambda]$) at a rapid temporal cadence (t), however, practical limitations lead us to accept various compromises of these four observables. Approaching this ideal is the fast tunable filtergraph (*i.e.* fast tunable Fabry–Pérot etalons, *e.g.* The GREGOR Fabry–Pérot Interferometer, Puschmann et al. [2012]), but the materials do not exist to extend this technology to extreme ultraviolet wavelengths (EUV) shortward of $\sim$150 nm [Wuelser et al., 2000]. Imagers like the *Transition Region and Coronal Explorer (TRACE)* [Handy et al., 1999] and the *Atmospheric Imaging Assembly (AIA)* [Lemen et al., 2012] collect high cadence 2D EUV spatial scenes, but they collect spectrally integrated intensity over a fixed passband that is not narrow enough to isolate a single emission line. In principle, filter ratios that make use of spectrally adjacent multilayer EUV passbands could detect Doppler shifts [Sakao et al., 1999]. However, the passbands of the multilayer coatings are still wide enough that the presence of weaker contaminant lines limits resolution of Doppler shifts to $\sim$1000 km s^{-1} [Kobayashi et al., 2000]. Slit spectrographs (*e.g. The Interface Region Imaging Spectrograph, IRIS* [De Pontieu et al., 2014]) obtain fast, high resolution spatial and spectral observations, but are limited by the narrow field of view (FOV) of the spectrograph slit. The $I[x, y, \lambda]$ data cube can be built up by rastering the slit pointing, but it cannot be co-temporal along the raster axis. Moreover, extended and dynamic scenes can change significantly in the time required to raster over their extant.

A different approach is to forego the entrance slit employed by traditional spectrographs entirely. The Naval Research Laboratory's (NRL) SO82A [Tousey et al., 1973, 1977] was one of the first instruments to pioneer this method. The 'overlappograms' obtained by SO82A identified several spectral line transitions [Feldman et al., 1985], and have more recently been used to determine line ratios in solar flares [Keenan et al., 2006]. Unfortunately, for closely spaced EUV lines, the dispersed images from the single diffraction order suffer from considerable overlap confusion. Image overlap is all but unavoidable with this configuration, however, overlappograms can be disentangled, or inverted, under the right circumstances.

In analogy to a tomographic imaging problem [Kak and Slaney, 1988], inversion of an overlapping spatial/spectral scene can be facilitated by increasing the number of independent spectral projections, or 'look angles,' through the 3D (x, y, λ) scene [DeForest et al., 2004]. For example, DeForest et al. [2004] demonstrated recovery of Doppler shifts in magnetograms from two dispersed orders of a grating at the output of the *Michelson Doppler Imager (MDI [Scherrer et al., 1995]).* The quality of the inversion (*e.g.* recovery of higher order spectral line moments) can also be improved by additional projections [Kak and Slaney, 1988, Descour et al., 1997], generally at the cost of computational complexity [Hagen and Dereniak, 2008]. *Computed Tomographic Imaging Spectrographs (CTIS)* [Okamoto and Yamaguchi, 1991, Bulygin et al., 1991, Descour and Dereniak, 1995] leverage this concept by obtaining multiple, simultaneous dispersed images of an object or scene; upwards of 25 grating diffraction orders may be projected onto a single detector plane [Descour et al., 1997]. Through post processing of these images, CTIS can recover a 3D data cube from a (spectrally) smooth and continuous scene over a large bandpass (*e.g.* Hagen and Dereniak [2008]).

The Multi-Order Solar EUV Spectrograph (MOSES Fox et al. [2010], Fox [2011]) is our first effort aimed at developing the unique capability of simultaneous imaging and spectroscopy for solar EUV scenes. MOSES is a three-order slitless spectrograph that seeks to combine the simplicity of the SO82A concept with the advantages of a CTIS instrument. A single diffraction grating (in conjunction with a fold mirror) projects the $m = \pm 1$ and the un-dispersed $m = 0$ order onto three different detectors. Through a combination of dispersion and multi-layer coatings, the passband of the $m = \pm 1$ orders encompasses only a few solar EUV emission lines. Thus, MOSES overlappograms consist of only a handful of spectral images. This constraint on the volume of the 3D data cube helps make inversion of MOSES data better-posed despite the discontinuous nature of the solar EUV spectrum. This working concept enabled by MOSES has been proven over the course of two previous rocket flights. Through inversion of MOSES overlappograms, Fox et al. [2010] obtained unprecedented measurements of Doppler shifts (*i.e.* line widths) of TR explosive events as a function of time and space while Rust [2017] recovered splitting and distinct moments of compact TR bright point line profiles.

Building on the working concept demonstrated by MOSES, here we describe a new instrument, the EUV Snapshot Imaging Spectrograph (ESIS), that will improve on past efforts to produce a solar EUV spectral map. ESIS will fly alongside MOSES and will observe the transition region (TR) and corona of the solar atmosphere in the O V 63.0 nm and Mg X 62.5 nm and 61.0 nm spectral lines. In Section 4.2 we detail how our experience with the MOSES instrument has shaped the design of ESIS. Section 4.3 describes the narrow scientific objectives and the requirements placed on the new instrument. Section 4.4 describes the technical approach to meet our scientific objectives, followed by a brief description of the expected mission profile in Section 4.5. The current status and progress toward launch is summarized in Section 4.6.

4.2 The ESIS Concept

A primary goal of the ESIS instrument is to improve the implementation of EUV snapshot imaging spectroscopy demonstrated by MOSES. Therefore, the design of the new instrument draws heavily from experiences and lessons learned through two flights of the MOSES instrument. ESIS and MOSES are both slitless, multi-projection spectrographs. As such, both produce dispersed images of a narrow portion of the solar spectrum, with the goal of enabling the reconstruction of a spectral line profile at every point in the field of view. The similarities end there, however, as the optical layout of ESIS differs significantly from that of MOSES. In this section, we detail some difficulties and limitations encountered with MOSES, then describe how the new design of ESIS addresses these issues.

4.2.1 Limitations of the MOSES Design

The MOSES design features a single concave diffraction grating forming images on three CCD detectors [Fox et al., 2010] (Fig. 4.1). The optical path is folded in half by a single flat secondary mirror (omitted in Fig. 4.1). Provided that the three cameras are positioned correctly, this arragement allows the entire telescope to be brought into focus using only the central (undispersed) order and a visible light source. Unfortunately this design uses volume inefficiently for two reasons. First, the lack of magnification by the secondary mirror limits the folded length of the entire telescope to be no less than half the 5 m focal length of the grating [Fox et al., 2010, Fox, 2011]. Second, the dispersion of the instrument is controlled by the placement of

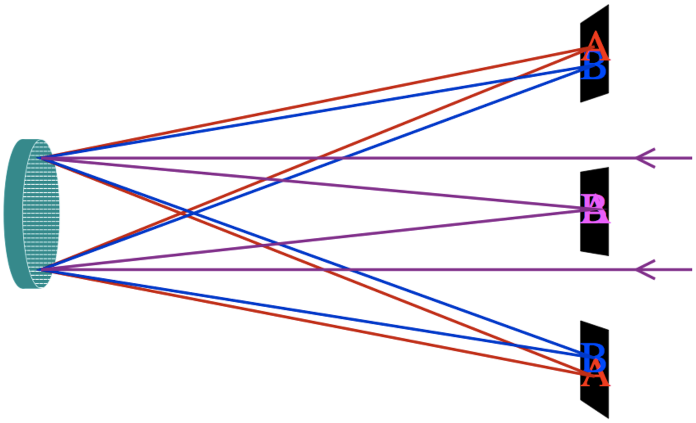

Figure 4.1: Schematic diagram of the MOSES instrument. Incident light on the right forms an undispersed image on the central $m = 0$ CCD. Dispersed images are formed on the outboard $m = \pm 1$ CCDs.

the cameras. To achieve the maximum dispersion of $29\,\mathrm{km\,s^{-1}}$ [Fox et al., 2010], the outboard orders are imaged as far apart as possible in the $\sim 22''$ diameter cross section of the rocket payload. The resulting planar dispersion poorly fills the cylindrical volume of the payload, leaving much unused space along the orthogonal planes.

Furthermore, the monolithic secondary, though it confers the focus advantage noted above, does not allow efficient placement of the dispersed image order cameras. For all practical purposes, the diameter of the payload (0.56 m) can only accommodate three diffraction orders ($m = -1, 0, +1$). Therefore, *MOSES can only collect, at most, three pieces of information at each point in the field of view.* From this, it is not reasonable to expect the reconstruction of more than three degrees of freedom in this spectrum, except in the case very compact, isolated features such as those described by Fox et al. [2010] and Rust [2017]. Consequently, it is a reasonable approximation to say that MOSES is sensitive primarily to spectral line intensities, shifts, and widths [Kankelborg and Thomas, 2001]. With any tomographic apparatus, the degree of detail that can be resolved in the object depends critically on the number of viewing angles [Kak and Slaney, 1988, Descour et al., 1997, Hagen and Dereniak, 2008]. So it is with the spectrum we observe with MOSES: more dispersed images are required to confer sensitivity to finer spectral details such additional lines in the passband or higher moments of the spectral line shape.

A related issue stems from the use of a single grating, with a single plane of dispersion. Since the solar corona and transition region are structured by magnetic fields, the scene tends to be dominated by field aligned structures such as loops [Rosner et al., 1978, Bonnet et al., 1980]. When the MOSES dispersion direction happens to be aligned nearly perpendicular to the magnetic field, filamentary structures on the transition region serve almost as spectrograph slits unto themselves. The estimation of Doppler shifts then becomes a simple act of triangulation, and broadenings are also readily diagnosed [Fox et al., 2010, Courrier and Kankelborg, 2018]. A double-peaked profile can also be observed with sufficiently isolated features [Rust, 2017]. Unfortunately, solar magnetic fields in the transition region are quite complex and do not have a global preferred direction. In cases where the field is nearly parallel to the instrument dispersion, spectral shifts and broadenings are not readily apparent.

The single diffraction grating also leads to a compromise in the optical performance of the instrument. Since the MOSES grating forms images in three orders simultaneously, aberration cannot be simultaneously optimized for all three of those spectral orders. A result of this design is that the orientations (*i.e.* the central axis) of the PSFs vary order to order [Rust, 2017]. During the first mission, MOSES was flown with a small amount of defocus [Rust, 2017], which exacerbated the inter-order PSF variation and caused the individual PSFs to span several pixels [Rust, 2017, Atwood and Kankelborg, 2018]. The combination of these two effects results in spurious spectral features that require additional consideration [Atwood and Kankelborg, 2018] and further increase the complexity of the inversion process [Rust, 2017, Courrier and Kankelborg, 2018].

Another complication is that the spatial and spectral content differs slightly between the three MOSES image orders. This is because the MOSES FOV is defined by a combination of the aperture of the grating (*i.e.* the entrance aperture of the telescope) and the spatial extent of the CCDs. The FOV in the $m = \pm 1$ orders is shifted along the dispersion axis as a function of wavelength, dependant upon where the dispersed spectral images intercept the $m = \pm 1$ CCDs. Spatially, this effect is limited to only a handful of pixel columns at the edges of each image order. Of higher concern is the 'spectral contamination' allowed by this layout; Parker and Kankelborg [2016] found that bright spectral lines and continuum far outside the wavelength passband and nominal $m = 0$ FOV could be diffracted onto the outboard order CCDs. This off-band contamination is detected as systematic intensity variation that lacks an anti-symmetric pairing in the opposite dispersed image order. Analysis of the spectral contamination is ongoing.

Finally, the exposure cadence of MOSES is hindered by an ∼6 s readout time for the CCDs [Fox, 2011]. The observing interval for a solar sounding rocket flight is very short, typically about five minutes. Consequently, every second of observing time is precious, both to achieve adequate exposure time and to catch the full development of dynamical phenomena. The MOSES observing duty cycle is ∼50 % since it is limited by the readout time of the CCDs. Thus, valuable observing time is lost. The readout data gap impelled us to develop a MOSES exposure sequence with exposures ranging from 0.25-24 s, a careful trade-off between deep and fast exposures.

In summary, our experience leads us to conclude that the MOSES design has the following primary limitations:

1. inefficient use of volume

2. dispersion constrained by payload dimensions

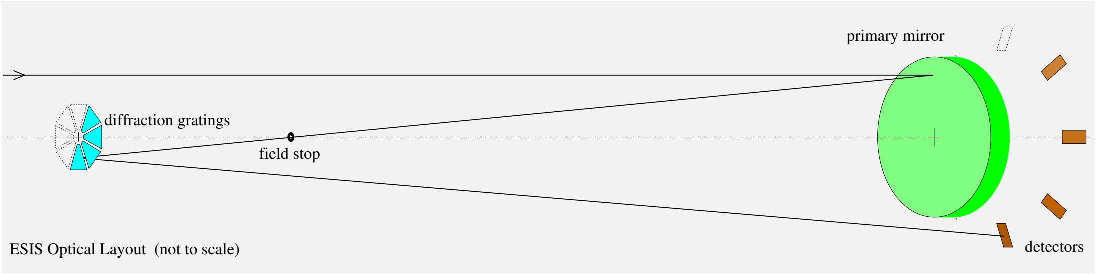

Figure 4.2: The ESIS instrument is a pseudo-Gregorian design. The secondary mirror is replaced by a segmented array of concave diffraction gratings. The field stop at prime focus defines instrument spatial/spectral FOV. CCDs are arrayed around the primary mirror, each associated with a particular grating. Eight grating positions appear in this schematic; only six fit within the volume of the rocket payload. Four channels are populated for the first flight.

3. too few dispersed images (orders)
4. single plane dispersion
5. lack of aberration control
6. insufficiently defined FOV
7. sub-optimal exposure cadence

In designing ESIS, we have sought to improve upon each of these points.

4.2.2 ESIS Features

The layout of ESIS (Fig. 4.2) is a modified form of Gregorian telescope. Incoming light is brought to focus at an octagonal field stop by a parabolic primary mirror. In the ESIS layout, the secondary mirror of a typical Gregorian telescope is replaced by a segmented, octagonal array of diffraction gratings. From the field stop, the gratings re-image to CCD detectors arranged radially around the primary mirror. The gratings are blazed for first order, so that each CCD is fed by a single corresponding grating, and all the gratings are identical in design. The features of this new layout address all of the limitations described in Sect. 4.2.1, and are summarized here.

Replacing the secondary mirror with an array of concave diffraction gratings confers several advantages to ESIS over MOSES. First, the magnification of the ESIS gratings results in a shorter axial length than MOSES, without sacrificing spatial or spectral resolution. Second, the magnification and tilt of an individual grating controls the position of the dispersed image with respect to the optical axis, so that the spectral resolution is not as constrained by the payload dimensions. Third, the radial symmetry of the design places the cameras closer together, resulting in a more compact instrument. Furthermore, by arranging the detectors around the optical axis, more dispersed grating orders can be populated; up to eight gratings can be arrayed around the ESIS primary mirror (up to six with the current optical table). This contrasts the three image orders available in the planar symmetry of MOSES. Taken together, these three design features make ESIS more compact than MOSES (§ 4.2.1 item 1), improve spectral resolution (§ 4.2.1 item 2) and allow the collection of more projections to better constrain the interpretation of the data (§ 4.2.1 item 3).

The ESIS gratings are arranged in a segmented array, clocked in 45° increments, so that there are four distinct dispersion planes. This will greatly aid in reconstructing spectral line profiles since the dispersion space of ESIS occupies a 3D volume rather than a 2D plane as with MOSES. For ESIS, there will always be a dispersion plane within 22.5° of the normal to any loop-like feature in the solar atmosphere. As discussed in § 4.2.1, a nearly perpendicular dispersion plane allows a filamentary structure to serve like a spectrographic slit, resulting in a clear presentation of the spectrum. This feature addresses § 4.2.1 item 4.

Rather than forming images at three spectral orders from a single grating, each ESIS imaging channel has a dedicated grating. Aberrations are controlled by optimizing the grating design to form images in first order, over a narrow range of ray deviation angles. This design controls aberration well enough to allow pixel-limited imaging, avoiding the PSF mismatch problems inherent to the MOSES design (§ 4.2.1 item 5). A disadvantage of this arrangement is that ESIS lacks a zero order focus. In its flight configuration with gratings optimized around a 63 nm wavelength, the instrument cannot be aligned and focused in visible light like MOSES. Visible gratings and a special alignment transfer apparatus (§ 4.4.5) must be used for alignment and focus of ESIS.

The ESIS design also includes an octagonal field stop placed at prime focus. This confers two advantages. First, the field stop fully defines the instrument FOV, so that ESIS is not susceptible to the spectral contamination observed in MOSES data (§ 4.2.1 limitation 6). Second, each spectral image observed by ESIS will be bordered by the outline of the field stop (*e.g.* § 4.4.1). This aids the inversion process since outside of this sharp edge the intensity is zero for any look angle through an ESIS data cube. Additionally, the symmetry of the field stop gives multiple checkpoints where the edge inversion is duplicated in the dispersed images produced by adjacent orders. The size and octagonal shape of the field stop are defined by the requirement that all CCDs must see the entire FOV from edge to edge, while leaving a small margin for alignment.

Lastly, in contrast to MOSES, ESIS employs frame transfer CCDs to make optimum use of our five minutes of observing time. The ESIS design is shutterless, so that each detector is always integrating. The result is a 100 % duty cycle. The lack of downtime for readout also allows ESIS to operate at a fixed, rapid cadence of ∼3 s. Longer integration times can be achieved for faint features by exposure stacking (§ 4.2.1 item 7).

In summary, the ESIS concept addresses all the limitations of the MOSES design enumerated in § 4.2.1. The volume of the ESIS optical layout is smaller than MOSES by almost a factor of two, yet with a smaller PSF, improved spectral resolution, and faster exposure cadence. ESIS offers several features to improve the recovery of spectral information, including more channels, crossed dispersion planes, and a field stop.

4.3 Science Objectives

The previous section discussed the qualitative design aspects of ESIS learned from experience with the MOSES instrument. MOSES, in turn, demonstrated a working concept of simultaneous EUV imaging and spectroscopy. This concept adds a unique capability to the science that we can obtain from the EUV solar atmosphere. ESIS, sharing the same payload volume as MOSES, is manifested to fly in 2019. In this section, we set forth specific scientific objectives for the combined ESIS/MOSES mission. From these objectives, and with an eye toward synergistic operation of MOSES and ESIS, in § 4.3.3 we derive the quantitative science requirements that drive the ESIS design.

The combined ESIS/MOSES mission will address the following two overarching science goals: (1) observe magnetic reconnection in the TR, and (2) map the transfer of energy through the TR with emphasis on magnetohydrodynamic (MHD) waves. These objectives have significant overlap with the missions of *IRIS* [De Pontieu et al., 2014], the *EUV Imaging Spectrometer* (*EIS*, Culhane et al. [2007]) aboard Hinode, the *EUV Normal-Incidence Spectrometer* (*EUNIS*, Brosius et al. [2007, 2014]), and a long history of FUV and EUV slit spectrographs. The ESIS instrument, however, can obtain both spatial and spectral information co-temporally. This will allow us to resolve complicated morphologies of compact TR reconnection events (as was done with MOSES [Fox, 2011, Rust, 2017, Courrier and Kankelborg, 2018]) and observe signatures of MHD waves over a large portion of the solar disk. Therefore, in support of goal 1, we will use ESIS and MOSES to map flows as a function of time and space in multiple TR reconnection events. To achieve goal 2, we will cross-correlate the evolution at multiple temperatures in the TR to map the vertical transport of energy over a wide FOV. In the latest configuration, the MOSES optics are optimized around Ne VII (0.5 MK). To achieve our goals, ESIS should have a complementary wavelength choice such that we can observe a reasonably isolated emission line formed in the lower TR.

4.3.1 Magnetic Reconnection Events

Magnetic reconnection describes the re-arrangement of the magnetic topology wherein magnetic energy is converted to kinetic energy resulting in the acceleration of plasma particles. Reconnection is implicated in many dynamic, high energy solar events. Solar flares are a well studied example (*e.g.* Priest and Forbes [2002] and the references therein), however we have little hope of pointing in the right place at the right time to observe a significant flare event in a rocket flight lasting only five minutes. Instead, we will search for signatures of magnetic reconnection in TR spectral lines. A particular signature of reconnection in the TR is the explosive energy release by ubiquitous, small scale events. These explosive events (EEs) are characterized as spatially compact (≈1.5 Mm length [Dere, 1994]) line broadenings on the order of $100\,\mathrm{km\,s^{-1}}$ [Dere et al., 1991]. They are observed across a range of TR emission lines that span temperatures of 20.000–250.000 K (C II–O V) [Moses et al., 1994]. The typical lifetime of an EE is 60-90 s [Moses et al., 1994, Dere, 1994, Dere et al., 1991]. Due to their location near quiet sun magnetic network elements, and the presence of supersonic flows near the Alfvèn speed, Dere et al. [1991] first suggested that EEs may result from fast Petschek [Petschek, 1964] reconnection.

The spectral line profile of EEs may indicate the type of reconnection that is occurring in the TR (*e.g.* Rust [2017]). For example, the Petschek model of reconnection predicts a 'bi-directional jet' line profile with highly Doppler shifted wings, but little emission from the line core [Innes and Tóth, 1999]. Innes et al. [2015] developed a reconnection model resulting from a plasmoid instability [Bhattacharjee et al., 2009]. In contrast to the bi-directional jet, this modeled line profile has bright core emission and broad wings. Both types of profile are seen in slit spectrograph data (*e.g.*, Innes et al. [1997, 2015], and the references therein), however MOSES observed EEs with more complicated morphologies than either of these two models suggest [Fox et al., 2010, Rust, 2017]. It is unclear whether the differing observations are a function of wavelength and temperature, a result of a limited number of observations, or because the morphology of the event is difficult to ascertain from slit spectrograph data.

ESIS will observe magnetic reconnection in the context of EEs, by extending the technique pioneered by MOSES to additional TR lines. Explosive events are well suited to sounding rocket observations; a significant portion of their temporal evolution can be captured in >150 s (*e.g.* the analysis by Rust [2017]) and they are sufficiently common to provide a statistically meaningful sample in a 5-minute rocket flight (*e.g.*, Dere et al. [1989, 1991]). In similarity with MOSES, we seek a TR line for ESIS that is bright and well enough isolated from neighboring emission lines so as to be easily distinguished.

4.3.2 Energy Transfer

Tracking the mass and energy flow through the solar atmosphere is a long-standing goal in solar physics. Bulk mass flow is evidenced by Doppler shifts or skewness in spectral lines. However, the observed non-thermal broadening of

TR spectral lines may result from a variety of physical processes, including MHD waves [De Pontieu et al., 2015, 2007], high-speed evaporative up-flows (*e.g.* nanoflares, Patsourakos and Klimchuk [2006]), turbulence, and other sources (*e.g.* Mariska [1992]). This is a broad topic which ESIS can address in many ways. Here we will focus on a single application; ESIS will search for sources of Alfvén waves in the solar atmosphere by observing line broadening as the spectroscopic signature of these waves.

Alfvén waves in coronal holes are observed to carry an energy flux of $7 \times 10^5\,\mathrm{erg/cm^2/s}$, enough to energize the fast solar wind [Hahn et al., 2012, Hahn and Savin, 2013]. The source and frequency spectrum of these waves is unknown. Here, we hypothesize that MHD waves are similarly ubiquitous in quiet Sun and active regions, and play an important role in the energization of the quiescent corona.

The magnitude of non-thermal broadening of optically thin spectral lines is a direct measure of the wave amplitude [Banerjee et al., 2009, Hahn et al., 2012, Hahn and Savin, 2013]. We may estimate a lower limit on the non-thermal velocity to be observed as follows. We assume that the magnetic field is constant for small changes in scale height in the TR and that line of sight effects are negligible for observations sufficiently far from disk center. Since the solar wind is not accelerated to an appreciable fraction of the Alfvén wave velocity at altitudes below $R \leq 1.15R_\odot$ [Cranmer and van Ballegooijen, 2005], the wave amplitude, v_{nt}, depends only weakly on electron density, n_e, so that $v_{nt} \propto n_e^{-1/4}$ [Hahn and Savin, 2013, Moran, 2001]. Assuming pressure balance between the low corona and transition zone, we may infer non-thermal velocities in the TR by scaling according to the temperature drop, $v_{nt} \propto T^{1/4}$. The measured non-thermal velocity of $24\,\mathrm{km\,s^{-1}}$ for Si VIII [Doyle et al., 1998] (0.8 MK [Moran, 2003]) near the limb should, neglecting damping, correspond to velocities of at least $21\,\mathrm{km\,s^{-1}}$ in mid TR Ne VII, and $18\,\mathrm{km\,s^{-1}}$ in the lower O V

(0.25 MK) line. The above non-thermal velocities are arrived at assuming both O V and Ne VII are formed near their ionization equilibrium temperatures. For O V, the thermal width is ∼11 km s^{-1} at 0.25 MK which means the total linewidth is primarily due to the non-thermal component.

More recently, Srivastava et al. [2017] observed torsional Alfvén waves with amplitude ∼20 km s^{-1} and period ∼30 s in the chromosphere. Modeling shows that these torsional waves can transfer a significant amount of energy to the corona [Kudoh and Shibata, 1999]. The torsional motion will be observed as Doppler shifts when viewed from the side. The oscillation period is long enough to be well resolved but short enough to see ∼10 cycles in a single rocket flight. An ESIS-like instrument is therefore well suited to observations of torsional Alfvén wave propagation over multiple heights in the TR.

By mapping Doppler velocities over a wide field of view in the TR, ESIS can address questions about both the origin of waves and whether they are able to propagate upward into the corona. Independent of the two propagation modes discussed above, there is a range of possible sources for Alfvén (and other MHD) waves in the solar atmosphere. Three potential scenarios are: (1) Waves originate in the chromosphere or below and propagate through the TR at a spatially uniform intensity ; (2) Intense sources are localized in the TR, but fill only a fraction of the surface; and (3) Weak sources are localized in the TR, but cover the surface densely enough to appear like the first case. The resulting non-thermal widths for localized sources will be significantly higher than the ∼20 km s^{-1} mean derived above. The concentration of non-thermal energy observed by ESIS will serve as an indicator of source density. Comparison of Doppler maps from ESIS and MOSES will indicate whether a uniform source density originates in the chromosphere or below (scenario 1) or is associated with spatially distributed TR phenomena (scenario 3) such as explosive events, or macrospicules. Comparison with a wider selection of ground and space based imagery will allow us to determine whether intense, localized sources (scenario 2) are associated with converging or emerging magnetic bipoles, type II spicules, spicule bushes, or other sources beneath the TR. For these comparisons, we need only to localize, rather than resolve, wave sources. A spatial resolution of ∼2 Mm will be sufficient to localize sources associated with magnetic flux tubes that are rooted in photospheric inter-granular network lanes (*e.g.* Berger et al. [1995]).

4.3.3 Science Requirements

ESIS will investigate two science targets; reconnection in explosive events, and the transport of mass and energy through the transition region. The latter may take many forms, from MHD waves of various modes to EUV jets or macro-spicules. To fulfill these goals, ESIS will obtain simultaneous intensity, Doppler shift and line width images of the O V 63 nm line in the solar transition region at rapid cadence. This is a lower TR line (0.25 MK) that complements the MOSES Ne VII. The bright, optically thin O V emission line is well isolated except for the two coronal Mg X lines. These coronal lines can be viewed as contamination or as a bonus; we expect that with the four ESIS projections it will be possible to separate the O V emission from that of Mg X. From the important temporal, spatial, and velocity scales referenced Sections 4.3.1 and 4.3.2 we define the instrument requirements in Table 4.1 that are needed to meet our science goals.

4.4 The ESIS Instrument

ESIS is a multiple projection slitless spectrograph that obtains line intensities, Doppler shifts, and widths in a single snapshot over a 2D FOV. Starting from the notional instrument described in Sec. 4.2, ESIS has been designed to ensure all of the

Table 4.1: ESIS instrument requirements. AR is active region, QS quiet sun, and CH coronal hole.

Parameter	Requirement	Science Driver	Capabilities
Spectral line	O v	Explosive events	O v, Mg x, & He i, Table 4.2
Spectral res.	$18\,\mathrm{km\,s^{-1}}$ broadening	MHD waves	18 km/s/ pixel, Table 4.2
Spatial res.	$2''$ (1.5 Mm)	Explosive events	$1.52''$, Table 4.2
Desired SNR	17.3 in CH	MHD waves in CH	>17.7 w/20×10 s exp., § 4.4.4
Cadence	15 s	Torsional waves	10 s eff., § 4.4.4
Obs. time	> 150 s	Explosive events	>270 s, § 4.5
FOV	$10'$ diam.	Span QS, AR, limb	$11.3'$, Table 4.2

science requirements set forth in Table 4.1 are met. The final design parameters are summarized in Table 4.2.

A schematic diagram of a single ESIS channel is presented in Fig. 4.3 [A], while the mechanical features of the primary mirror and gratings are detailed in Figs. 4.3 [B] and [C], respectively.

4.4.1 Optics

Figure 4.3 [A] shows the relative layout of the optics and detectors for a single ESIS channel. Here we give specific details of the primary mirror and gratings (Fig. 4.3 [B] and [C], respectively). The features of the field stop have been described previously in Sec. 4.2.2, while the CCD and cameras are covered in Sec. 4.4.7.

The primary mirror is octagonal in shape. A triangular aperture mask in front of the primary mirror defines the clear aperture of each channel, imaged by a single grating. Figure 4.3 [B] shows one such aperture mask superimposed upon the primary mirror. The octagonal shape of the primary also allows dynamic clearance for filter tubes that are arranged radially around the mirror (§ 4.4.3). The mirror is attached to a backing plate by three "bipods"; thin titanium structures that are flexible in the radial dimension, perpendicular to the mirror edge, but rigid in the other two dimensions. The bipods form a kinematic mount, isolating the primary mirror figure

Table 4.2: ESIS Design Parameters.

Primary	Parabolic
	Octagonal Aperture, D=144 mm
	Focal length 1.0 m
	SiC single layer coating optimized for λ63 nm
	Transparent vis/IR
Field Stop	11.3′, projected on sky plane
	Octagonal
Gratings (4)	Spherical varied line space
	(Individual master gratings)
	Trapezoidal Aperture, Height: 16.9 mm,
	Long Base: 18.0 mm, Short Base: 3.8 mm
	Groove spacing d_0=0.3866 µm
	Magnification M=3.9
	Mg/Al/SiC multilayer, λ63 nm
	Efficiency 14 % (Uncoated 39 %)
Filters (4)	30 mm clear aperture
	Thin film, 100 nm Al
	82 % open Ni mesh
Detectors (4)	E2V CCD230-42
	Active area 2048 × 1024
	Pixel size 15 µm
	QE 33 %, λ63 nm
	Max readout time or min cadence here for ver. table 1?
Back Focal Length	127 mm
Plate scale	0.76 ″/pixel
	37 mÅ (18 $\mathrm{km\,s^{-1}}$) per pixel
Resolution	1.52″ (Nyquist limited)

from mounting stress.

The mirror will have to maintain its figure under direct solar illumination, so low expansion (Corning ULE) substrates were used. The transparency of ULE, in conjunction with the transparency of the mirror coating in visible and near IR wavelengths (*e.g.*, Table 4.2 and § 4.4.3), helps minimize the heating of the mirror. Surface figure specifications for the ESIS optics are described in Sec. 4.4.2.

The spherical gratings (Fig. 4.3 [C]) re-image light from the field stop to form

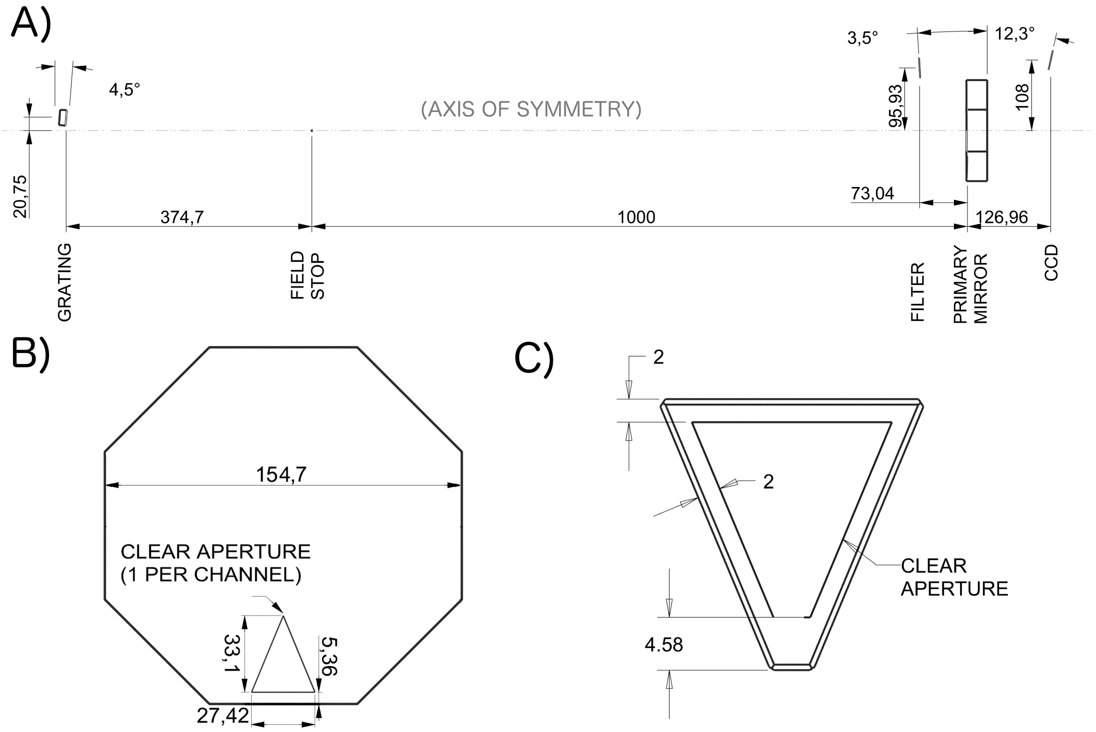

Figure 4.3: [A] Schematic diagram of the ESIS optical train. Dimensions and clear aperture of the ESIS [B] primary mirror and [C] diffraction gratings.

dispersed images at the CCDs. Each grating is individually mounted to a backing plate in a similar fashion as the primary mirror. For these much smaller optics, lightweight bipods were wire EDM cut from thin titanium sheet. The bipods are bonded to both the grating and backing plate along the three long edges of each grating. The individual mounts allow each grating to be adjusted in tip and tilt to center the image on the CCD.

The gratings have a varied line space ruling pattern optimized to provide, in principle, pixel limited imaging from the field stop to the CCDs. The pitch at the center of the grating is d_0 =0.3866 µm resulting in a dispersion of 17.5 $\mathrm{km\,s^{-1}}$ at the center of the O v FOV. The groove profile is optimized for the $m = 1$ order, so that each grating serves only a single CCD. The modeled grating groove efficiency in this

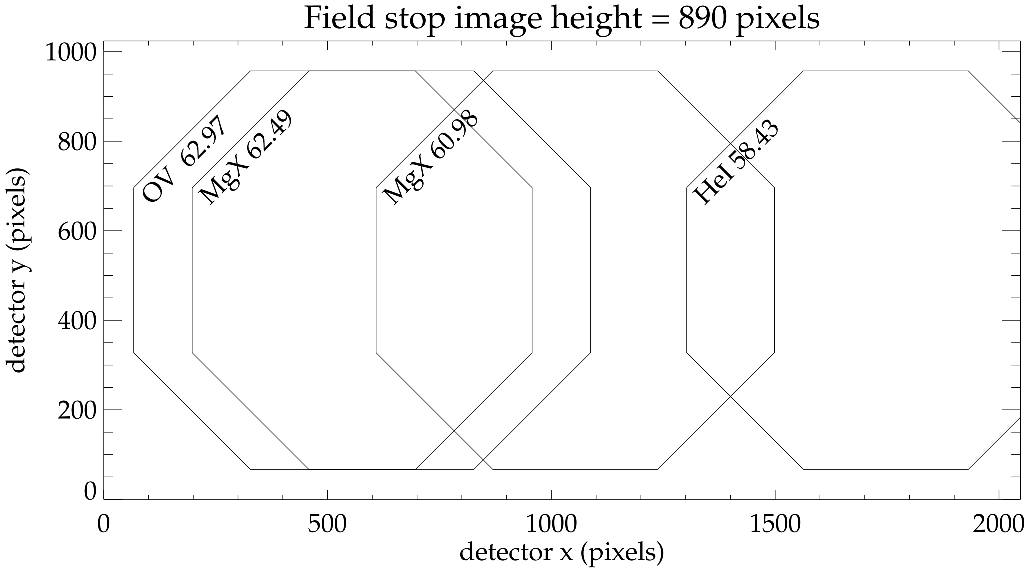

Figure 4.4: Areas occupied by strong spectral lines on the ESIS detectors. The plot axes are sized exactly to the CCD active area. The ESIS passband is defined by a combination of the field stop and grating dispersion.

order is 36 % at 63 nm.

Figure specification and groove profile are not well controlled near the edges of the gratings. Therefore, a baffle is placed at each grating to restrict illumination to the clear aperture marked in Fig. 4.3 [C].

The ESIS passband is defined through a combination of the field stop, the grating dispersion, and the CCD size. The passband includes the He I (58.43 nm) spectral line through Mg X (60.98 and 62.49 nm) to O V (62.97 nm). Figure 4.4 shows where images of each of the strong spectral lines will fall on the CCD. The instrument dispersion satisfies the spectral resolution requirement in Table 4.1 and ensures that the spectral images are well separated; Figure 4.4 shows that He I will be completely separated from the target O v line.

4.4.2 Optimization and Tolerancing

The science resolution requirement of 2.0″ (Table 4.1) was flowed down to specifications for the ESIS optics. To ensure that ESIS meets this requirement, an imaging error budget was developed to track parameters that significantly influence instrument resolution. The budget is roughly divided into two categories; the first includes ‘variable’ parameters that can be directly controlled (*e.g.*, the figure and finish of the optics, grating radius and ruling, placement of the elements in the system, and the accuracy to which the instrument is focused). The second category consists of ‘fixed’ contributions (*e.g.*, CCD charge diffusion, pointing stability, and diffraction from the entrance aperture). In this sub-section we describe the optimization of the first category to balance the contributions of the second.

Figure and surface roughness specifications for the primary mirror and gratings were developed first by a rule of thumb and then validated through a Fourier optics based model and MonteCarlo simulations. Surface figure errors were randomly generated, using a power law distribution in frequency. The model explored a range of power spectral distributions for the surface figure errors, with power laws ranging from 0.1 to 4.0. For each randomly generated array of optical figure errors, the amplitude was adjusted to yield a target MTF degradation factor, as compared to the diffraction limited MTF. For the primary mirror, the figure of merit was a MTF degradation of 0.7 at 2.0″ resolution. Though the grating is smaller and closer to the focal plane, it was allocated somewhat more significant MTF degradation of 0.6 based on manufacturing capabilities. The derived requirements are described in table 4.3. Note that this modeling exercise was undertaken before the baffle designs were finalized. The estimated diffraction MTF and aberrations were therefore modeled for a rough estimate of the ESIS single sector aperture.

Table 4.3: Figure and surface roughness requirements compared to metrology for the ESIS optics. Slope error (both the numerical estimates and the measurements) is worked out with integration length and sample length defined per ISO 10110.

Element	Parameter	Requirement	Measured
Primary	RMS Slope error (μrad)	< 1.0	
	integration length (mm)	4.0	
	sample length (mm)	2.0	
Primary	RMS roughness (nm)	< 2.5	
	Periods (mm)	0.1-6	
Grating	RMS slope error (μrad)	< 3.0	
	integration length (mm)	2	
	sample length (mm)	1	
Grating	RMS roughness (nm)	< 2.3	
	Periods (mm)	0.02-2	

The initial grating radius of curvature, R_g, and ruling pattern of the ESIS gratings were derived from the analytical equations developed by Poletto and Thomas [2004] for stigmatic spectrometers. A second order polynomial describes the ruling pattern,

$$d = d_0 + d_1 r + d_2 r^2 \,, \tag{4.1}$$

where r runs radially outward from the optical axis with its origin at the center of the grating (Fig. 4.3 [C]). The parameters of Equation 4.1 and R_g were chosen so that the spatial and spectral focal curves intersect at the center of the O v image on the CCD.

Starting from the analytically derived optical prescription, a model of the system was developed in ray-trace software. Since the instrument is radially symmetric, only one grating and its associated lightpath was analyzed. In the ray trace model, R_g, d_1, d_2, grating cant angle, CCD cant angle, and focus position were then optimized to minimize the RMS spot at select positions in the O v FOV, illustrated in Fig. 4.5.

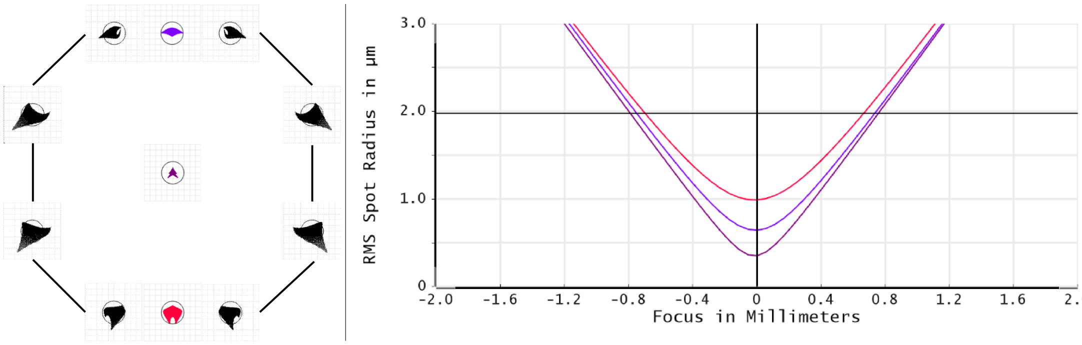

Figure 4.5: (Left:) Ray traced spot diagrams for ESIS, illustrated at the center and vertices of the O V FOV on the CCD. The grid spacing is 1 µm and the diffraction limit airy disk (overplotted on each spot) radius is 2 µm. Imaging performance will be limited by the 15 µm pixel size. (Right:) RMS spot radius through focus for the three centered spots; top of FOV (purple curve), center (maroon), and bottom (red).

The optical prescription derived from the ray trace is listed in Table 4.2 and 4.3.

The ray trace model was also used to quantify how mirror and positional tolerances affect the instrument's spatial resolution. Each element of the model was individually perturbed, then a compensation applied to adjust the image on the CCD. The compensation optimized grating tip/tilt angle and CCD focus position, so that the image was re-centered and RMS spot size minimized at the positions in Fig. 4.5. We then computed the maximum change in RMS spot size over all spot positions between the optimized and perturbed models. The computed positional tolerances for each element in the ESIS optical system are listed in Table 4.4

The imaging error budget is displayed in Table 4.4. For the primary mirror and grating surface figure contributions, we choose the MTF figures of merit from the surface roughness specifications described earlier. To quantify the remaining entries, we assume that each term can be represented by a gaussian function of width σ^2 that "blurs" the final image. The value of σ then corresponds to the maximum change in RMS spot size for each term as it is perturbed in the tolerance analysis described above. The value of the modulation transfer function (MTF) in the right-most column of Table 4.4 is computed from each of the gaussian blur terms at the Nyquist frequency (0.5 cycles/arcsecond). From Table 4.4, we estimate the total MTF of ESIS to be 0.109 at the Nyquist frequency. Compared to, for example, the Rayleigh criterion of 0.09 cycles/arcsecond [Lord Rayleigh F.R.S., 1879] we estimate the resolution of ESIS to be essentially pixel limited. Since ESIS pixels span $0.76''$, the resolution target in Table 4.1 is obtained by this design.

Table 4.4: Imaging error budget and tolerance analysis results. MTF is given at 0.5 cycles/arcsecond.

Element		Tolerance	σ^2 [μm]	MTF
Primary M.	Surface figure	(Ref. Table 4.3)		0.700
	Decenter	1 mm	1.700	0.881
Grating	Surface figure	(Ref. Table 4.3)		0.600
	Radius	2.5 mm	1.410	0.916
	Decenter	1 mm	0.001	1.000
	Defocus	0.015 mm	0.801	0.972
	Clocking	13 mrad	1.300	0.929
CCD	Decenter	1 mm	0.310	0.996
	Defocus	0.229 mm	0.706	0.978
Max RMS spot radius (modeled)			1.720	0.878
CCD charge diffusion (est.)			2.000	0.839
Thermal drift			0.192	0.998
SPARCS drift			1.920	0.998
Pointing jitter			3.430	0.597
Diff. Limit				0.833
Total MTF				0.109

4.4.3 Coatings and Filters

The diffraction gratings are coated with a multilayer optimized for a center wavelength of 63.0 nm, developed by a collaboration between Reflective X-Ray Optics LLC and Lawrence Berkeley National Laboratory (LBNL). In Fig. 4.6 (A), characterization of a single, randomly selected multilayer coated grating at LBNL

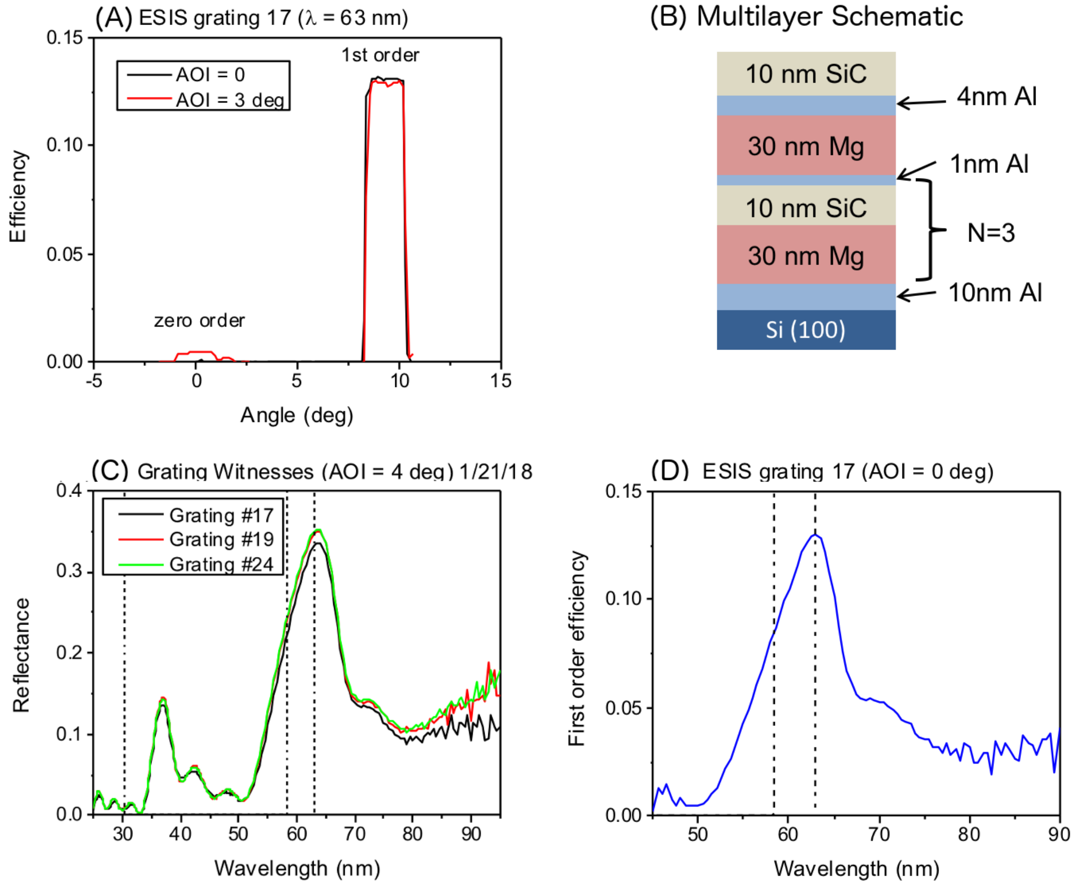

Figure 4.6: (A) Measured efficiency of a single grating as a function of reflection angle. Note flat response in first order over instrument FOV and suppression of zero order. (B) Schematic of the Al/SiC/Mg multilayer with $N = 4$ layers. (C) Measured reflectance for several multilayer coated witness samples. Dashed lines mark He I (left, 58.4 nm) and O V (right, 63.0 nm) emission line wavelengths, with additional vertical line showing suppression of He II emission (far left dashed line, 30.4 nm) (D) Measured multilayer coated grating efficiency as a function of wavelength. Dashed lines mark the same emission lines as in (C)..

shows that the grating reflectivity is constant over the instrument FOV in the $m = 1$ order while the $m = 0$ order is almost completely suppressed. Figure 4.6 (B) shows a schematic of the coating that achieves peak reflectivity and selectivity in the $m = 0$ order using four layer pairs of silicon carbide (SiC) and magnesium (Mg). The Aluminum (Al) layers are deposited adjacent to each Mg layer to mitigate corrosion.

The maximum reflectance for the coating alone in the nominal instrument passband is ∼35 % in Fig. 4.6 (C), measured from witness samples coated at the same time as the diffraction gratings. Combined with the predicted groove efficiency from § 4.4.1 and, given the relatively shallow groove profile and near normal incidence angle, the total reflectivity in first order is ∼13 % at 63 nm. This is confirmed by the first order efficiency measured from a single ESIS grating in Fig. 4.6 (D).

Unlike EUV imagers (*e.g.*, *TRACE* [Handy et al., 1999], *AIA* [Lemen et al., 2012], and Hi-C [Kobayashi et al., 2014]) the ESIS passband is defined by a combination of the field stop and grating (§ 4.4.1, Fig. 4.4) rather than multi-layer coatings. The coating selectivity is therefore not critical in this respect, allowing the multi-layer to be manipulated to suppress out-of-band bright, nearby emission lines. Figure 4.6 (D) shows the peak reflectance of the grating multilayer is shifted slightly towards longer wavelengths to attenuate the He I emission line, reducing the likelihood of detector saturation. A similar issue arises with the bright He II (30.4 nm) line. Through careful design of the grating multilayer, the reflectivity at this wavelength is ∼2 % of that at 63 nm (Fig. 4.6 (D)). In combination with the primary mirror coating (described below) the rejection ratio at 30.4 nm is ∼32 dB. Thus, He II emission will be completely attenuated at the CCD.

The flight and spare primary mirrors were coated with the same Al/SiC/Mg multilayer. Corrosion of this multilayer rendered both mirrors unusable. The failed coating was stripped from primary mirror SN001. The mirror was then re-coated with a 5 nm thick layer of chromium (Cr) to improve adhesion followed by a 25 nm thick layer of SiC. The reflectance of this coating deposited on a silicon (Si) wafer witness sample appears in Fig. 4.7. The spare primary mirror (SN002) retains the corroded Al/SiC/Mg multilayer.

The Si CCDs are sensitive to visible light as well as EUV. Visible solar radiation

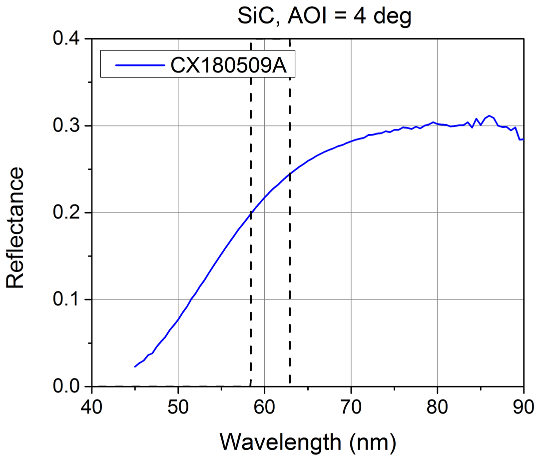

Figure 4.7: Measured reflectivity of the ESIS primary mirror 25 nm thick SiC coating deposited on a Si witness sample. Dashed lines mark He I (left, 58.4 nm) and O V (right, 63.0 nm) emission line wavelengths.

is much stronger than EUV, and visible stray light can survive multiple scatterings while retaining enough intensity to contaminate the EUV images. Luxél [Powell et al., 1990] Al filters 100 nm thick will be used to shield each CCD from visible light. The Al film is supported by a 70 line per inch (lpi) Ni mesh, with 82% transmission. The theoretical filter transmission curve, modeled from CXRO data [Henke et al., 1993], is displayed in Fig. 4.8. We conservatively estimate filter oxidation at the time of launch as a 4nm thick layer of Al_2O_3.

An Al filter is positioned in front of the focal plane of each CCD by a filter tube, creating a light tight box with a labyrinthine evacuation vent (e.g., Fig. 4.11). The placement of the filter relative to the CCD is optimized so that the filter mesh shadow is not visible. By modeling the filter mesh shadow, we find that a position far from the CCD (>200 mm) and mesh grid clocking of 45° to the detector array reduces the shadow amplitude well below photon statistics. The MOSES instrument utilizes a similar design; no detectable signature of the filter mesh is found in data and inversion residuals from the 2006 MOSES flight.

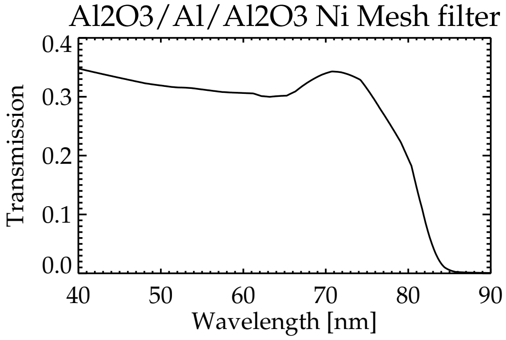

Figure 4.8: Model of ESIS filter transmissivity, including filter mesh and 4 nm thick oxidation layers on either side of the 100 nm Al film.

To prevent oxidation, and to minimize the risk of tears, pinholes, and breakage from handling, the filters will be stored in a nitrogen purged environment until after payload vibration testing.

4.4.4 Sensitivity and Cadence

Count rates for ESIS are estimated using the expected component throughput from Section 4.4.3 and the CCD quantum efficiency (QE) listed in Table 4.2. Line intensities are derived from Vernazza and Reeves [1978] (V&R) and the SOHO/Coronal Diagnostic Spectrometer (CDS) [Harrison et al., 1995] data. The 100 % duty cycle of ESIS (§ 4.4.7) gives us the flexibility to use the shortest exposures that are scientifically useful. So long as the shot noise dominates over read noise (which is true even for our coronal hole estimates at 10 s exposure length), we can stack exposures without a significant SNR penalty. Table 4.5 shows that ESIS is effectively shot noise limited with a 10 s exposure. The signal requirement in Table 4.1 is met by stacking exposures. Good quality images ($\sim$ 300 counts) in active regions can be obtained by stacking 30 s worth of exposures. This cadence is sufficient to observe explosive events, but will not resolve torsional Alfvén waves described in § 4.3. However, by stacking multiple 10 s exposures, sufficient SNR *and* temporal resolution of torsional Alfvén wave oscillations can be obtained. The count rates given here are for an unvignetted system as described in § 4.4.6.

Table 4.5: Estimated signal statistics per channel (in photon counts) for ESIS lines in coronal hole (CH), quiet Sun (QS), and active region (AR).

Source	V&R	V&R	V&R	CDS
Solar Context	QS	CH	AR	AR
10 s Exp.				
Mg x (62.5 nm)	3	0	26	16
O V (62.9 nm)	22	19	66	34
Total Counts	25	19	92	50
Shot Noise	5.0	4.3	9.6	7.0
Read Noise (est.)		– 1.9 –		
SNR	4.7	4.0	9.4	6.8
3×10 s Exp. Stack				
Total Counts	75	56	276	148
SNR	8.1	6.8	16.3	11.7

4.4.5 Alignment and Focus

In the conceptual phase of ESIS, the decision was made to perform focus and alignment in visible light with a HeNe source. Certain difficulties are introduced by this choice, however, the benefits outweigh the operational complexity and equipment that would be required for focus in EUV. Moreover, a sounding rocket instrument requires robust, adjustment-free mounts to survive the launch environment. Such a design is not amenable to iterative adjustment in vacuum. The choice of alignment wavelength is arbitrary for most components; CCD response and multilayer coating reflectively is sufficient across a wide band a visible wavelengths. The exceptions are the thin film filters (which will not be installed until just before launch and have no affect on telescope alignment and focus) and the diffraction gratings. Visible light gratings have been manufactured specifically for alignment and focus. These gratings are identical to the EUV flight version, but with a ruling pattern scaled to a 632.8 nm wavelength.

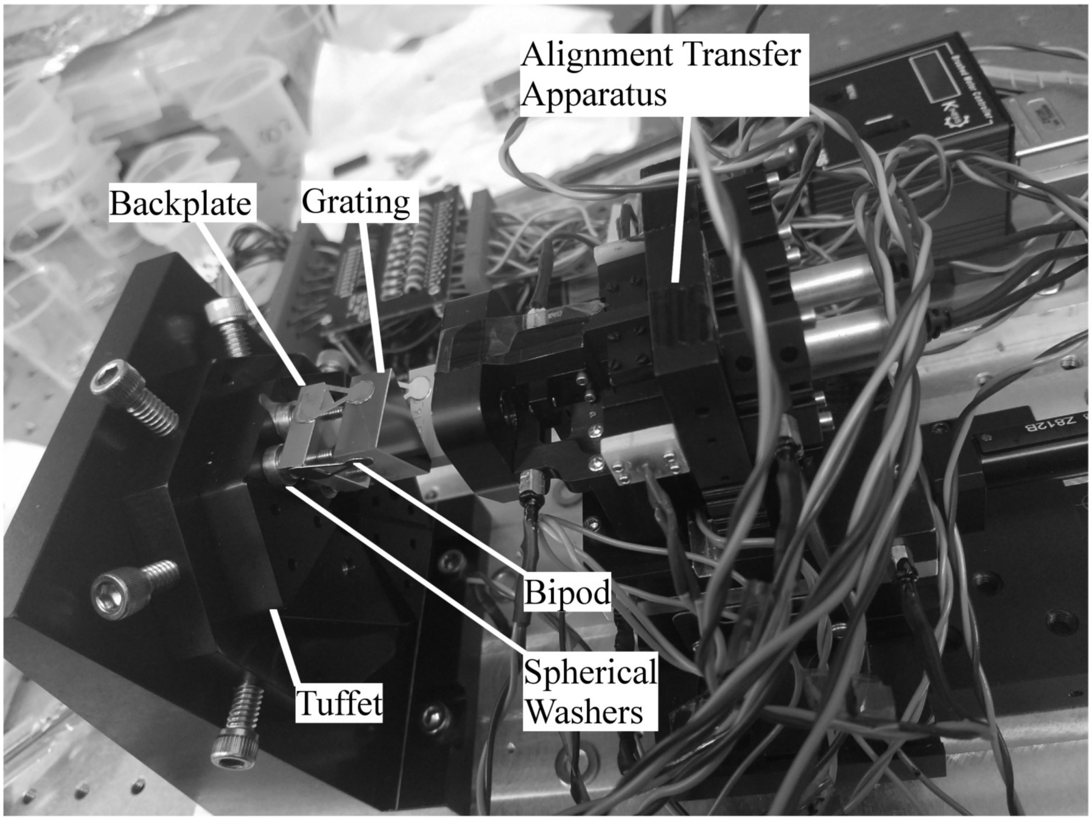

Figure 4.9: ESIS alignment transfer device, consisting of three miniature confocal microscopes that translate along the optical axis. Trapezoidal grating, bipods, and mounting plate are installed on the tuffet in front of the apparatus (left of center).

After alignment and focus has been obtained with the HeNe source, the instrument will be prepared for flight by replacing the visible gratings by the EUV flight versions. Each grating (EUV and alignment) is individually mounted to a backing plate using a bipod system similar to that of the primary mirror. The array of gratings on their backing plates are in turn mounted to a single part which we call the 'tuffet.' The backing plate is attached to the tuffet by bolts through spherical washers. With this mounting scheme, the gratings can be individually aligned in tip/tilt. The tuffet is attached to the secondary mirror mount structure (Fig. 4.9). This enables the entire grating array to be replaced simply by removing/installing the tuffet, such as when switching between alignment and EUV gratings.

Properly positioning the gratings will be the most difficult aspect of final telescope assembly. Table 4.4 shows that the telescope is very sensitive to defocus. The depth of field is an order of magnitude smaller in EUV than in visible light. Moreover, the sensitivity to defocus at the gratings is $M^2 + 1 = 17$ times greater than at the detectors. Another sensitive aspect of the telescope is grating tip/tilt. A tolerance of $\sim \pm 0.5\,\mathrm{mrad}$ will be needed to insure that the entire image lands on the active area of the CCD.

Once the visible gratings are aligned and focused, the challenge is to transfer this alignment to the UV gratings. Johnson et al. [2018] describes a procedure and the apparatus constructed to accurately transfer the position of an alignment grating radius to an EUV flight grating. This device, displayed in Fig. 4.9, consists of an array of three miniature confocal microscopes that record the position of the alignment grating radius. The alignment grating is replaced by an EUV grating, which is then measured into position by the same apparatus. This device (and procedure) is capable of obtaining position measurements of the diffraction gratings to a repeatability of $\approx 14\,\mu\mathrm{m}$ in the three confocal channels. This alignment transfer apparatus will ensure that the EUV flight gratings are positioned to within the tolerances described in Table 4.4.

4.4.6 Apertures and Baffles

Each channel of ESIS has two apertures: one at the surface of the grating and another in front of the primary mirror. The purpose of the aperture at the grating is to mask the out-of-figure margins at the edges of these optics. This provides a

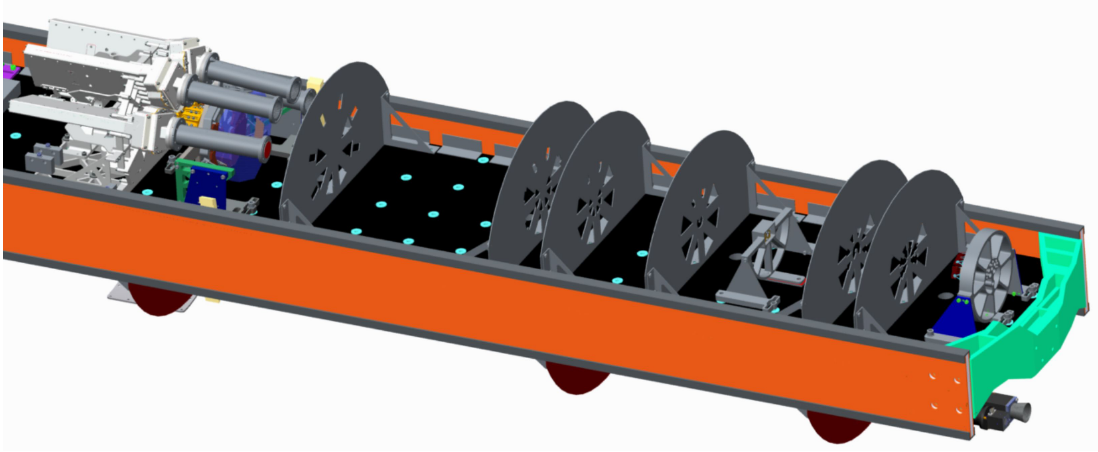

Figure 4.10: Model view of ESIS baffle placement and cutouts.

well defined edge to the clear aperture of each grating while also keeping unwanted rays from being reflected from the grating margins and back onto the CCDs. The dimensions of the grating aperture match those of the grating clear aperture shown in Figure 4.3 [C].

The aperture placed at the primary mirror is the stop for each individual channel. The area of the stop has been maximized under the constraint that no rays be vignetted anywhere else in the system. The gratings and their clear apertures were the most significant areas of concern for potential vignetting. Thus, the shape of stop at the primary is largely influenced by the shape of the grating clear aperture. The inner extent of the primary stop (the “tip” of the triangle in Figure 4.3 [B]) is defined by the occultation of the primary by the shadow cast from the gratings and their mounts. This presented an intricate geometry problem, as the occultation is a function of the incoming field angle, the radial extent of the grating mount, and the distance of the mount to the primary mirror along the optical axis. Hence, the inner extent of the primary stop was solved for iteratively with the optimization described in Section 4.4.2, which affected the placement of the gratings relative to the primary mirror. The resulting optimized and non-vignetting stop geometry is shown in Figure 4.3 [B].

After final optimization, the stop geometry was analyzed to check for vignetting at the grating with the optical model. A footprint diagram was generated at the grating from of multiple grids of rays. The incidence angle of each grid of rays corresponded to the extremes of FOV defined by the positions of the eight points of the octagonal field stop. The footprint diagram showed that, with the stop completely filled, no ray landed outside of the grating clear aperture in Figure 4.3 [C], and no ray was intercepted by the central obscuration.

From Figure 4.3 [C] it is apparent that considerable surface area of the primary mirror is unused by the non-vignetting stop design. The primary apertures could be enlarged considerably if the vignetting constraint were to be relaxed.

The ESIS baffles are designed to block direct light paths between the front aperture plate and the CCDs for any ray $<1.4^\circ$ from the optical axis. This angle is purposefully larger than the angular diameter of the sun ($\sim 0.5^\circ$) so that any direct paths are excluded from bright sources in the solar corona. All baffles are bead-blasted, anodized Al sheet metal oriented perpendicular to the optical axis. The size and shape of the cutouts were determined using a combination of the ray trace from Section 4.4.2 and 3D modeling. The light path from the primary mirror to the field stop is defined as the volume that connects each vertex of the primary mirror aperture mask (e.g., Fig. 4.3) to every vertex of the octagonal field stop. This is a conservative definition that ensures no rays within the FOV are excluded, and therefore unintentionally vignetted by the baffles. Light paths from the field stop to the grating, and from the grating to the image formed on the CCD, are defined in a similar manner. The cutouts in the baffles are sized using the projection of these light paths onto the baffle surface. A conservative 1 mm margin is added to each cutout to prevent unintentional vignetting. A model of the six baffles, showing cutouts and position on the optical bench, is displayed in Fig. 4.10.

4.4.7 Cameras

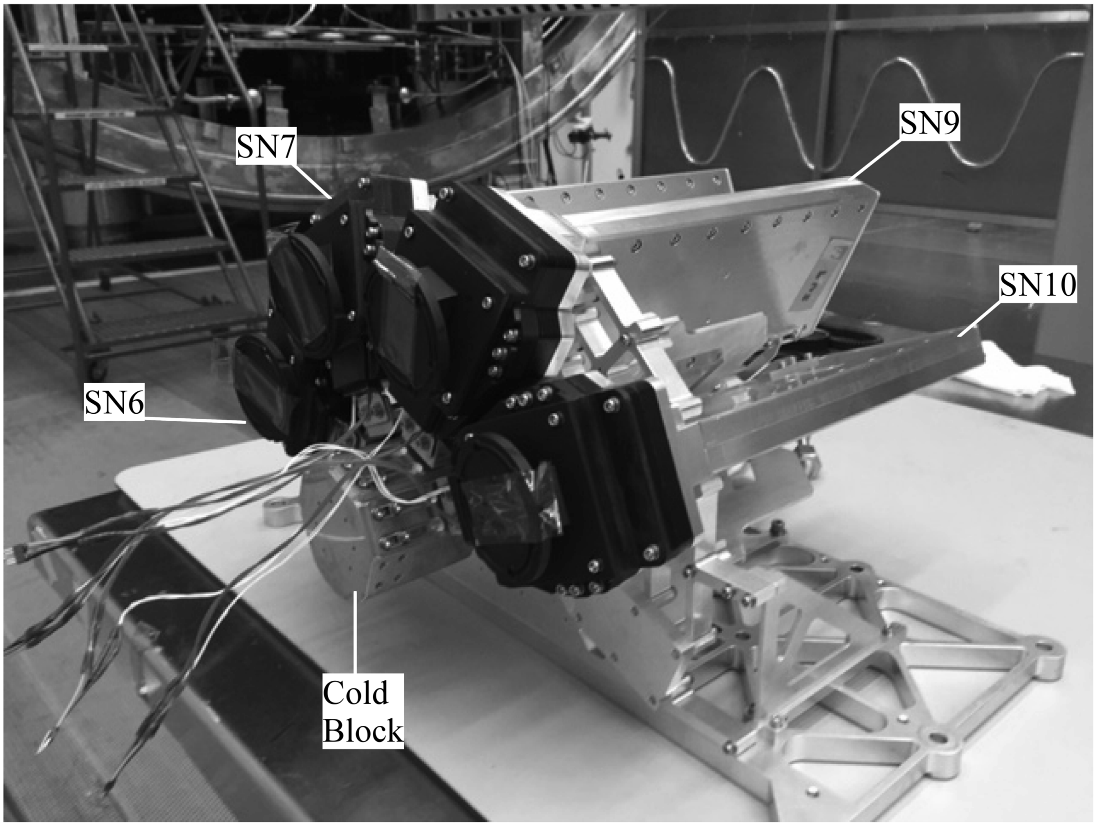

Figure 4.11: ESIS camera assembly as built by MSFC. Thin film filters and filter tubes are not installed in this image.

The ESIS CCD cameras were designed and constructed by Marshall Space Flight Center (MSFC), and are the latest in a series of camera systems developed specifically for use on solar space flight instruments. The ESIS camera heritage includes those flown on both the Chromospheric Lyman-Alpha Spectro-Polarimeter (CLASP) [Kano et al., 2012, Kobayashi et al., 2012] and the High-Resolution Coronal Imager (Hi-C)[Kobayashi et al., 2014].

The ESIS detectors are CCD230-42 astro-process CCDs from E2V. For each camera, the CCD is operated in a split frame transfer mode with each of the four ports read out by a 16-bit A/D converter. The central 2048×1024 pixels of the $2k \times 2k$ device are used for imaging, while the outer two regions are used for storage. Two overscan columns on either side of the imaging area and eight extra rows in each storage region will monitor read noise and dark current. When the camera receives the trigger signal, it transfers the image from the imaging region to the storage regions and starts image readout. The digitized data are sent to the Data Acquisition and Control System (DACS) through a SpaceWire interface immediately, one line at a time. The frame transfer takes $<$60 ms, and readout takes 1.1 s. The cadence is adjustable from 2-600 s in increments of 100 ms, to satisfy the requirement listed in Table 4.1. Because the imaging region is continuously illuminated, the action of frame transfer (transferring the image from the imaging region to the storage regions) also starts the next exposure without delay. Thus the exposure time is controlled by the time period between triggers. Camera 1 (Fig. 4.11) generates the sync trigger, which is fed back into Camera 1's trigger input and provides independently buffered triggers to the remaining three cameras. The trigger signals are synchronized to better than ±1 ms. Shutterless operation allows ESIS to observe with a 100 % duty cycle. The cadence is limited only by the 1.1 s readout time.

MSFC custom designed the camera board, enclosure, and mounting structure for ESIS to fit the unique packaging requirements of this experiment (Fig 4.11). The front part of the camera is a metal block which equalizes the temperature across the CCD while fastening it in place. The carriers of all cameras are connected to a central two-piece copper (3 kg) and aluminum (1 kg) thermal reservoir (cold block) by flexible copper cold straps. The flexible cold straps allow individual cameras to be translated parallel to the optical axis (by means of shims) up to ∼13 mm to adjust focus in each channel prior to launch. The centrally located cold block will be cooled by LN2 flow from outside the payload until just before launch. The LN2 flow will be controlled automatically by a Ground Support Equipment (GSE) computer so that all cameras are maintained above survival temperature but below the target temperature of −55 °C to insure a negligible dark current level.

The gain, read noise, and dark current of the four cameras were measured at MSFC using an ^{55}Fe radioactive source. Cameras are labeled 1, 2, 3, and 4 with associated serial numbers SN6, SN7, SN9, and SN10 respectively in Fig. 4.11. Gain ranges from 2.5-2.6 e^-/DN in each quadrant of all four cameras. Table 4.6 lists gain, read noise, and dark current by quadrant for each camera.

The Quantum Efficiency (QE) of the ESIS CCDs will not be measured before flight. Similar astro-process CCDs with no AR coating are used in the Solar X-ray Imager (SXI) aboard the Geosynchronous Orbiting Environmental Satellites (GOES) N and O. A QE range of 43% at 583Å to 33% at 630Å is expected for the ESIS CCDs, based on QE measurements by Stern et al. [2004] for GOES SXI instruments.

4.4.8 Avionics

The ESIS DACS are based on the designs used for both CLASP [Kano et al., 2012, Kobayashi et al., 2012] and Hi-C [Kobayashi et al., 2014]. The electronics are a combination of Military Off-The-Shelf (MOTS) hardware and custom designed components. The DACS is a 6-slot, 3U, open VPX PCIe architecture conduction cooled system using an AiTech C873 single board computer. The data system also include a MOTS PCIe switch card, MSFC parallel interface card, and two MOTS Spacewire cards. A slot for an additional Spacewire card is included to accommodate two more cameras for the next ESIS flight. The C873 has a 2.4 GHz Intel i7 processor with 16 Gb of memory. The operating temperature range for the data system is -40

Table 4.6: ESIS Camera properties.

Camera	Quad	Gain $[e^{-}/DN]$	Read Noise [DN]	Dark Current $[e^{-}/ms]$
1 (SN6)	1	2.57	3.9	$1.37e^{-}4$
	2	2.50	4.0	$9.66e^{-}5$
	3	2.52	4.1	$6.85e^{-}5$
	4	2.53	3.7	$9.80e^{-}5$
2 (SN7)	1	2.55	3.9	$6.77e^{-}5$
	2	2.58	4.0	$5.89e^{-}5$
	3	2.57	4.0	$8.98e^{-}5$
	4	2.63	4.0	$1.01e^{-}4$
3 (SN9)	1	2.57	4.1	$3.14e^{-}5$
	2	2.53	4.1	$2.68e^{-}5$
	3	2.52	4.1	$3.18e^{-}5$
	4	2.59	4.3	$3.72e^{-}5$
4 (SN10)	1	2.60	3.9	$6.39e^{-}4$
	2	2.60	3.9	$5.07e^{-}5$
	3	2.54	4.2	$6.63e^{-}5$
	4	2.58	4.1	$8.24e^{-}5$

to +85 C. The operating system for the flight data system is Linux Fedora 23.

The DACS is responsible for several functions; it controls the ESIS experiment, responds to timers and uplinks, acquires and stores image data from the cameras, downlinks a subset of images through telemetry, and provides experiment health and status. The DACS is housed with the rest of the avionics (power supply, analog signal conditioning system) in a 0.56-0.43 m transition section outside of the experiment section. This relaxes the thermal and cleanliness constraints placed on the avionics. Custom DC/DC converters are used for secondary voltages required by other electronic components. The use of custom designed converters allowed additional ripple filtering for low noise.

4.4.9 Pointing System

The imaging target will be selected prior to launch, the morning of the day of flight. During flight, pointing will be maintained by the Solar Pointing Attitude Rocket Control System (SPARCS) [Lockheed Missiles and Space Co. Report]. Images from Camera 1 will be downlinked and displayed in real time on the SPARCS control system console at intervals of ∼16 s to verify pointing is maintained during flight.

4.4.10 Mechanical

ESIS and MOSES are mounted on opposite sides of a composite optical table structure originally developed for the Solar Plasma Diagnostics Experiment rocket mission (SPDE, Bruner [1995]). The layered carbon fiber structure features a convenient, precisely coplanar array of threaded inserts with precision counterbores. The carbon fiber layup is designed to minimize the longitudinal coefficient of thermal expansion. The optical table is housed in two 0.56 m diameter skin sections, with a total length of 3 m. A ball joint and spindle assembly on one end and flexible metal aperture plate on the other hold the optical table in position inside the skin sections. The kinematic mounting system isolates the optical table from bending or twisting strain of the skins.

4.5 Mission Profile

ESIS will be launched aboard a sub-orbital Terrier Black Brant sounding rocket from White Sands Missile Range. The experiment is currently scheduled for launch in August, 2019. Trajectory will follow a roughly parabolic path, with >270 s solar observing time above 160 km. ESIS will begin continuously taking exposures at a fixed cadence immediately after launch, terminating just before the payload impacts the upper atmosphere. Exposure length will be determined by the target selected for launch day. Exposures taken while the payload shutter door is closed ($< 160\,\mathrm{km}$) will be used for dark calibration. Data will be stored on board and downloaded after recovery, however a limited amount of data will be transmitted to the ground station via high speed telemetry as a safeguard against payload loss or destruction. A parachute will slow the descent of the payload after it enters the atmosphere, and recovery will be accomplished by helicopter after the payload is located on the ground.

4.5.1 ESIS Mission Update

Since the time of writing ESIS launched and was recovered successfully from White Sands Missile Range on September 30, 2019. Unfortunately, due to failure of the mechanical shutter, no MOSES data was obtained during this flight. A paper is forthcoming that will document the ESIS instrument in its as-flown configuration [Courrier et al., 2020]. A companion paper will describe ESIS first results [Parker et al., 2020]. Two significant changes, one to the ESIS instrument and one to our alignment procedures, were made prior to launch and are summarized below.

The transfer from visible to EUV grating alignment was completed by an alternative means. The apparatus described by Johnson et al. [2018] was not able to maintain sufficient repeatability during test runs on diffraction grating surfaces. To maintain the launch schedule, a phase shifting interferometer was used to transfer the alignment of the visible gratings to the EUV flight gratings.

A trade study was conducted, and it was decided to remove the primary aperture stop. The advantage was an increase in sensitivity. The disadvantage was to sacrifice the unvignetted design described in section 4.4.6. The effective aperture is increased by a factor of 1.7 to 2.7 as a function of FOV in the radial dimension. The corresponding signal gradient is oriented along the dispersion direction of each channel; vignetting increases (and signal decreases) when moving towards blue wavelengths (*i.e.* moving to the left in Figure 4.4). This gradient is due almost entirely to vignetting by the central obscuration, and is linear across the entire FOV. The principal challenge is that the images cannot be corrected directly; rather, since the gradient is repeated for each of the overlapping spectral line images, the vignetting can only be accounted for by forward modeling. Since forward modeling is required for all of the inversion procedures under consideration for ESIS data analysis, the vignetting was deemed low risk to the mission science.

4.6 Conclusion and Outlook

ESIS is a next generation slitless spectrograph, designed to obtain co-temporal spectral and spatial images of the solar transition region and corona. In this report, we present details of the scientific objectives, instrument, image and spectral resolution, data acquisition, and flight profile.

ESIS follows on the proven MOSES design, incorporating several design changes to improve the utility of the instrument. The symmetrical arrangement of CCDs and diffraction gratings results in a compact instrument while increasing the number of dispersed images and dispersion planes. This aids the inversion process, while also allowing access to higher order spectral line profile moments. Individual gratings improve resolution by controlling aberration in each channel. The addition of a field stop eliminates spectral contamination and provides an easily recognizable edge for data inversion. The ESIS design also demonstrates that all this can be accomplished in a volume small enough to serve as a prototype for a future orbital instrument.

For the first flight, four of the six available ESIS channels will be populated with optics optimized around the O V emission line. The large ($11.3'$), high resolution FOV ($1.52''$, $74\,\text{m\AA}$) can simultaneously observe the evolution of small scale EUV flows and large scale MHD waves in high temporal cadence. ESIS also enables the study of transport of mass and energy in the transition region and corona during the ~ 5 minute data collection portion of rocket flight.

ESIS was recovered after a successful first launch on September 30, 2019, with analysis of collected data currently in-process. Subsequent flights will be proposed and the instrument refined with an eye toward orbital opportunities. Suborbital flights will allow us to expand the instrument to its full complement of six channels and refine our data analysis methods, but do not provide access to major flares and eruptive events that drive space weather. The long term prospect is that an ESIS-like instrument on an orbital platform could provide high cadence maps of spectral line profiles in solar flares, allowing unique and comprehensive observations of the dynamics in solar eruptive events, flare ribbons, and the flare reconnection region.

4.7 Acknowledgements

We gratefully acknowledge the support of the NASA Heliophysics Low-Cost Access to Space program, grant number NNX14AK71G.

CHAPTER FIVE

CONCLUSION

The solar atmosphere above the temperature minimum (chromosphere, transition region and corona) is characterized by a positive temperature gradient ($\frac{\partial T}{\partial r} > 0$, on average) and marked departure from the local thermodynamic equilibrium (LTE) of the solar interior and photosphere. A long standing goal in solar physics is to understand the non-thermal mechanisms by which mass and energy are transported from the relatively cool photosphere to the million degree solar corona. Dissipation of magnetic energy, through some combination of magnetohydrodynamic (MHD) waves and/or magnetic reconnection events may power the hot corona and solar wind [*e.g.* De Moortel and Browning, 2015, and references therein]. Emission from the solar atmosphere spans many VUV spectral lines that are observable only from space. Short-ward of 150 nm there is little continuum and the spectrum comprises well separated emission lines (well separated in the sense that the stronger lines can be isolated in ∼1–3 Å [Vernazza and Reeves, 1978]). Much of our knowledge of the TR in the past two decades has been gained from spectroscopic observations [*e.g.*, Wilhelm et al., 2004, Tian, 2017]. The review paper by Tian [2017] cites observations by *SOHO/SUMER* and *IRIS* as key in uncovering the role the transition region (TR) may play in transporting mass and energy to the corona and solar wind. These observations also show that rather than a stratified layer, the TR is tenuous, finely textured, and highly dynamic.

Investigations of the TR and surrounding atmosphere are limited by our observational capabilities. The TR phenomena of interest have complex structure and are extensive in two dimensions (or more accurately three dimensions considering the line of sight). Spectroscopy allows direct access to the mechanics of the TR through analysis of spectral line shifts, or better yet, resolving the entire line profile. Diffraction gratings are the only technology available to resolve VUV spectral lines; the materials do not exist to create a Fabry-Pèrot etalon shortward of ≈100 nm [*e.g.*, Wuelser et al., 2000], and Multi-layer mirror coatings cannot achieve a narrow enough pass band to isolate a single emission line (*e.g.* Fig. 4.6). Therefore, the usual design for VUV solar spectroscopy is a slit spectrograph. However, the 1D field of view of these instruments makes it difficult to capture the spatial *and* temporal variability of the TR.

In chapters 2, 3 and 4 of this thesis, I presented three investigations that advance the state of the art in imaging spectroscopy of the solar atmosphere in VUV wavelengths. This advancement is achieved through slitless, multi-order spectroscopy in Chapters 2 and 4 as a new technology to image the TR. Chapter 3 focuses on improving *IRIS* observations through characterization of the instrument PSF. In this chapter, I summarize the objectives of each project, and assesses its value to the scientific community. I will also describe how each study leads to further questions, and suggest how those questions may be answered in the future.

5.1 MOSES Doppler Inversion

In Chapter 2 [Courrier and Kankelborg, 2018] I presented a method to infer Doppler shifts from MOSES data. MOSES is a slitless spectrograph, imaging with three detectors placed at the $m = -1, 0$, and $+1$ orders of a diffraction grating, allowing it to overcome the spatial and temporal limitations associated with slit spectroscopy. The data MOSES collects are co-temporal over a large FOV. The disadvantage of this configuration is that the data obtained are an overlapping series of images from the bright emission lines in the instrument passband (He II 304Å and

Si XI 303Å). Disentangling this overlapping information is ill posed [Kankelborg and Thomas, 2001]. A full "inversion" of MOSES data is analogous to a tomographic three-projection inversion. Fox [2011] and Rust [2017] have performed separate inversions of select features in MOSES He II data using variations of the multiplicative algebraic reconstruction technique (MART) developed by Gordon et al. [1970].

Rather than perform a full inversion of select features, I sought to obtain only Doppler shifts over the entire MOSES dataset. The automated method I developed measures the perceived displacement of individual features between pairs of MOSES image orders using local correlation tracking (LCT). The displacements directly correspond to He II line shifts in the 2006 February MOSES data. This is not an optically thin line, so radiative transfer effects may broaden the profile [*e.g.* Jordan, 1975]. Nevertheless, I assume that the LCT derived displacements correspond to bulk flows along the line-of-sight (LOS). These flows may indicate energy release, as in explosive events [Fox et al., 2010, Rust, 2017], mass supply to the corona [Tian et al., 2008, Brannon et al., 2015], or cooling material in flare loops [Brannon, 2016].

The LCT based method is sensitive to Doppler shifts of the He II line profile, but not higher order line moments (*e.g.* line width). The trade-off in recovering only a subset of the available spectral information is the problem becomes better posed compared to the full inversions mentioned previously. This may make the LCT based method more robust when faced with a crowded and/or complicated field. For example, LCT is insensitive to image background, which must be carefully treated in MART based inversions [Fox, 2011, Rust, 2017]. Also, the 2D nature of the correlation provides a degree of freedom orthogonal to the dispersion axis, so that the LCT method can accommodate differing PSFs in each of the three image orders.

Since the transition region is finely structured, it is desirable to resolve Doppler shifts at the smallest spatial scales possible. For the method developed in Chapter 2, the Doppler map spatial resolution is limited by correlation window size. Tests with synthetic data showed that the minimum useful window is of the same scale as the instrument PSF (≈ 3 pixels). This makes the resolution of the derived Doppler maps similar to that of the original intensity images.

The LCT based method yields similar results for Doppler shifts compared to inversion for the full spectrum. Fox et al. [2010] identified and analyzed a single explosive event (EE) in MOSES He II 304 Å data. In that study, the EE was background subtracted by hand, then fitted with Gaussian profiles row-by-row, with human supervision of the fitting process. The automated LCT method is more efficient; Doppler shift estimates for each pixel in the entire MOSES He II data set (30 exposures, $2048\,x\,1024$ pixels each) were obtained in only a few minutes.

5.1.1 Future Directions for LCT Doppler Maps

While I was successful in deriving Doppler shifts from MOSES data, analysis of both this and synthetic data identified areas that could be improved with future work. The two critical concerns are PSF effects and LCT displacement offset.

Systematic errors arise from the differing PSFs of each image order. Compact, isolated features in MOSES data are dominated by the instrument PSF, the shape of which varies in each image order. The regions where these PSFs do not overlap, or are not “well-aligned” between image orders are falsely interpreted by the LCT method as displacements. The result is underestimation if the mis-alignment is opposed to the true Doppler shift direction, and overestimation if it is directed along the true shift. The false Doppler signatures can have magnitudes of tens of $\mathrm{km\,s^{-1}}$ and often appear as bi-polar jet structures in features where the true Doppler signal is weak [Fox, 2011, Rust, 2017].

Deconvolution offers one possible method of removing the PSF artifacts. Like inversion, deconvolution of a known PSF is an ill-posed problem, the outcome of which may vary greatly depending on the form of the PSF chosen. In Chapter 2 the PSF estimates I used were sufficient to illustrate the expected error that arises from their differing shapes. A more refined estimate of the MOSES PSFs was made by Rust [2017]. The new versions were inferred from unresolved features in the 08 February 2006 data, that were isolated by a partial wavelet reconstruction technique. Deconvolution of these PSFs from the MOSES data could greatly reduce the appearance of spatial PSF effects in the LCT inversion. Note, however, that Rust showed the MOSES PSFs tend to change with time during flight.

An alternate form of correction is PSF equalization. A recent study, completed just after the publication of Chapter 2, filters images from each of the three MOSES orders so that they all share one “equalized” PSF [Atwood and Kankelborg, 2018]. Unlike known PSF deconvolution, the filtering does not sharpen (or for that matter, smooth) the images. However, a filter to equalize the PSFs is a better posed problem than deconvolution. Atwood and Kankelborg [2018] showed that false bi-polar PSF artifacts were significantly reduced in MOSES images, while features larger than the equalized image PSF retained their spectral characteristics. Applying this filtering before the the LCT inversion could potentially eliminate dissimilar PSF shape as a source of error without affecting the spatial resolution of the Doppler maps.

Another systematic error arises from “displacement offset” inherent to the LCT technique used to perform the inversions. LCT correlates sub-regions of two images to find a local displacement between the pair [November and Simon, 1988]. The Fourier method I employed defines the sub-regions of each image with a Gaussian windowing function, centered at the same pixel location in each image [Fisher and Welsch, 2008]. Correlations can therefore only be drawn for the portions of features that are contained in both sub-regions. Since the correlation is best when the window straddles the corresponding copies of the feature in both images, this results in an offset of the perceived position of the derived displacement vectors. The magnitude of the offset equals one-half the magnitude of displacement between the two images. This formulation of LCT makes sense for its originally intended purpose, but is problematic for inversion of MOSES data. Fortunately, the symmetric positioning of the two outboard image orders avoided this effect, so that the offset displacement vectors tended to fall over the correct positions on the Sun. This form of correction is not possible for the first flight of ESIS, as none of the four dispersion orders will be oppositely positioned. To reduce this systematic error in ESIS inversions, it may be desirable to develop a more suitable algorithm for comparing asymmetric pairs of diffraction orders.

5.2 PSFs for *IRIS*

In Chapter 3 [Courrier et al., in press], I determined on-orbit spatial PSFs for the NUV and FUV channels of the *IRIS* spectrograph from a Mercury transit of the Sun. This is the first PSF characterization of the *IRIS* spectrograph since its launch in 2014. I found that the NUV channel PSF estimates contain more energy in the scattering wings, and wider cores when compared to models that include only pixel size and diffraction. In the FUV channels, the PSF estimates are comparable to the models. Modulation transfer functions derived from the PSF estimates show that the spectrograph can achieve a spatial resolution of 2.47 cycles/arcsec in the NUV channel near 2796 Å and 2.55 cycles/arcsec near 2814 Å. In the short (≈1336 Å) and long (≈1394 Å) wavelength FUV channels, the MTFs show pixel limited resolution (3.0 cycles/arcsec)

Deconvolution of the estimated PSFs improves some aspects the observed spectra. PSF effects are more obvious in the NUV channel than the FUV channel.

This is because the broad core of the NUV PSF estimates reduces fine scale resolution, especially noticeable in compact bright (relative to background) isolated features. Doppler shifts and other line profile metrics are also attenuated because adjacent spectra are blurred together. When comparing spectra, deconvolution increased the observed peak intensity by 3% and velocity by 22% when derived from Mg II (NUV) line profiles of a single isolated explosive event (EE). The core of the FUV PSFs estimates are not broadened, so deconvolution of the FUV EE spectra produces more subtle results. In this channel, the equivalent width of the EE line profile is reduced by only 0.02 Å.

Deconvolution also reduces scattered light in the NUV spectra, improving contrast at all scales. In the Mercury transit data, scattered light is visible as non-zero intensity deep within Mercury's shadow. After deconvolution this 'residual' intensity is reduced to a small fraction of a DN in the NUV channel.

In summary, the accuracy of spectral observables (*e.g.*, Doppler shifts, line widths, and line ratios) depends on resolving the structure(s) in which they occur. Deconvolution using the PSF estimates derived in Chapter 3 will allow the scientific community to perform these measurements at the best possible resolution for IRIS. The results of Chapter 3 are made available through a SolarSoft module [Freeland and Handy, 1998]. The routine `iris_sg_deconvolve.pro` implements either a Richardson-Lucy or FFT deconvolution of *IRIS* spectra along the spatial axis. It also includes a pointer to the file that contains the PSF estimates in the *IRIS* SolarSoft distribution.

5.2.1 Future Directions for *IRIS* PSF Characterization

In the comparison of the NUV and FUV PSF estimates in Chapter 3, I cautioned that the FUV transit data is of lesser quality and quantity than the NUV. An exposure-to-exposure fluctuation in camera pedestal was observed in both FUV channels that influenced the results of the PSF analysis. Signal in the FUV channels was also comparatively lower than that in the NUV. Both of these issues were exacerbated by the short exposure lengths required to minimize motion blur (up to approximately a half pixel of blurring can be expected over 15 s), so that the FUV PSF estimates are considerably noisier than their NUV counterparts. Since the *IRIS* resolution is effectively limited by the noise floor of the instrument, noise gating the Mercury spectra could lead to an improvement in the quality of both the FUV and NUV PSF estimates.

Finally, the PSF characterization focused only on the spectrograph spatial resolution. *IRIS* also observed the Mercury transit in all slit-jaw imager channels. The method I developed could be generalized to two dimensions, so that 2D spatial PSFs could be estimated for the slit-jaw imager from the Mercury transit.

5.3 ESIS

Chapter 4 [Courrier et al., 2020] describes a new instrument, the EUV Snapshot Imaging Spectrograph (ESIS). Since the time of writing in Chapter 4, ESIS has been recovered from a successful launch on September 30, 2019. Unfortunately, due to failure of the mechanical shutter, no MOSES data was obtained during this flight. Like MOSES, ESIS is a slitless spectrograph, combining imaging and spectroscopy to address the observational challenges of the finely structured and highly dynamic solar transition region. The ESIS and MOSES instruments fly together on the same payload, each observing distinct temperature regions in the TR. The passband of each instrument is narrow enough to encompass only a few bright spectral lines (MOSES: Ne VII, ESIS: O V and Mg X). Both instruments collect co-temporal spatial and spectral information over a large FOV (MOSES: $20' \times 10'$, ESIS: $11'$ octagonal) at high-cadence (minimum ≈4 s) observing distinct temperature regions in the TR.

While the instruments share similar objectives, the design of ESIS is significantly different. This is a direct result of experience gained from MOSES. The new design reduces (and in some cases, removes altogether) many of the instrumental artifacts and limitations that affect MOSES inversions. The ESIS optics are based on a Gregorian telescope layout, with the multiple projections rotationally symmetric about the optical axis (*e.g.* Fig. 4.2). A field stop is placed at the intermediate focus of the parabolic primary mirror. This eliminates contamination of the spectra from sources outside the FOV, such as that observed by Parker and Kankelborg [2016] in MOSES data. The secondary mirror is replaced by a segmented array of identical spherical variable line space (SVLS) gratings. Each grating produces only one projection, compared to three projections by the single MOSES grating. This allows optimization of the SVLS grating for a single spectral order. The modeled PSF of an ESIS image projection is not rotationally invariant, but is small enough to be mostly contained in a single pixel. This significantly reduces systematic errors due to PSF shape in the inversion method described in Chapter 2. The design of ESIS is also more compact than MOSES, so that more projections and projection planes can be accommodated. MOSES has three projections arrayed along a single plane. The initial flight of ESIS was populated with four projections (of a maximum of six), each of which occupies a different projection plane. The placement of the ESIS projections not only increases the number of "look angles" available for tomographic reconstruction, but also expands the space occupied by the projections to three dimensions instead of the two dimensional plane occupied by MOSES. The additional dimension reduces the extent of the null space (spatial-spectral structures to which the instrument has zero response, *e.g.* [Kankelborg and Thomas, 2001]) of ESIS compared to MOSES. This in turn results in less inherent ambiguity in the inversion problem posed by ESIS than that of MOSES.

5.3.1 ESIS Objectives

A primary science objective of ESIS is to study magnetic reconnection in the TR by observing multiple explosive events (EEs). These extremely common events appear to be closely associated with magnetic reconnection in the solar atmosphere, however, their exact nature and morphology remains elusive. The MOSES instrument analyzed previously unobserved structure and morphology in He II transition region explosive events [Fox et al., 2003, Rust, 2017]. ESIS also observed multiple EEs and ongoing analysis will map line profiles over the full extent of each event, improving upon and extending the characterization of TR EEs first begun by MOSES.

ESIS data will also allow investigation of energy transport in the TR and corona. Alfvén waves can carry sufficient energy to power the fast solar wind [De Pontieu et al., 2007, McIntosh et al., 2011], presenting a mechanism by which mass and energy may be transported to the hot solar corona. The motions of these waves are detectable to ESIS through the non-thermal broadening of optically thin spectral lines in the instrument passband. The concentration of non-thermal energy observed by ESIS serves as an indicator of Alfvén wave source density in the sky-plane. In a similar manner, comparison of Doppler maps from ESIS and MOSES can indicate whether Alfvén waves originate in the chromosphere or below (*i.e.* along the line-of-sight). Thus, ESIS (and MOSES) can detect and localize MHD waves and their origins in the three spatial dimensions of the solar atmosphere.

REFERENCES CITED

S. Akiyama, G. A. Doschek, and J. T. Mariska. Nonthermal Velocities in Different Temperature Regions of the Solar Lower Transition Region. *ApJ*, 623(1):540–550, Apr 2005. doi: 10.1086/428638.

H. Alfvén. Existence of Electromagnetic-Hydrodynamic Waves. *Nature*, 150:405–406, Oct. 1942. doi: 10.1038/150405d0.

V. Angelopoulos, J. P. McFadden, D. Larson, C. W. Carlson, S. B. Mende, H. Frey, T. Phan, D. G. Sibeck, K.-H. Glassmeier, U. Auster, E. Donovan, I. R. Mann, I. J. Rae, C. T. Russell, A. Runov, X.-Z. Zhou, and L. Kepko. Tail Reconnection Triggering Substorm Onset. *Science*, 321:931, Aug. 2008. doi: 10.1126/science.1160495.

P. Antolin and L. Rouppe van der Voort. Observing the Fine Structure of Loops through High-resolution Spectroscopic Observations of Coronal Rain with the CRISP Instrument at the Swedish Solar Telescope. *ApJ*, 745:152, Feb. 2012. doi: 10.1088/0004-637X/745/2/152.

S. Atwood and C. Kankelborg. Blind technique for point spread function equalization with application to the Multi-Order Solar Extreme Ultraviolet Spectrograph. *Journal of Astronomical Telescopes, Instruments, and Systems*, 4(2):028002, Apr. 2018. doi: 10.1117/1.JATIS.4.2.028002.

G. R. Ayers and J. C. Dainty. Iterative blind deconvolution method and its applications. *Opt. Lett.*, 13(7):547–549, Jul 1988. doi: 10.1364/OL.13.000547. URL `http://ol.osa.org/abstract.cfm?URI=ol-13-7-547`.

D. Banerjee, D. Pérez-Suárez, and J. G. Doyle. Signatures of Alfvén waves in the polar coronal holes as seen by EIS/Hinode. *A&A*, 501:L15–L18, July 2009. doi: 10.1051/0004-6361/200912242.

W. A. Baum, F. S. Johnson, J. J. Oberly, C. C. Rockwood, C. V. Strain, and R. Tousey. Solar Ultraviolet Spectrum to 88 Kilometers. *Physical Review*, 70: 781–782, Nov. 1946. doi: 10.1103/PhysRev.70.781.

T. E. Berger, C. J. Schrijver, R. A. Shine, T. D. Tarbell, A. M. Title, and G. Scharmer. New Observations of Subarcsecond Photospheric Bright Points. *ApJ*, 454:531, Nov. 1995. doi: 10.1086/176504.

M. Bertero, P. Boccacci, G. Desiderá, and G. Vicidomini. Image deblurring with Poisson data: from cells to galaxies. *Inverse Problems*, 25(12):123006, 2009.

A. Bhattacharjee, Y.-M. Huang, H. Yang, and B. Rogers. Fast reconnection in high-Lundquist-number plasmas due to the plasmoid Instability. *Physics of Plasmas*, 16(11):112102, Nov. 2009. doi: 10.1063/1.3264103.

R. M. Bonnet, M. Decaudin, E. C. Bruner, Jr., L. W. Acton, and W. A. Brown. High-resolution Lyman-alpha filtergrams of the sun. *ApJ*, 237:L47–L50, Apr. 1980. doi: 10.1086/183232.

S. R. Brannon. Observation and Analysis of Ballistic Downflows in an M-class Flare with the Interface Region Imaging Spectrograph. *ApJ*, 833:101, Dec. 2016. doi: 10.3847/1538-4357/833/1/101.

S. R. Brannon, D. W. Longcope, and J. Qiu. Spectroscopic Observations of an Evolving Flare Ribbon Substructure Suggesting Origin in Current Sheet Waves. *ApJ*, 810:4, Sept. 2015. doi: 10.1088/0004-637X/810/1/4.

J. W. Brosius and A. N. Daw. Quasi-periodic Fluctuations and Chromospheric Evaporation in a Solar Flare Ribbon Observed by IRIS. *ApJ*, 810(1):45, Sep 2015. doi: 10.1088/0004-637X/810/1/45.

J. W. Brosius, D. M. Rabin, and R. J. Thomas. Doppler Velocities Measured in Coronal Emission Lines from a Bright Point Observed with the EUNIS Sounding Rocket. *ApJ*, 656:L41–L44, Feb. 2007. doi: 10.1086/512185.

J. W. Brosius, A. N. Daw, and D. M. Rabin. Pervasive Faint Fe XIX Emission from a Solar Active Region Observed with EUNIS-13: Evidence for Nanoflare Heating. *ApJ*, 790:112, Aug. 2014. doi: 10.1088/0004-637X/790/2/112.

G. E. Brueckner and J.-D. F. Bartoe. Observations of high-energy jets in the corona above the quiet sun, the heating of the corona, and the acceleration of the solar wind. *ApJ*, 272:329–348, Sept. 1983. doi: 10.1086/161297.

M. E. Bruner. SPDE: Solar Plasma Diagnostic Experiment. Technical Report Contract NAS5-32147, Lockheed Martin Palo Alto Research Lab., Palo Alto, CA., Sept. 1995.

F. V. Bulygin, G. N. Vishnyakov, G. G. Levin, and D. V. Karpukhin. Spectrotomography–a new method of obtaining spectrograms of 2-D objects. *Optics and Spectroscopy*, 71:561–563, Dec. 1991.

J. Christensen-Dalsgaard, W. Dappen, S. V. Ajukov, E. R. Anderson, H. M. Antia, S. Basu, V. A. Baturin, G. Berthomieu, B. Chaboyer, S. M. Chitre, A. N. Cox, P. Demarque, J. Donatowicz, W. A. Dziembowski, M. Gabriel, D. O. Gough, D. B. Guenther, J. A. Guzik, J. W. Harvey, F. Hill, G. Houdek, C. A. Iglesias, A. G. Kosovichev, J. W. Leibacher, P. Morel, C. R. Proffitt, J. Provost, J. Reiter, J. Rhodes, E. J., F. J. Rogers, I. W. Roxburgh, M. J. Thompson, and R. K. Ulrich. The Current State of Solar Modeling. *Science*, 272(5266):1286–1292, May 1996. doi: 10.1126/science.272.5266.1286.

J. W. Cook, F. P. Keenan, P. L. Dufton, A. E. Kingston, A. K. Pradhan, H. L. Zhang, J. G. Doyle, and M. A. Hayes. The O IV and S IV intercombination lines in solar and stellar ultraviolet spectra. *ApJ*, 444:936–942, May 1995. doi: 10.1086/175664.

H. Courrier, C. Kankelborg, B. De Pontieu, and J.-P. Wülser. An on orbit determination of point spread functions for the Interface Region Imaging Spectrograph. *Sol. Phys.*, in press.

H. T. Courrier and C. C. Kankelborg. Using local correlation tracking to recover solar spectral information from a slitless spectrograph. *J. Atmos. Tel. & Img. Sys.*, 4 (1):018001, Jan. 2018. doi: 10.1117/1.JATIS.4.1.018001.

H. T. Courrier, C. C. Kankelborg, A. Winebarger, K. Kobayashi, B. Beabout, D. Beabout, B. Carroll, J. Cirtain, J. A. Duffy, C. Gomez, E. Gullikson, M. Johnson, J. Parker, L. Rachmeler, R. T. Smart, L. Springer, and D. L. Windt. The EUV Snapshot Imaging Spectrograph (ESIS). In preparation, 2020.

S. R. Cranmer and A. A. van Ballegooijen. On the Generation, Propagation, and Reflection of Alfvén Waves from the Solar Photosphere to the Distant Heliosphere. *ApJS*, 156:265–293, Feb. 2005. doi: 10.1086/426507.

J. L. Culhane, L. K. Harra, A. M. James, K. Al-Janabi, L. J. Bradley, R. A. Chaudry, K. Rees, J. A. Tandy, P. Thomas, M. C. R. Whillock, B. Winter, G. A. Doschek, C. M. Korendyke, C. M. Brown, S. Myers, J. Mariska, J. Seely, J. Lang, B. J. Kent, B. M. Shaughnessy, P. R. Young, G. M. Simnett, C. M. Castelli, S. Mahmoud, H. Mapson-Menard, B. J. Probyn, R. J. Thomas, J. Davila, K. Dere, D. Windt, J. Shea, R. Hagood, R. Moye, H. Hara, T. Watanabe, K. Matsuzaki, T. Kosugi, V. Hansteen, and Ø. Wikstol. The EUV Imaging Spectrometer for Hinode. *Sol. Phys.*, 243:19–61, June 2007. doi: 10.1007/s01007-007-0293-1.

A. Czaykowska, B. De Pontieu, D. Alexander, and G. Rank. Evidence for Chromospheric Evaporation in the Late Gradual Flare Phase from SOHO/CDS Observations. *ApJ*, 521(1):L75–L78, Aug 1999. doi: 10.1086/312176.

I. De Moortel and P. Browning. Recent advances in coronal heating. *Philosophical Transactions of the Royal Society of London Series A*, 373:20140269–20140269, Apr. 2015. doi: 10.1098/rsta.2014.0269.

B. De Pontieu, S. W. McIntosh, M. Carlsson, V. H. Hansteen, T. D. Tarbell, C. J. Schrijver, A. M. Title, R. A. Shine, S. Tsuneta, Y. Katsukawa, K. Ichimoto, Y. Suematsu, T. Shimizu, and S. Nagata. Chromospheric Alfvénic Waves Strong Enough to Power the Solar Wind. *Science*, 318:1574, Dec. 2007. doi: 10.1126/science.1151747.

B. De Pontieu, A. M. Title, J. R. Lemen, G. D. Kushner, D. J. Akin, B. Allard, T. Berger, P. Boerner, M. Cheung, C. Chou, J. F. Drake, D. W. Duncan,

S. Freeland, G. F. Heyman, C. Hoffman, N. E. Hurlburt, R. W. Lindgren, D. Mathur, R. Rehse, D. Sabolish, R. Seguin, C. J. Schrijver, T. D. Tarbell, J.-P. Wülser, C. J. Wolfson, C. Yanari, J. Mudge, N. Nguyen-Phuc, R. Timmons, R. van Bezooijen, I. Weingrod, R. Brookner, G. Butcher, B. Dougherty, J. Eder, V. Knagenhjelm, S. Larsen, D. Mansir, L. Phan, P. Boyle, P. N. Cheimets, E. E. DeLuca, L. Golub, R. Gates, E. Hertz, S. McKillop, S. Park, T. Perry, W. A. Podgorski, K. Reeves, S. Saar, P. Testa, H. Tian, M. Weber, C. Dunn, S. Eccles, S. A. Jaeggli, C. C. Kankelborg, K. Mashburn, N. Pust, L. Springer, R. Carvalho, L. Kleint, J. Marmie, E. Mazmanian, T. M. D. Pereira, S. Sawyer, J. Strong, S. P. Worden, M. Carlsson, V. H. Hansteen, J. Leenaarts, M. Wiesmann, J. Aloise, K.-C. Chu, R. I. Bush, P. H. Scherrer, P. Brekke, J. Martinez-Sykora, B. W. Lites, S. W. McIntosh, H. Uitenbroek, T. J. Okamoto, M. A. Gummin, G. Auker, P. Jerram, P. Pool, and N. Waltham. The Interface Region Imaging Spectrograph (IRIS). *Sol. Phys.*, 289:2733–2779, July 2014. doi: 10.1007/s11207-014-0485-y.

B. De Pontieu, S. McIntosh, J. Martinez-Sykora, H. Peter, and T. M. D. Pereira. Why is Non-Thermal Line Broadening of Spectral Lines in the Lower Transition Region of the Sun Independent of Spatial Resolution? *ApJ*, 799:L12, Jan. 2015. doi: 10.1088/2041-8205/799/1/L12.

C. DeForest, D. F. Elmore, M. P. Bradford, J. Elrod, and D. L. Gilliam. Stereoscopic Spectroscopy for Efficient Spectral Imaging and Magnetography. *ApJ*, 616:600–616, Nov. 2004. doi: 10.1086/424745.

C. E. DeForest, P. C. H. Martens, and M. J. Wills-Davey. Solar Coronal Structure and Stray Light in TRACE. *ApJ*, 690:1264–1271, Jan. 2009. doi: 10.1088/0004-637X/690/2/1264.

G. Del Zanna and H. E. Mason. Solar UV and X-ray spectral diagnostics. *Living Reviews in Solar Physics*, 15(1):5, Aug 2018. doi: 10.1007/s41116-018-0015-3.

K. P. Dere. Explosive events, magnetic reconnection, and coronal heating. *Advances in Space Research*, 14:13–, Apr. 1994. doi: 10.1016/0273-1177(94)90154-6.

K. P. Dere, J.-D. F. Bartoe, and G. E. Brueckner. High-resolution telescope and spectrograph observations of the quiet solar chromosphere and transition zone. *ApJ*, 281:870–883, June 1984. doi: 10.1086/162167.

K. P. Dere, J.-D. F. Bartoe, and G. E. Brueckner. Explosive events in the solar transition zone. *Sol. Phys.*, 123:41–68, Mar. 1989. doi: 10.1007/BF00150011.

K. P. Dere, J. Bartoe, G. E. Brueckner, J. Ewing, and P. Lund. Explosive events and magnetic reconnection in the solar atmosphere. *J. Geophys. Res.*, 96:9399–9407, June 1991. doi: 10.1029/90JA02572.

M. Descour and E. Dereniak. Computed-tomography imaging spectrometer: experimental calibration and reconstruction results. *Appl. Opt.*, 34(22):4817–4826, Aug 1995. doi: 10.1364/AO.34.004817. URL `http://ao.osa.org/abstract.cfm?URI=ao-34-22-4817`.

M. R. Descour, C. E. Volin, E. L. Dereniak, T. M. Gleeson, M. F. Hopkins, D. W. Wilson, and P. D. Maker. Demonstration of a computed-tomography imaging spectrometer using acomputer-generated hologram disperser. *Appl. Opt.*, 36(16): 3694–3698, Jun 1997. doi: 10.1364/AO.36.003694. URL `http://ao.osa.org/abstract.cfm?URI=ao-36-16-3694`.

L. Dolla and J. Solomon. Solar off-limb line widths: Alfvén waves, ion-cyclotron waves, and preferential heating. *A&A*, 483:271–283, May 2008. doi: 10.1051/0004-6361:20077903.

G. A. Doschek, U. Feldman, and K. P. Dere. Electron densities in solar flares from line ratios of Ca XVII. *A&A*, 60(2):L11–L13, Sep 1977.

J. G. Doyle, D. Banerjee, and M. E. Perez. Coronal line-width variations. *Sol. Phys.*, 181:91–101, July 1998. doi: 10.1023/A:1005019931323.

J. Dudík, V. Polito, E. Dzifčáková, G. Del Zanna, and P. Testa. Non-Maxwellian Analysis of the Transition-region Line Profiles Observed by the Interface Region Imaging Spectrograph. *ApJ*, 842(1):19, Jun 2017. doi: 10.3847/1538-4357/aa71a8.

U. Feldman, G. A. Doschek, and K. G. Widing. Electron densities in solar flare and active region plasmas from a density-sensitive line ratio of Fe IX. *ApJ*, 219:304–306, Jan 1978. doi: 10.1086/155778.

U. Feldman, G. A. Doschek, and J. F. Seely. New identifications of Fe XVII spectral lines in solar flares. *MNRAS*, 212:41P–45P, Feb. 1985. doi: 10.1093/mnras/212.1.41P.

D. A. Fish, A. M. Brinicombe, E. R. Pike, and J. G. Walker. Blind deconvolution by means of the Richardson-Lucy algorithm. *J. Opt. Soc. Am. A*, 12(1):58–65, Jan 1995. doi: 10.1364/JOSAA.12.000058.

G. H. Fisher and B. T. Welsch. FLCT: A Fast, Efficient Method for Performing Local Correlation Tracking. In R. Howe, R. W. Komm, K. S. Balasubramaniam, and G. J. D. Petrie, editors, *Subsurface and Atmospheric Influences on Solar Activity*, volume 383 of *Astronomical Society of the Pacific Conference Series*, page 373, 2008.

J. L. Fox. *Snapshot imaging spectroscopy of the solar transition region: The Multi-Order Solar EUV Spectrograph (MOSES) sounding rocket mission.* PhD thesis, Montana State University, 2011.

J. L. Fox, C. C. Kankelborg, and T. R. Metcalf. Data inversion for the multi-order solar extreme-ultraviolet spectrograph. In A. M. Larar, J. A. Shaw, and Z. Sun, editors, *Optical Spectroscopic Techniques and Instrumentation for Atmospheric and Space Research V.*, volume 5157, pages 124–132. Proc. SPIE, November 2003.

J. L. Fox, C. C. Kankelborg, and R. J. Thomas. A Transition Region Explosive Event Observed in He II with the MOSES Sounding Rocket. *ApJ*, 719:1132–1143, Aug. 2010. doi: 10.1088/0004-637X/719/2/1132.

M. S. Freed, D. E. McKenzie, D. W. Longcope, and M. Wilburn. Analysis of Flows inside Quiescent Prominences as Captured by Hinode/Solar Optical Telescope. *ApJ*, 818(1):57, Feb 2016. doi: 10.3847/0004-637X/818/1/57.

S. L. Freeland and B. N. Handy. Data Analysis with the SolarSoft System. *Sol. Phys.*, 182:497–500, Oct. 1998. doi: 10.1023/A:1005038224881.

L. Golub, M. Herant, K. Kalata, I. Lovas, G. Nystrom, F. Pardo, E. Spiller, and J. Wilczynski. Sub-arcsecond observations of the solar X-ray corona. *Nature*, 344: 842–844, Apr. 1990. doi: 10.1038/344842a0.

L. Golub, J. Bookbinder, E. Deluca, M. Karovska, H. Warren, C. J. Schrijver, R. Shine, T. Tarbell, A. Title, J. Wolfson, B. Handy, and C. Kankelborg. A new view of the solar corona from the transition region and coronal explorer (TRACE). *Physics of Plasmas*, 6:2205–2216, May 1999. doi: 10.1063/1.873473.

J. W. Goodman. *Introduction to Fourier Optics*. Roberts & Company, Engelwood, CO, 3rd edition, 2005.

R. Gordon, R. Bender, and G. T. Herman. Algebraic reconstruction techniques (art) for three-dimensional electron microscopy and x-ray photography. *J. Theor. Bio.*, 29(3):471 – 481, 1970. ISSN 0022-5193. doi: https://doi.org/10.1016/0022-5193(70)90109-8. URL `http://www.sciencedirect.com/science/article/pii/0022519370901098`.

B. V. Gudiksen, M. Carlsson, V. H. Hansteen, W. Hayek, J. Leenaarts, and J. Martínez-Sykora. The stellar atmosphere simulation code Bifrost. Code description and validation. *A&A*, 531:A154, July 2011. doi: 10.1051/0004-6361/201116520.

N. Hagen and E. L. Dereniak. Analysis of computed tomographic imaging spectrometers. I. Spatial and spectral resolution. *Appl. Opt.*, 47(28):F85–F95, Oct 2008. doi: 10.1364/AO.47.000F85. URL `http://ao.osa.org/abstract.cfm?URI=ao-47-28-F85`.

M. Hahn and D. W. Savin. Observational Quantification of the Energy Dissipated by Alfvén Waves in a Polar Coronal Hole: Evidence that Waves Drive the Fast Solar Wind. *ApJ*, 776:78, Oct. 2013. doi: 10.1088/0004-637X/776/2/78.

M. Hahn, E. Landi, and D. W. Savin. Evidence of Wave Damping at Low Heights in a Polar Coronal Hole. *ApJ*, 753:36, July 2012. doi: 10.1088/0004-637X/753/1/36.

G. E. Hale. On the Probable Existence of a Magnetic Field in Sun-Spots. *ApJ*, 28: 315, Nov. 1908. doi: 10.1086/141602.

G. E. Hale, F. Ellerman, S. B. Nicholson, and A. H. Joy. The Magnetic Polarity of Sun-Spots. *ApJ*, 49:153, Apr. 1919. doi: 10.1086/142452.

B. N. Handy, L. W. Acton, C. C. Kankelborg, C. J. Wolfson, D. J. Akin, M. E. Bruner, R. Caravalho, R. C. Catura, R. Chevalier, D. W. Duncan, C. G. Edwards, C. N. Feinstein, S. L. Freeland, F. M. Friedlaender, C. H. Hoffmann, N. E. Hurlburt, B. K. Jurcevich, N. L. Katz, G. A. Kelly, J. R. Lemen, M. Levay, R. W. Lindgren, D. P. Mathur, S. B. Meyer, S. J. Morrison, M. D. Morrison, R. W. Nightingale, T. P. Pope, R. A. Rehse, C. J. Schrijver, R. A. Shine, L. Shing, K. T. Strong, T. D. Tarbell, A. M. Title, D. D. Torgerson, L. Golub, J. A. Bookbinder, D. Caldwell, P. N. Cheimets, W. N. Davis, E. E. Deluca, R. A. McMullen, H. P. Warren, D. Amato, R. Fisher, H. Maldonado, and C. Parkinson. The transition region and coronal explorer. *Sol. Phys.*, 187:229–260, July 1999. doi: 10.1023/A:1005166902804.

H. Hara, T. Watanabe, L. K. Harra, J. L. Culhane, and P. R. Young. Plasma Motions and Heating by Magnetic Reconnection in a 2007 May 19 Flare. *ApJ*, 741:107, Nov. 2011. doi: 10.1088/0004-637X/741/2/107.

R. A. Harrison, E. C. Sawyer, M. K. Carter, A. M. Cruise, R. M. Cutler, A. Fludra, R. W. Hayes, B. J. Kent, J. Lang, D. J. Parker, J. Payne, C. D. Pike, S. C. Peskett, A. G. Richards, J. L. Gulhane, K. Norman, A. A. Breeveld, E. R. Breeveld, K. F. Al Janabi, A. J. McCalden, J. H. Parkinson, D. G. Self, P. D. Thomas, A. I. Poland, R. J. Thomas, W. T. Thompson, O. Kjeldseth-Moe, P. Brekke, J. Karud, P. Maltby, B. Aschenbach, H. Bräuninger, M. Kühne, J. Hollandt, O. H. W. Siegmund, M. C. E. Huber, A. H. Gabriel, H. E. Mason, and B. J. I. Bromage. The Coronal Diagnostic Spectrometer for the Solar and Heliospheric Observatory. *Sol. Phys.*, 162:233–290, Dec. 1995. doi: 10.1007/BF00733431.

E. Hecht. *Optics*. Addison-Wesley Pub. Co., Reading, Mass., 2nd ed.. edition, 1987. ISBN 020111609X.

B. L. Henke, E. M. Gullikson, and J. C. Davis. X-Ray Interactions: Photoabsorption, Scattering, Transmission, and Reflection at E = 50-30,000 eV, Z = 1-92. *Atomic Data and Nuclear Data Tables*, 54:181–342, July 1993. doi: 10.1006/adnd.1993.1013.

T. J. Holmes. Blind deconvolution of quantum-limited incoherent imagery: maximum-likelihood approach. *Journal of the Optical Society of America A*, 9: 1052–1061, July 1992. doi: 10.1364/JOSAA.9.001052.

Z. Huang, M. S. Madjarska, L. Xia, J. G. Doyle, K. Galsgaard, and H. Fu. Explosive Events on a Subarcsecond Scale in IRIS Observations: A Case Study. *ApJ*, 797:88, Dec. 2014. doi: 10.1088/0004-637X/797/2/88.

D. E. Innes and G. Tóth. Simulations of small-scale explosive events on the Sun. *Sol. Phys.*, 185:127–141, Mar. 1999. doi: 10.1023/A:1005162216540.

D. E. Innes, B. Inhester, W. I. Axford, and K. Wilhelm. Bi-directional plasma jets produced by magnetic reconnection on the Sun. *Nature*, 386:811–813, Apr. 1997. doi: 10.1038/386811a0.

D. E. Innes, L.-J. Guo, Y.-M. Huang, and A. Bhattacharjee. IRIS Si IV Line Profiles: An Indication for the Plasmoid Instability during Small-scale Magnetic Reconnection on the Sun. *ApJ*, 813:86, Nov. 2015. doi: 10.1088/0004-637X/813/2/86.

S.-n. Ishikawa, L. Glesener, S. Krucker, S. Christe, J. C. Buitrago-Casas, N. Narukage, and J. Vievering. Detection of nanoflare-heated plasma in the solar corona by the FOXSI-2 sounding rocket. *Nature Astronomy*, 1:771–774, Oct. 2017. doi: 10.1038/s41550-017-0269-z.

S. Jaeggli. Corrections for Spectral Geometry. IRIS Technical Note 19, Montana State University, Bozeman, MT, July 2016.

S. A. Jaeggli, P. G. Judge, and A. N. Daw. Formation of the UV Spectrum of Molecular Hydrogen in the Sun. *ApJ*, 855(2):134, Mar 2018. doi: 10.3847/1538-4357/aaafd5.

D. B. Jess, M. Mathioudakis, R. Erdélyi, P. J. Crockett, F. P. Keenan, and D. J. Christian. Alfvén waves in the lower solar atmosphere. *Science*, 323(5921):1582–1585, 2009. ISSN 0036-8075. doi: 10.1126/science.1168680. URL `https://science.sciencemag.org/content/323/5921/1582`.

M. A. Johnson, C. C. Kankelborg, R. Meuchel, and R. Smart. Confocal microscopy for high-precision non-contact optical measurements. In *Optical System Alignment, Tolerancing, and Verification XII*, volume 10747 of *Proc. SPIE*, page 107470A, Sept. 2018. doi: 10.1117/12.2319597.

C. Jordan. The intensities of helium lines in the solar EUV spectrum. *MNRAS*, 170:429–440, Feb. 1975. doi: 10.1093/mnras/170.2.429.

A. C. Kak and M. Slaney. *Principles of Computerized Tomographic Imaging.* IEEE Press, 345 East 47th Street, New York, NY 10017-2394, 1988. ISBN 0-87942-198-3.

C. C. Kankelborg and R. J. Thomas. Simultaneous imaging and spectroscopy of the solar atmosphere: advantages and challenges of a 3-order slitless spectrograph.

In O. H. Siegmund, S. Fineschi, and M. A. Gummin, editors, *UV/EUV and Visible Space Instrumentation for Astronomy and Solar Physics*, volume 4498 of *Proc. SPIE*, pages 16–26, Dec. 2001. doi: 10.1117/12.450074.

R. Kano, T. Bando, N. Narukage, R. Ishikawa, S. Tsuneta, Y. Katsukawa, M. Kubo, S.-n. Ishikawa, H. Hara, T. Shimizu, Y. Suematsu, K. Ichimoto, T. Sakao, M. Goto, Y. Kato, S. Imada, K. Kobayashi, T. Holloway, A. Winebarger, J. Cirtain, B. De Pontieu, R. Casini, J. Trujillo Bueno, J. Štepán, R. Manso Sainz, L. Belluzzi, A. Asensio Ramos, F. Auchère, and M. Carlsson. Chromospheric Lyman-alpha spectro-polarimeter (CLASP). In *Space Telescopes and Instrumentation 2012: Ultraviolet to Gamma Ray*, volume 8443 of *Proc. SPIE*, page 84434F, Sept. 2012. doi: 10.1117/12.925991.

M. Karovska, S. R. Habbal, L. Golub, E. DeLuca, and H. Hudson. Recovering the fine structures in solar images. In J. J. Hunt, editor, *Solar Dynamic Phenomena and Solar Wind Consequences, the Third SOHO Workshop*, volume SP-373 of *ESA*, page 183, Dec. 1994.

F. P. Keenan, A. E. Kingston, K. M. Aggarwal, and K. G. Widing. Mg vii and Si ix line ratios in the sun. *Sol. Phys.*, 103(2):225–230, Feb 1986. doi: 10.1007/BF00147825.

F. P. Keenan, K. M. Aggarwal, D. S. Bloomfield, A. Z. Msezane, and K. G. Widing. An investigation of Fe XV emission lines in solar flare spectra. *A&A*, 449:1203–1208, Apr. 2006. doi: 10.1051/0004-6361:20054028.

J. A. Klimchuk. On Solving the Coronal Heating Problem. *Sol. Phys.*, 234:41–77, Mar. 2006. doi: 10.1007/s11207-006-0055-z.

K. Kobayashi, H. Hara, R. Kano, S. Nagata, T. Sakao, T. Shimizu, S. Tsuneta, T. Yoshida, and R. Harrison. On the Detection of Solar Coronal High-Velocity Fields Using the XUV Doppler Telescope. *PASJ*, 52:1165–L1174, Dec. 2000. doi: 10.1093/pasj/52.6.1165.

K. Kobayashi, R. Kano, J. Trujillo-Bueno, A. Asensio Ramos, T. Bando, L. Belluzzi, M. Carlsson, R. C. B. De Pontieu, H. Hara, K. Ichimoto, R. Ishikawa, Y. Katsukawa, M. Kubo, R. Manso Sainz, N. Narukage, T. Sakao, J. Stepan, Y. Suematsu, S. Tsuneta, H. Watanabe, and A. Winebarger. The Chromospheric Lyman-Alpha SpectroPolarimeter: CLASP. In L. Golub, I. De Moortel, and T. Shimizu, editors, *Fifth Hinode Science Meeting*, volume 456 of *Astronomical Society of the Pacific Conference Series*, page 233, May 2012.

K. Kobayashi, J. Cirtain, A. R. Winebarger, K. Korreck, L. Golub, R. W. Walsh, B. De Pontieu, C. DeForest, A. Title, S. Kuzin, S. Savage, D. Beabout, B. Beabout, W. Podgorski, D. Caldwell, K. McCracken, M. Ordway, H. Bergner, R. Gates, S. McKillop, P. Cheimets, S. Platt, N. Mitchell, and D. Windt. The High-Resolution

Coronal Imager (Hi-C). *Sol. Phys.*, 289:4393–4412, Nov. 2014. doi: 10.1007/s11207-014-0544-4.

R. A. Kopp and G. W. Pneuman. Magnetic reconnection in the corona and the loop prominence phenomenon. *Sol. Phys.*, 50(1):85–98, Oct 1976. doi: 10.1007/BF00206193.

T. Kosugi, K. Matsuzaki, T. Sakao, T. Shimizu, Y. Sone, S. Tachikawa, T. Hashimoto, K. Minesugi, A. Ohnishi, and T. Yamada. The Hinode (Solar-B) Mission: An Overview. *Sol. Phys.*, 243(1):3–17, Jun 2007. doi: 10.1007/s11207-007-9014-6.

M. Kubo, Y. Katsukawa, Y. Suematsu, R. Kano, T. Bando, N. Narukage, R. Ishikawa, H. Hara, G. Giono, S. Tsuneta, S. Ishikawa, T. Shimizu, T. Sakao, A. Winebarger, K. Kobayashi, J. Cirtain, P. Champey, F. Auchère, J. Trujillo Bueno, A. Asensio Ramos, J. Štěpán, L. Belluzzi, R. Manso Sainz, B. De Pontieu, K. Ichimoto, M. Carlsson, R. Casini, and M. Goto. Discovery of Ubiquitous Fast-Propagating Intensity Disturbances by the Chromospheric Lyman Alpha Spectropolarimeter (CLASP). *ApJ*, 832(2):141, Dec. 2016. doi: 10.3847/0004-637X/832/2/141.

T. Kudoh and K. Shibata. Alfvén Wave Model of Spicules and Coronal Heating. *ApJ*, 514(1):493–505, Mar. 1999. doi: 10.1086/306930.

J. Leenaarts, T. M. D. Pereira, M. Carlsson, H. Uitenbroek, and B. De Pontieu. The Formation of IRIS Diagnostics. I. A Quintessential Model Atom of Mg II and General Formation Properties of the Mg II h&k Lines. *ApJ*, 772:89, Aug. 2013a. doi: 10.1088/0004-637X/772/2/89.

J. Leenaarts, T. M. D. Pereira, M. Carlsson, H. Uitenbroek, and B. De Pontieu. The Formation of IRIS Diagnostics. II. The Formation of the Mg II h&k Lines in the Solar Atmosphere. *ApJ*, 772:90, Aug. 2013b. doi: 10.1088/0004-637X/772/2/90.

J. R. Lemen, A. M. Title, D. J. Akin, P. F. Boerner, C. Chou, J. F. Drake, D. W. Duncan, C. G. Edwards, F. M. Friedlaender, G. F. Heyman, N. E. Hurlburt, N. L. Katz, G. D. Kushner, M. Levay, R. W. Lindgren, D. P. Mathur, E. L. McFeaters, S. Mitchell, R. A. Rehse, C. J. Schrijver, L. A. Springer, R. A. Stern, T. D. Tarbell, J.-P. Wuelser, C. J. Wolfson, C. Yanari, J. A. Bookbinder, P. N. Cheimets, D. Caldwell, E. E. Deluca, R. Gates, L. Golub, S. Park, W. A. Podgorski, R. I. Bush, P. H. Scherrer, M. A. Gummin, P. Smith, G. Auker, P. Jerram, P. Pool, R. Soufli, D. L. Windt, S. Beardsley, M. Clapp, J. Lang, and N. Waltham. The Atmospheric Imaging Assembly (AIA) on the Solar Dynamics Observatory (SDO). *Sol. Phys.*, 275:17–40, Jan. 2012. doi: 10.1007/s11207-011-9776-8.

Lockheed Missiles and Space Co. Report. Solar Pointing Aerobee Rocket Control System (SPARCS) Final report. Technical Report Contract NAS2-3500, Lockheed Missiles and Space Co., Sunnyvale, California, Nov. 1969.

D. W. Longcope and L. A. Tarr. Relating magnetic reconnection to coronal heating. *PHILOS T R SOC A*, 373(2042), February 2015.

Lord Rayleigh F.R.S. XXXI. Investigations in optics, with special reference to the spectroscope. *The London, Edinburgh, and Dublin Philosophical Magazine and Journal of Science*, 8(49):261–274, 1879. doi: 10.1080/14786447908639684.

L. B. Lucy. An iterative technique for the rectification of observed distributions. *AJ*, 79:745, June 1974. doi: 10.1086/111605.

J. T. Mariska. The quiet solar transition region. *ARA&A*, 24:23–48, 1986. doi: 10.1146/annurev.aa.24.090186.000323.

J. T. Mariska. *The solar transition region*. Cambridge astrophysics series ; 23. Cambridge University Press, Cambridge [England] ; New York, NY, USA, 1992. ISBN 0521382610.

S. W. McIntosh, B. de Pontieu, M. Carlsson, V. Hansteen, P. Boerner, and M. Goossens. Alfvénic waves with sufficient energy to power the quiet solar corona and fast solar wind. *Nature*, 475:477–480, July 2011. doi: 10.1038/nature10235.

T. G. Moran. Interpretation of coronal off-limb spectral line width measurements. *A&A*, 374:L9–L11, Aug. 2001. doi: 10.1051/0004-6361:20010643.

T. G. Moran. Test for Alfvén Wave Signatures in a Solar Coronal Hole. *ApJ*, 598: 657–666, Nov. 2003. doi: 10.1086/378795.

J. S. Morrill and C. M. Korendyke. High-Resolution Center-to-Limb Variation of the Quiet Solar Spectrum near Mg II. *ApJ*, 687:646–657, Nov. 2008. doi: 10.1086/591305.

D. Moses, J. W. Cook, J.-D. F. Bartoe, G. E. Brueckner, K. P. Dere, D. F. Webb, J. M. Davis, J. W. Harvey, F. Recely, S. F. Martin, and H. Zirin. Solar fine scale structures in the corona, transition region, and lower atmosphere. *ApJ*, 430: 913–924, Aug. 1994. doi: 10.1086/174461.

R. E. Nather and D. S. Evans. Photoelectric measurement of lunar occultations. I. The process. *AJ*, 75:575–582, June 1970. doi: 10.1086/110991.

L. J. November and G. W. Simon. Precise proper-motion measurement of solar granulation. *ApJ*, 333:427–442, Oct. 1988. doi: 10.1086/166758.

B. O'Dwyer, G. Del Zanna, H. E. Mason, M. A. Weber, and D. Tripathi. SDO/AIA response to coronal hole, quiet Sun, active region, and flare plasma. *A&A*, 521: A21, Oct 2010. doi: 10.1051/0004-6361/201014872.

T. Okamoto and I. Yamaguchi. Simultaneous acquisition of spectral image information. *Opt. Lett.*, 16(16):1277–1279, Aug 1991. doi: 10.1364/OL.16.001277. URL `http://ol.osa.org/abstract.cfm?URI=ol-16-16-1277`.

E. N. Parker. Sweet's Mechanism for Merging Magnetic Fields in Conducting Fluids. *J. Geophys. Res.*, 62(4):509–520, Dec 1957. doi: 10.1029/JZ062i004p00509.

J. Parker and C. Kankelborg. Determining the Spectral Content of MOSES Images. In *AAS/Solar Physics Division Meeting*, volume 47 of *AAS/Solar Physics Division Meeting*, page 2.04, May 2016.

J. Parker, C. C. Kankelborg, R. T. Smart, A. Winebarger, K. Kobayashi, H. T. Courrier, M. Johnson, L. Rachmeler, and L. Springer. First results from the EUV Snapshot Imaging Spectrograph (ESIS). In preparation, 2020.

S. Patsourakos and J. A. Klimchuk. Nonthermal Spectral Line Broadening and the Nanoflare Model. *ApJ*, 647:1452–1465, Aug. 2006. doi: 10.1086/505517.

T. M. D. Pereira, J. Leenaarts, B. De Pontieu, M. Carlsson, and H. Uitenbroek. The Formation of IRIS Diagnostics. III. Near-ultraviolet Spectra and Images. *ApJ*, 778: 143, Dec. 2013. doi: 10.1088/0004-637X/778/2/143.

H. Peter. Analysis of Transition-Region Emission-Line Profiles from Full-Disk Scans of the Sun Using the SUMER Instrument on SOHO. *ApJ*, 516(1):490–504, May 1999. doi: 10.1086/307102.

D. M. Peterson, R. Baron, E. W. Dunham, D. Mink, G. Aldering, J. Klavetter, and R. Morgan. Lunar Occultation of Praesepe. II. Massachusetts. *AJ*, 98:2156, Dec 1989. doi: 10.1086/115285.

H. E. Petschek. Magnetic Field Annihilation. *NASA Special Publication*, 50:425, 1964.

A. A. Pevtsov, G. H. Fisher, L. W. Acton, D. W. Longcope, C. M. Johns-Krull, C. C. Kankelborg, and T. R. Metcalf. The Relationship Between X-Ray Radiance and Magnetic Flux. *ApJ*, 598(2):1387–1391, Dec 2003. doi: 10.1086/378944.

W. A. Podgorski, P. N. Cheimets, L. Golub, J. R. Lemen, and A. M. Title. Design, performance prediction, and measurements of the interface region imaging spectrograph (IRIS) telescope. In *Space Telescopes and Instrumentation 2012: Ultraviolet to Gamma Ray*, volume 8443 of *Proc. SPIE*, page 84433D, Sept. 2012. doi: 10.1117/12.925491.

B. Poduval, C. E. DeForest, J. T. Schmelz, and S. Pathak. Point-spread Functions for the Extreme-ultraviolet Channels of SDO/AIA Telescopes. *ApJ*, 765:144, Mar. 2013. doi: 10.1088/0004-637X/765/2/144.

L. Poletto and R. J. Thomas. Stigmatic Spectrometers for Extended Sources: Design with Toroidal Varied-Line-Space Gratings. *Appl. Opt.*, 43:2029–2038, Apr. 2004. doi: 10.1364/AO.43.002029.

F. R. Powell, P. W. Vedder, J. F. Lindblom, and S. F. Powell. Thin film filter performance for extreme ultraviolet and X-ray applications. *Optical Engineering*, 29:614–624, June 1990. doi: 10.1117/12.55641.

E. R. Priest. *Solar magneto-hydrodynamics.*, volume 21. Dordrecht: Springer Netherlands, 1982.

E. R. Priest and T. G. Forbes. The magnetic nature of solar flares. *A&A Rev.*, 10: 313–377, 2002. doi: 10.1007/s001590100013.

K. G. Puschmann, C. Denker, F. Kneer, N. Al Erdogan, H. Balthasar, S. M. Bauer, C. Beck, N. Bello González, M. Collados, T. Hahn, J. Hirzberger, A. Hofmann, R. E. Louis, H. Nicklas, O. Okunev, V. Martínez Pillet, E. Popow, T. Seelemann, R. Volkmer, A. D. Wittmann, and M. Woche. The GREGOR Fabry-Pérot Interferometer. *Astronomische Nachrichten*, 333:880, Nov. 2012. doi: 10.1002/asna.201211734.

W. H. Richardson. Bayesian-Based Iterative Method of Image Restoration. *J. Opt. Soc. Am.*, 62(1):55–59, Jan 1972. doi: 10.1364/JOSA.62.000055.

A. Richichi. Model-independent retrieval of brightness profiles from lunar occultation lightcurves in the near infrared domain. *A&A*, 226:366–372, Dec. 1989.

R. Rosner, W. H. Tucker, and G. S. Vaiana. Dynamics of the quiescent solar corona. *ApJ*, 220:643–645, Mar. 1978. doi: 10.1086/155949.

T. Rust. Private Communication, March 2015.

T. Rust and C. C. Kankelborg. Quiet-Sun Explosive Events Observed in He II λ304 with MOSES-06. *ApJ*, 877(1):59, May 2019. doi: 10.3847/1538-4357/ab12e2.

T. L. Rust. *Explosive Events in the Quiet Sun: Extreme Ultraviolet Imaging Spectroscopy Instrumentation and Observations.* PhD thesis, Montana State Univeristy, Bozeman, MT, July 2017.

T. Sakao, S. Tsuneta, H. Hara, T. Shimizu, R. Kano, K. Kumagai, T. Yoshida, S. Nagata, and K. Kobayashi. The XUV Doppler Telescope (XDT). *Sol. Phys.*, 187(2):303–333, July 1999. doi: 10.1023/A:1005127827006.

P. H. Scherrer, R. S. Bogart, R. I. Bush, J. T. Hoeksema, A. G. Kosovichev, J. Schou, W. Rosenberg, L. Springer, T. D. Tarbell, A. Title, C. J. Wolfson, I. Zayer, and MDI Engineering Team. The Solar Oscillations Investigation - Michelson Doppler Imager. *Sol. Phys.*, 162:129–188, Dec. 1995. doi: 10.1007/BF00733429.

J. T. Schmelz and A. R. Winebarger. What can observations tell us about coronal heating? *Philosophical Transactions of the Royal Society of London Series A*, 373 (2042):20140257–20140257, Apr 2015. doi: 10.1098/rsta.2014.0257.

P. W. Schuck. Tracking Magnetic Footpoints with the Magnetic Induction Equation. *ApJ*, 646:1358–1391, Aug. 2006. doi: 10.1086/505015.

P. Shearer, R. A. Frazin, A. O. Hero, III, and A. C. Gilbert. The First Stray Light Corrected Extreme-ultraviolet Images of Solar Coronal Holes. *ApJ*, 749:L8, Apr. 2012. doi: 10.1088/2041-8205/749/1/L8.

K. Shibata and T. Magara. Solar Flares: Magnetohydrodynamic Processes. *Living Reviews in Solar Physics*, 8(1):6, Dec 2011. doi: 10.12942/lrsp-2011-6.

A. K. Srivastava, J. Shetye, K. Murawski, J. G. Doyle, M. Stangalini, E. Scullion, T. Ray, D. P. Wójcik, and B. N. Dwivedi. High-frequency torsional Alfvén waves as an energy source for coronal heating. *Scientific Reports*, 7:43147, Mar. 2017. doi: 10.1038/srep43147.

E. Staath and P. Lemaire. High resolution profiles of the MG II H and MG II K lines. *A&A*, 295:517–528, Mar. 1995.

R. A. Stern, L. Shing, P. R. Catura, M. D. Morrison, D. W. Duncan, J. R. Lemen, T. Eaton, P. J. Pool, R. Steward, D. M. Walton, and A. Smith. Characterization of the flight CCD detectors for the GOES N and O solar x-ray imagers. In S. Fineschi and M. A. Gummin, editors, *Telescopes and Instrumentation for Solar Astrophysics*, volume 5171 of *Proc. SPIE*, pages 77–88, Feb. 2004. doi: 10.1117/12.506346.

C. R. Subrahmanya. A new method of deconvolution and its application to lunar occultations. *A&A*, 89:132–139, Sept. 1980.

H. Tian. Probing the solar transition region: current status and future perspectives. *Research in Astronomy and Astrophysics*, 17:110, Oct. 2017. doi: 10.1088/1674-4527/17/11/110.

H. Tian, C. Y. Tu, E. Marsch, J. S. He, and G. Q. Zhou. Signature of mass supply to quiet coronal loops. *A&A*, 478:915–919, Feb. 2008. doi: 10.1051/0004-6361:20078813.

S. Tomczyk, S. W. McIntosh, S. L. Keil, P. G. Judge, T. Schad, D. H. Seeley, and J. Edmondson. Alfvén Waves in the Solar Corona. *Science*, 317(5842):1192, Aug 2007. doi: 10.1126/science.1143304.

R. Tousey. Solar spectroscopy from Rowland to SOT. *Vistas in Astronomy*, 29: 175–199, 1986. doi: 10.1016/0083-6656(86)90007-3.

R. Tousey, J. D. F. Bartoe, J. D. Bohlin, G. E. Brueckner, J. D. Purcell, V. E. Scherrer, N. R. Sheeley, Jr., R. J. Schumacher, and M. E. Vanhoosier. A Preliminary Study of the Extreme Ultraviolet Spectroheliograms from Skylab. *Sol. Phys.*, 33:265–280, Dec. 1973. doi: 10.1007/BF00152418.

R. Tousey, J.-D. F. Bartoe, G. E. Brueckner, and J. D. Purcell. Extreme ultraviolet spectroheliograph ATM experiment S082A. *Appl. Opt.*, 16:870–878, Apr. 1977.

J. H. Underwood. Soft X-ray imaging with a normal incidence mirror. *Nature*, 294 (5840):429–431, Dec. 1981. doi: 10.1038/294429a0.

U.S. G.P.O. *The Astronomical Almanac for the year 2016*. Government Printing Office; Annual edition (May 28, 2015), Washington, 2015. ISBN 9780707741581.

J. E. Vernazza and E. M. Reeves. Extreme ultraviolet composite spectra of representative solar features. *ApJS*, 37:485–513, Aug. 1978. doi: 10.1086/190539.

A. B. C. Walker, T. W. Barbee, R. B. Hoover, and J. F. Lindblom. Soft X-ray images of the solar corona with a normal-incidence Cassegrain multilayer telescope. *Science*, 241:1781–1787, Sept. 1988. doi: 10.1126/science.241.4874.1781.

H. Wang. Comparison of Hα and He II λ304 Macrospicules. *ApJ*, 509:461–470, Dec. 1998. doi: 10.1086/306497.

M. Weber, E. E. Deluca, L. Golub, J. Cirtain, R. Kano, T. Sakao, K. Shibasaki, and N. Narukage. An On-Orbit Determination of the On-Axis Point Spread Function of the Hinode X-Ray Telescope. *PASJ*, 59:S853–S855, Nov. 2007. doi: 10.1093/pasj/59.sp3.S853.

S. Wedemeyer-Böhm. Point spread functions for the Solar optical telescope onboard Hinode. *A&A*, 487:399–412, Aug. 2008. doi: 10.1051/0004-6361:200809819.

K. Wilhelm, B. N. Dwivedi, E. Marsch, and U. Feldman. Observations of the Sun at Vacuum- Ultraviolet Wavelengths from Space. Part I: Concepts and Instrumentation. *Space Sci. Rev.*, 111:415–480, Apr. 2004. doi: 10.1023/B:SPAC.0000032695.27525.54.

D. L. Windt, S. Donguy, J. Seely, and B. Kjornrattanawanich. Experimental Comparison of Extreme-Ultraviolet Multilayers for Solar Physics. *Appl. Opt.*, 43 (9):1835–1848, Mar. 2004. doi: 10.1364/AO.43.001835.

J.-P. Wuelser, W. A. Rosenberg, and M. E. Bruner. Tunable Fabry-Perot etalons for the 120- to 150-nm wavelength range. In S. Fineschi, C. M. Korendyke, O. H. Siegmund, and B. E. Woodgate, editors, *Instrumentation for UV/EUV Astronomy and Solar Missions*, volume 4139 of *Proc. SPIE*, pages 390–401, Dec. 2000. doi: 10.1117/12.410537.

J.-P. Wülser, S. Jaeggli, B. De Pontieu, T. Tarbell, P. Boerner, S. Freeland, W. Liu, R. Timmons, S. Brannon, C. Kankelborg, C. Madsen, S. McKillop, J. Prchlik, S. Sarr, N. Schanche, P. Testa, P. Bryans, and M. Wiesmann. Instrument Calibration of the *Interface Region Imaging Spectrograph* (IRIS) Mission. *Sol. Phys.*, submitted, 2018.

P. R. Young, K. P. Dere, G. Del Zanna, E. Landi, and R. Sutherland. Latest updates to the CHIANTI atomic database. In *American Astronomical Society Meeting Abstracts*, volume 51 of *American Astronomical Society Meeting Abstracts*, page 314.02, Jun 2019.

APPENDICES

APPENDIX A

ERROR ESTIMATION

In this section we estimate error in correlation between two images due to random intensity errors in the data. We begin by assuming we have two different 1D Gaussian intensity distributions, $F(x)$ and $G(x)$, centered at the origin,

$$F(x) = f(x) \pm \epsilon_f = f_0 e^{\frac{-x^2}{2\sigma_f^2}} + E_f(x)\,, \tag{A.1}$$

$$G(x) = g(x) \pm \epsilon_g = g_0 e^{\frac{-x^2}{2\sigma_g^2}} + E_g(x)\,, \tag{A.2}$$

where x is position in pixels, f_o is intensity at $x = 0$, σ_f is the characteristic width of the distribution, $E_f(x)$ is per pixel Gaussian distributed noise with mean zero and standard deviation ϵ_f, and similarly for Eq. A.2. The correlation function is then written,

$$H(x) = F(x)\otimes G(x) \approx \frac{\sqrt{2\pi} f_0 g_0 \sigma_f \sigma_g}{\sqrt{\sigma_f^2 + \sigma_g^2}} e^{\frac{-x^2}{2(\sigma_f^2+\sigma_g^2)}} + [f(x)\otimes E_g(x)] + [g(x)\otimes E_f(x)]\,, \tag{A.3}$$

where $\otimes$ is the cross-correlation operator. Assuming the real intensity distributions contain sufficient background so that $E_f(x)$ and $E_g(x)$ vary only weakly with x, we write

$$f(x)\otimes E_g(x) \approx \epsilon_g \sqrt{\int_{-\infty}^{\infty} f^2(x)dx} = f_0 \epsilon_g \sqrt{\sigma_f}\pi^{\frac{1}{4}}\,, \tag{A.4}$$

$$g(x)\otimes E_f(x) \approx \epsilon_f \sqrt{\int_{-\infty}^{\infty} g^2(x)dx} = g_0 \epsilon_f \sqrt{\sigma_g}\pi^{\frac{1}{4}}\,. \tag{A.5}$$

The uncertainty in $H(x)$ is therefore:

$$\sigma_\otimes = \sqrt{\sqrt{\pi}\sigma_f (f_0\epsilon_g)^2 + \sqrt{\pi}\sigma_g (g_0\epsilon_f)^2}\,, \tag{A.6}$$

where Eq. A.6 results from adding Eq. A.4 and Eq. A.5 in quadrature. For small displacements of x (not accounting for errors in intensity), we Taylor expand the first term of Eq. A.3 so that

$$h(x) \approx \frac{\sqrt{2\pi} f_0 g_0 \sigma_f \sigma_g}{\sqrt{\sigma_c^2 + \sigma_g^2}} \left(1 + \frac{-x^2}{2(\sigma_f^2 + \sigma_g^2)}\right)\,. \tag{A.7}$$

To find how the position of the maximum correlation, $h(0)$, varies with intensity fluctuations we solve

$$h(0) - h(x) = \sigma_\otimes\,, \tag{A.8}$$

for x. The error in doppler velocity from random intensity fluctuations, σ_d, is then x multiplied by the MOSES pixel dispersion ($29\,\mathrm{km\,s^{-1}}$) so that

$$\sigma_d = 29 \times \sqrt{\frac{\sqrt{2}(\sigma_f^2+\sigma_g^2)^3}{f_0 g_0 \sigma_f \sigma_g}} \left[\frac{\sigma_f (f_0 \epsilon_g)^2}{\sqrt{\pi}} + \frac{\sigma_g (g_0 \epsilon_f)^2}{\sqrt{\pi}}\right]^{\frac{1}{4}} . \tag{A.9}$$

Values of σ_f and σ_g are estimated for each MOSES image order by the Gaussian fits in Fig. 2.4. For convenience we list the characteristic width, σ_m, together with gain (j) and read noise (σ_r^2) determined by Ref. 134 in Table A.1 for each of the MOSES CCDs. The value of ϵ_f is then

$$\epsilon_f^2 = j f_0 + \sigma_r^2 \,, \tag{A.10}$$

for each image order, and similarly for ϵ_g.

Table A.1: Error model parameters at 30.4 nm.

CCD	σ_m [Pixel]	j [DN/photon]	σ_r^2 [DN]
$m=-1$	2.33	1.79	4.4
$m=0$	2.15	1.73	4.3
$m+1$	1.84	1.76	5.1

APPENDIX B

DIFFRACTION FROM MERCURY'S LIMB

In some cases, diffraction at the Moon's limb is a measurable effect at the Earth's surface; *e.g.* diffraction effects from Lunar occultations has been used to determine the angular diameters of distant stars [*e.g.* Nather and Evans, 1970, and references therein]. The question is then raised, in the case of the *IRIS* Mercury transit observations, does diffraction from Mercury's limb have a measurable contribution to the PSF estimates derived in chapter 3? Here, diffraction from Mercury's limb is modeled (conservatively) using Fresnel (near field) diffraction. The results of the model described herein shows that diffraction from Mercury's limb is negligible at *IRIS* resolution.

B.1 Mercury Diffraction Model

Similar to the occultation of distant stars by celestial bodies, the occlusion caused by Mercury can be approximated by an opaque, semi-infinite knife-edge. A schematic diagram of the Sun-Mercury-Earth geometry is shown in Figure B.1. The resulting intensity pattern at the Earth is modeled by the Fresnel (near field) diffraction equation since the aperture created by the knife-edge extends to infinity in one direction. For distant stars, the diffraction pattern created under these circumstances consists of alternating bright and dark bands in the starlight that extends beyond the edge of the geometric shadow. The characteristic length between these shadow bands is much larger than a typical telescope aperture. Hence, the diffraction effect is detected as a modulation in intensity with time as the shadow bands sweep across the telescope aperture in concert with the sky-plane motion of the diffracting object. These intensity fluctuations can be detected by large telescopes with millisecond exposure lengths (*e.g.* Peterson et al. [1989]).

To estimate the diffraction of sunlight from the limb of Mercury, an infinitesimally small portion of the solar surface can be treated as a point source similar to the stellar diffraction case outlined above. Following the stellar diffraction model, the Fresnel diffraction equation for illumination by a single point source located far behind Mercury's limb can then be obtained. To model the Sun as an extended source, the diffraction pattern created at the location of *IRIS* can then be approximated by the contribution from a collection of mutually incoherent point sources that fill the angular width of an *IRIS* pixel. The relevant Sun-Mercury-Earth (*IRIS*) geometry shown in Figure B.1.

B.1.1 *IRIS*-Specific Assumptions

To help simplify the model, the following assumptions are made: First, as mentioned earlier, the occultation caused by Mercury is well approximated as a semi-infinite, 1D knife edge. This treatment is valid (as will be shown below) because, at *IRIS* resolution, the extent of the limb diffraction effects are small and well contained within a single pixel as compared to the ~70 pixel extent of Mercury along the *IRIS* slit found in chapter 3. Thus, diffraction from only one edge of Mercury's limb need be considered as it crosses the *IRIS* spectrograph slit. Second, since *IRIS* is a slit spectrograph, the Sun can be approximated as a monochromatic source. This is a conservative approach that disregards any smoothing of the diffraction pattern (*e.g.* Nather and Evans [1970]) over the optical bandwidth of a single *IRIS* pixel (the *IRIS* spectral scale is 12.8 mÅ FUV and 25.6 mÅ NUV per pixel, respectively, De Pontieu et al. [2014]). Under this assumption, the diffraction pattern can then be investigated anywhere in the IRIS spectral range by choosing a column of constant wavelength, λ.

B.1.2 Fresnel Diffraction Model

Similar to the case of stellar occultations, here we consider a point source located far behind Mercury, so that the distribution of complex field, $U(\xi)$, directly behind Mercury's limb (the *IRIS* or earthward side) is approximated by a plane wave. Once the plane wave encounters Mercury's limb, it takes the form of the Heaviside function so that $U(\xi) = U_0 H(\xi)$, where the point of the knife edge is located at $\xi = 0$ and the amplitude of the field is U_0. The geometric shadow cast by the knife-edge lands at $x = 0$ after traveling a distance L to Earth, as illustrated schematically in Figure B.1.

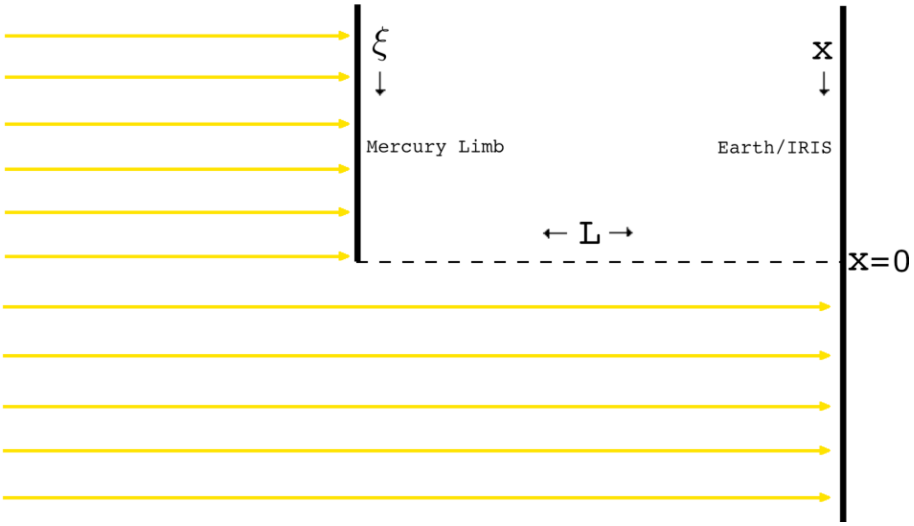

Figure B.1: Schematic diagram (not drawn to scale) representing the complex field immediately behind Mercury's limb. The incoming solar radiation is incident from the left in this diagram. L is the Earth-Mercury distance, while ξ and x are the coordinates parallel to the *IRIS* slit at Mercury and Earth, respectively. The dashed line indicates the geometric shadow cast by Mercury's limb, which lands at $x = 0$ at the Earth.

Under the aforementioned assumptions the complex field at the location of the Earth can be found from the convolution form of the Fresnel diffraction equation (*e.g.* Goodman [2005]). Here the convolution kernel, $h(x)$, is

$$h(x) = e^{\frac{i\pi x^2}{L\lambda}} \tag{B.1}$$

where x is the spatial coordinate (parallel to the *IRIS* slit) of the shadow landing at Earth, and L is the distance from *IRIS* (Earth) to Mercury. The complex field at *IRIS* is then

$$U(x) = U_0 \int_{-\infty}^{\infty} H(\xi) h(x-\xi) d\xi = U_0 \int_{0}^{\infty} h(x-\xi) d\xi = U_0 \int_{-\infty}^{x} e^{\frac{i\pi x'^2}{L\lambda}} dx' \,, \tag{B.2}$$

where the variable substitution $x' = x - \xi$ is made in the last step. The intensity at *IRIS* (along the slit) is $I(x) = |U(x)|^2$ so that

$$I(x) = I_0 \left| \int_{-\infty}^{x} e^{\frac{i\pi x'^2}{L\lambda}} dx' \right|^2 \,, \tag{B.3}$$

with $I_0 = |U_0|^2$. Re-writing Equation B.3 as the sum of two real integrals,

$$I(x) = I_0 \left\{ \left[\int_{-\infty}^{x} \cos(\frac{\pi x'^2}{L\lambda}) dx' \right]^2 + \left[\int_{-\infty}^{x} \sin(\frac{\pi x'^2}{L\lambda}) dx' \right]^2 \right\} . \tag{B.4}$$

Equation B.4 can be re-written in terms of the Fresnel integrals [*e.g.* Subrahmanya, 1980, Goodman, 2005]. Since both $\cos(\frac{\pi t^2}{L\lambda})$ and $\sin(\frac{\pi t^2}{L\lambda})$ are even about 0,

$$\int_{-\infty}^{0} \cos(\frac{\pi x'^2}{L\lambda}) dx' = \int_{-\infty}^{0} \sin(\frac{\pi x'^2}{L\lambda}) dx' = \int_{0}^{\infty} \cos(\frac{\pi x'^2}{L\lambda}) dx' = \sqrt{\frac{L\lambda}{8}} . \tag{B.5}$$

Equation B.4 is then

$$\begin{aligned} I(x) &= I_0 \left[\int_{-\infty}^{0} \cos(\frac{\pi x'^2}{L\lambda}) dx' + \int_{0}^{x} \cos(\frac{\pi x'^2}{L\lambda}) dx' \right]^2 \\ &\quad + I_0 \left[\int_{-\infty}^{0} \sin(\frac{\pi x'^2}{L\lambda}) dx' + \int_{0}^{x} \sin(\frac{\pi x'^2}{L\lambda}) dx' \right]^2 , \\ I(x) &= I_0 \left\{ \left[\sqrt{\frac{L\lambda}{8}} + C\left(\sqrt{\frac{2}{L\lambda}} x \right) \right]^2 + \left[\sqrt{\frac{L\lambda}{8}} + S\left(\sqrt{\frac{2}{L\lambda}} x \right) \right]^2 \right\} , \end{aligned} \tag{B.6}$$

using the Fresnel integrals given by

$$C(u) = \int_{0}^{u} \cos\left(\frac{\pi u'^2}{2} \right) du' \,, \tag{B.7}$$

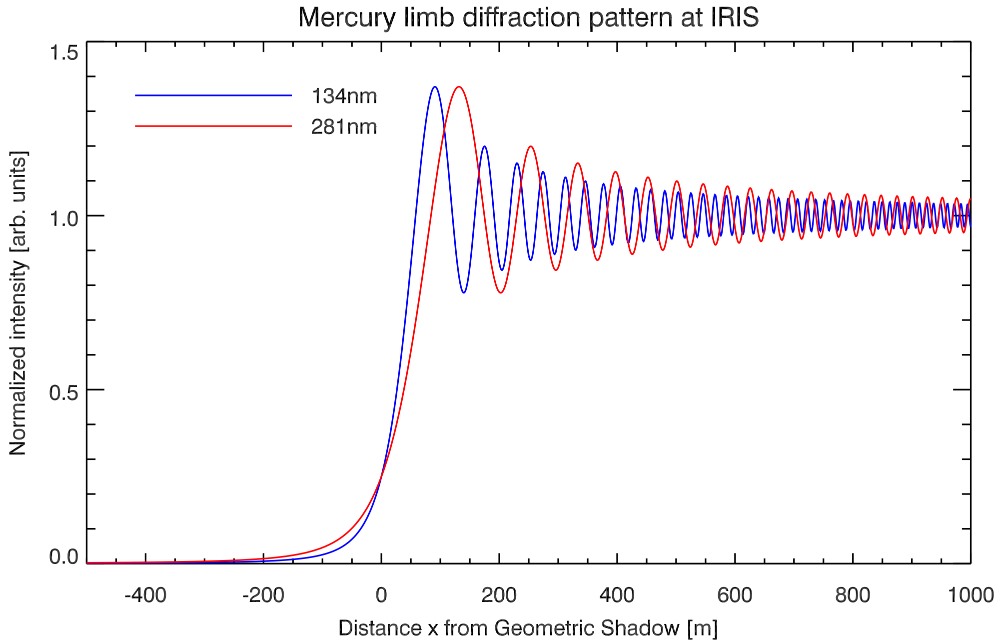

Figure B.2: Solar point source diffraction pattern from Mercury's limb at the position of *IRIS*.

$$S(u) = \int_0^u \sin\left(\frac{\pi u'^2}{2}\right) du' \,, \tag{B.8}$$

Here, Equations B.7 and B.8 are evaluated using the error function, $\mathrm{erf}(u)$,

$$C(u) = \frac{1-i}{4}\left[\mathrm{erf}\left(\frac{1+i}{2}\sqrt{\pi}u\right) + i\,\mathrm{erf}\left(\frac{1-i}{2}\sqrt{\pi}u\right)\right] \,, \tag{B.9}$$

$$S(u) = \frac{1+i}{4}\left[\mathrm{erf}\left(\frac{1+i}{2}\sqrt{\pi}u\right) - i\,\mathrm{erf}\left(\frac{1-i}{2}\sqrt{\pi}u\right)\right] \,. \tag{B.10}$$

B.2 Mercury Limb Diffraction at *IRIS*

In Figure B.2, the point source diffraction pattern described by Equation B.6 is plotted for $\lambda = 134\,\mathrm{nm}$ and $\lambda = 281\,\mathrm{nm}$. These values correspond to the shortest and longest nominal wavelengths in the *IRIS* spectrograph passband, respectively. Since only the modulation in intensity due to diffraction is of interest, the total amplitude is normalized so that $I_0 L\lambda = 1$. Figure B.2 shows that the spacing between fringes is orders of magnitude greater than the 19 cm *IRIS* telescope aperture [De Pontieu et al., 2014]. Therefore, in this approximation of the Sun as a point source, it is clear that no spatial modulation of intensity would be detected along the *IRIS* slit. However, a temporal modulation of intensity would be detected as the shadow bands from Mercury sweep across the *IRIS* telescope aperture. In this case, assuming Mercury has a velocity of $\sim 20\,\mathrm{km\,s^{-1}}$ relative to Earth (*e.g.* U.S. G.P.O. [2015]), an exposure length of less than 2.5 ms would be needed to temporally resolve the bright and dark fringes.

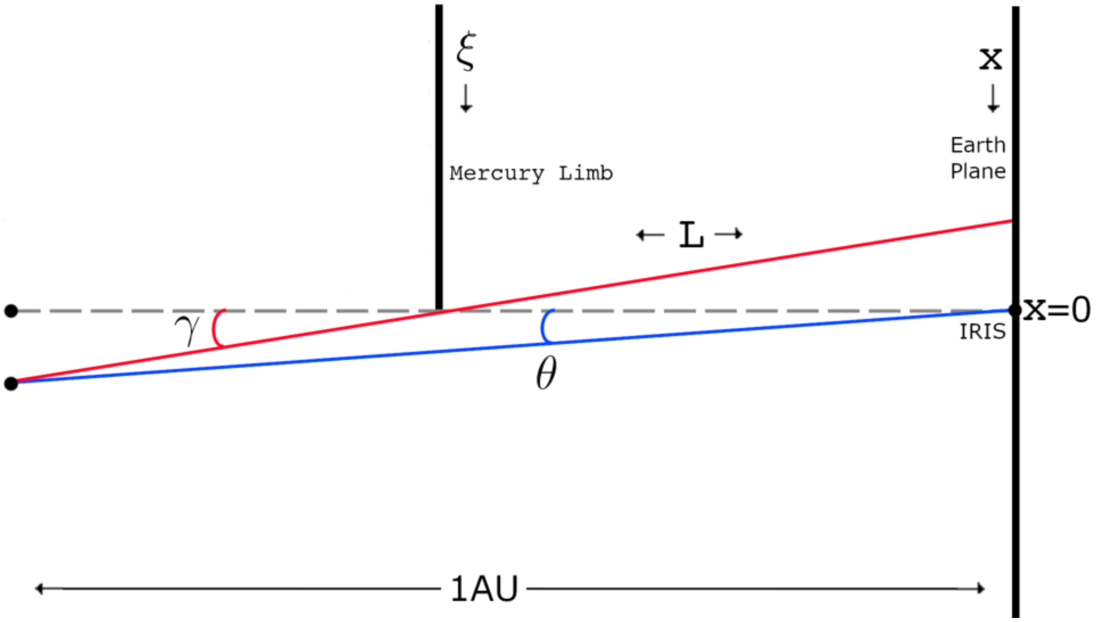

Figure B.3: Schematic diagram showing geometry for diffraction patterns from multiple sources. The Sun is approximated as a collection of point sources that span the *IRIS*angular FOV. The *IRIS* aperture is centered at the geometric shadow at $x = 0$. The intensity pattern that *IRIS* sees from a point source located along the blue line (field angle θ) is centered around the intersection of the red line (angle γ) and the plane located at the Earth.

The Sun, however, is an extended source. To evaluate this case we assume, for simplicity, that the solar surface intensity is constant. Figure B.3 shows a representative source, off-axis at field angle θ. As indicated by the red line, the edge of the geometric shadow cast by Mercury's limb from this source projects to the point $x = -\gamma L$, where $\gamma = \frac{\theta}{1-\frac{L}{1AU}}$. The intensity incident at *IRIS*, located at $x = 0$, from the extended, constant intensity source is then expressed in terms of θ using the $I(x)$ function in Equation B.6,

$$I_{\mathrm{IRIS}}(\theta) = I(-\gamma L) = I\left(\frac{-\theta L}{1 - \frac{L}{1AU}}\right). \tag{B.11}$$

$I_{\mathrm{IRIS}}(\theta)$ is plotted in red in Figure B.4. This represents the idealized intensity

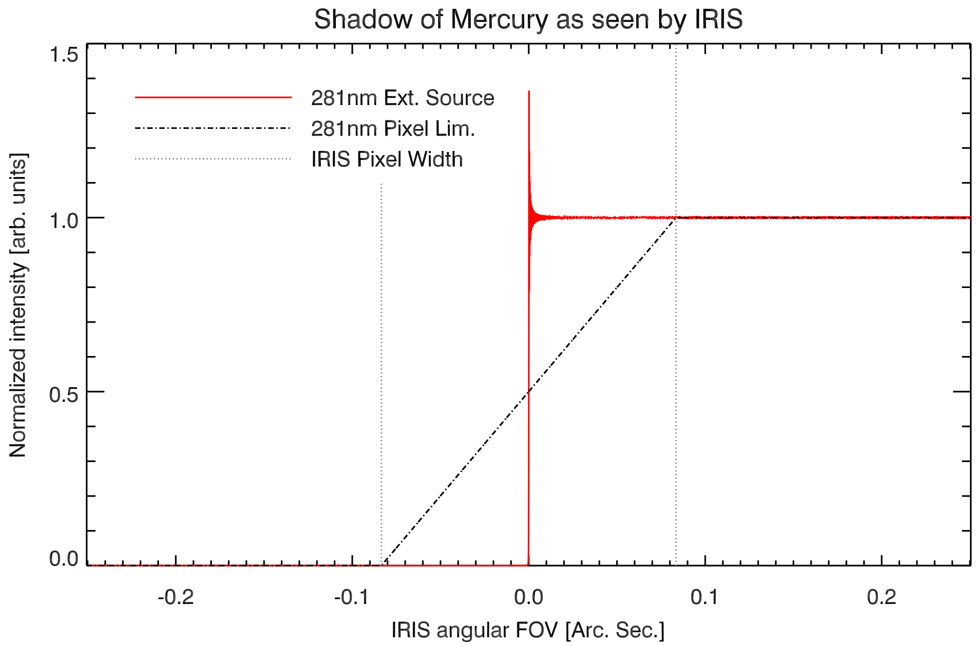

Figure B.4: Solar diffraction pattern from Mercury's limb as seen at the location of *IRIS*. The red curve is the (impossible to observe) diffraction pattern created by an extended, constant intensity source located at the position of the sun as a function of field angle θ. The black dash-dot curve is the red curve convolved with a $1/6''$ boxcar, modeling *IRIS* pixel limited resolution. The gray dotted lines indicate the angular width of an *IRIS* pixel.

observed by an impossible instrument with infinite spatial resolution despite a finite (*i.e.* diffraction limited) aperture. The details of $I_{\text{IRIS}}(\theta)$ are on the order of milliarcsecond scale, and cannot be resolved in practice. If, for example, we imagine that IRIS is pixel limited, then the red intensity curve in Figure B.4 would be convolved with a boxcar of $1/6''$ width [De Pontieu et al., 2014], as illustrated by the black dash-dot curve in the same figure. However, the black dash-dot curve shows no hint of modulation due to diffraction, and so it is indistinguishable from the intensity that would be observed from a geometrically perfect shadow. Therefore, diffraction from Mercury's limb can have no measurable contribution to the point spread functions derived in chapter 3.